DISSOLVED CO_2 EFFECT ON THE REACTIVITY OF THE HONTOMÍN RESERVOIR ROCKS (LIMESTONE AND SANDSTONE)

María García Ríos

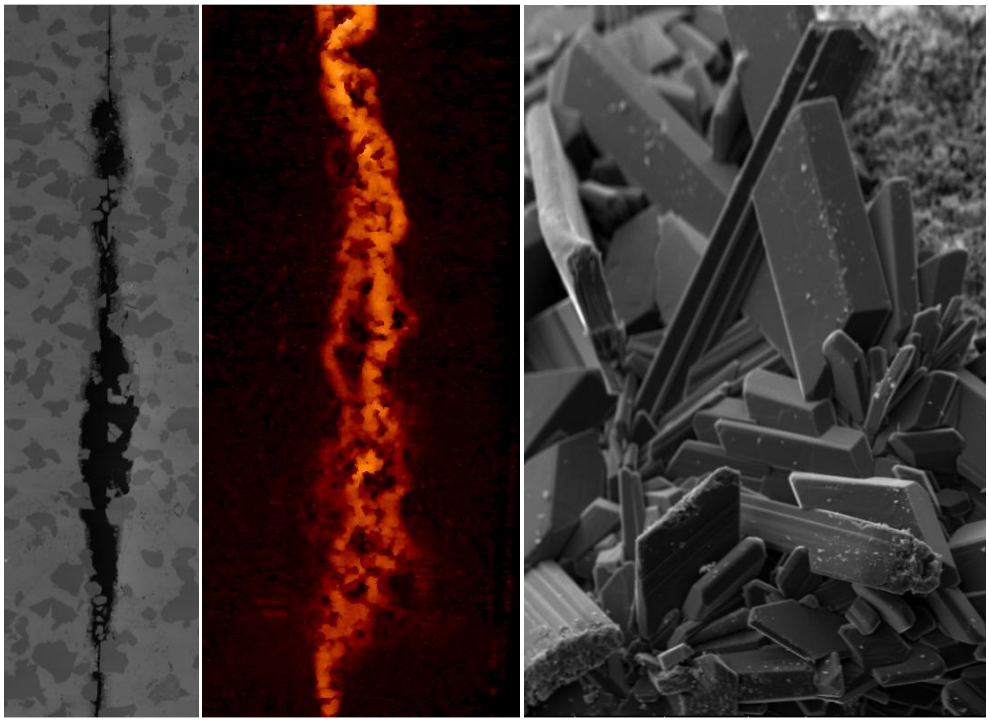

PhD Thesis
Department of Geotechnical Engineering and Geo-Sciences (ETCG)
Technical University of Catalonia (UPC)

Supervisors:
Dr. Jordi Cama Dra. Linda Luquot Dr. Josep M. Soler

Institute of Environmental Assessment and Water Research
(IDAEA-CSIC)

idaea CSIC CONSEJO SUPERIOR DE INVESTIGACIONES CIENTÍFICAS UPC

UNIVERSITAT POLITÈCNICA DE CATALUNYA
BARCELONATECH
Escola de Doctorat

Curso académico:

Acta de calificación de tesis doctoral

Nombre y apellidos: MARIA OLIMPIA GARCIA RIOS

Programa de doctorado:

Unidad estructural responsable del programa

Resolución del Tribunal

Reunido el Tribunal designado a tal efecto, el doctorando / la doctoranda expone el tema de la su tesis doctoral titulada _____

_____.

Acabada la lectura y después de dar respuesta a las cuestiones formuladas por los miembros titulares del tribunal, éste otorga la calificación:

☐ NO APTO ☐ APROBADO ☐ NOTABLE ☐ SOBRESALIENTE

(Nombre, apellidos y firma) Presidente/a		(Nombre, apellidos y firma) Secretario/a
(Nombre, apellidos y firma) Vocal	(Nombre, apellidos y firma) Vocal	(Nombre, apellidos y firma) Vocal

_____, _____ de _____ de _____

El resultado del escrutinio de los votos emitidos por los miembros titulares del tribunal, efectuado por la Escuela de Doctorado, a instancia de la Comisión de Doctorado de la UPC, otorga la MENCIÓN CUM LAUDE:

☐ SÍ ☐ NO

(Nombre, apellidos y firma) Presidente de la Comisión Permanente de la Escuela de Doctorado	(Nombre, apellidos y firma) Secretario de la Comisión Permanente de la Escuela de Doctorado

Barcelona a _____ de _____ de _____

TECHNICAL UNIVERSITY OF CATALONIA (UPC)
DEPARTMENT OF GEOTECHNICAL ENGINEERING AND GEO-SCIENCES (ETCG)

Dissolved CO_2 effect on the reactivity of the Hontomín reservoir rocks

(limestone and sandstone)

Thesis presented by

María García Ríos

Work conducted in the Institute of Environmental Assessment and Water Research (IDAEA-CSIC) under the supervision of

Dr. Jordi Cama i Robert

Institute of Environmental Assessment and Water Research (IDAEA), CSIC

Dra. Linda Luquot

Institute of Environmental Assessment and Water Research (IDAEA), CSIC

Dr. Josep M. Soler

Institute of Environmental Assessment and Water Research (IDAEA), CSIC

Barcelona, February 2015

This thesis has been funded by CIUDEN (project ALM11/009), Spanish Government Project CGL2010-20984-CO2-01 and the PANACEA project (European Community's Seventh Framework Programme FP7/2007-2013 under grant agreement number 282900).

to The Rivers

Abstract

A test site for CO_2 geological storage is situated in Hontomín (Burgos, northern Spain) with a reservoir rock that is mainly composed of limestone (80-85%) and sandstone (15-20%). The reservoir rock is a deep saline aquifer that is covered by a very low permeability formation which acts as a cap rock. During and after CO_2 injection, since the resident groundwater contains sulfate, the resulting CO_2-rich acid solution gives rise to the dissolution of carbonate minerals (calcite and dolomite) and secondary sulfate-rich mineral precipitation (gypsum or anhydrite) may occur. These reactions that may imply changes in the porosity, permeability and pore structure of the repository could vary the CO_2 storage capacity and injectivity of the reservoir rock.

Therefore, **better knowledge about the overall process of gypsum precipitation at the expense of carbonate mineral dissolution in CO_2-rich solutions and its implications for the hydrodynamic properties of the reservoir rocks** is necessary. A first aim of this thesis is to better understand these coupled reactions by assessing the effect that P, pCO_2, T, mineralogy, acidity and solution saturation state exert on these reactions. To this end, experiments using columns filled with crushed limestone or dolostone are conducted under different P–pCO_2 conditions (atmospheric: $1–10^{-3.5}$ bar; subcritical: 10–10 bar; and supercritical: 150–34 bar), T (25, 40 and 60 °C) and input solution compositions (gypsum-undersaturated and gypsum-equilibrated solutions). The CrunchFlow and PhreeqC (v.3) numerical codes are used to perform 1D reactive transport simulations of the experiments to evaluate mineral reaction rates in the system and quantify the porosity variation along the column.

Within the range of P–pCO_2 and T of this study only gypsum precipitation takes place and this only occurs when the injected solution is equilibrated with gypsum. Under the P–pCO_2–T conditions, the volume of precipitated gypsum is smaller than the volume of dissolved carbonate minerals, yielding always an increase in porosity ($\Delta\phi$ up to ≈ 4%).

A decrease in T favors limestone dissolution regardless of pCO_2 owing to increasing undersaturation with decreasing temperature. However, gypsum precipitation is favored at high T and under atmospheric pCO_2 conditions but not at high T and under 10 bar of pCO_2

conditions. The increase in limestone dissolution with pCO_2 is directly attributed to pH, which is more acidic at higher pCO_2.

Limestone dissolution induces late gypsum precipitation (long induction time) in contrast to dolostone dissolution, which promotes rapid gypsum precipitation. Moreover, owing to the slow kinetics of dolomite dissolution with respect to that of calcite, both the volume of dissolved mineral and the increase in porosity are larger in the limestone experiments than in the dolostone ones under all pCO_2 conditions ($10^{-3.5}$ and 10 bar).

By increasing pCO_2, carbonate dissolution occurs along the column whereas it is localized in the very inlet under atmospheric conditions. This is due to the buffer capacity of the carbonic acid, which maintains pH at around 5 and keeps the solution undersaturated with respect to calcite and dolomite along the column.

1D reactive transport simulations reproduce the experimental data (carbonate dissolution and gypsum precipitation for different P–pCO_2–T conditions). Drawing on reaction rate laws in the literature, the reactive surface area to fit the models to the experimental data is used. The values of the reactive surface area are much smaller than those calculated from the geometric areas, given by the transport control of the dissolution reactions.

Given that Hontomín reservoir rock is a fractured system, understanding reaction-induced changes in fracture hydrodynamic properties as a result of contact with acidic fluids is essential for predicting subsurface flows, such as leakage, injectability, and fluid production. Considering this, the second aim of this thesis is to **characterize the overall evolution of a fracture in contact with CO_2-rich solutions under different flow rates**. Also, the geochemical response of two fractured Hontomín reservoir rocks (limestone and sandstone) to injection of a CO_2-rich solution is compared. Hence, a set of percolation experiments which consist of injecting CO_2-rich solutions through fractured limestone and sandstone cores are performed under P = 150 bar and T = 60 ºC at different flow rates ranging from 0.2 to 60 mL/h and sulfate-rich and sulfate-free solutions.

Variation in fracture volume induced by calcite dissolution and gypsum precipitation is measured by means of X-ray computed microtomography (XCMT) and aqueous chemistry. The influence of the flow rate on fracture evolution is accurately evaluated. By increasing the flow rate, under the same pH and far from equilibrium conditions, the volume of dissolved calcite per time increases, confirming that calcite dissolution in the fracture is transport

controlled. In addition, the formation of more uniform geometries under fast flow rates seems to favor calcite dissolution.

The formed dissolution patterns vary from face dissolution to wormhole formation and uniform dissolution by increasing the flow rate (*i.e.*, *Pe* from 1 to 346). Variation in fracture permeability is also measured and is found to be highly dependent on the flow rate and developed dissolution pattern. Fracture permeability always increases regardless the sulfur content of the injected solution.

On the basis of the obtained experimental results, limestone and sandstone reservoir rocks can be evaluated to identify the most favorable geological context within the reservoir for injection and storage of CO_2. In addition, 2D reactive transport models that reproduce the variation in aqueous chemistry and fracture geometry of the experiments are performed to estimate flow and reaction kinetics parameters.

Resum

Una planta pilot per a l'emmagatzematge geològic de CO_2 es troba a Hontomín (Burgos). El reservori és un aqüífer salí profund, format principalment per roca calcària (80-85%) i gres (15-20%), que està situat entre dues capes de molt baixa permeabilitat que actuen com a roques segell. La dissolució de CO_2 a l'aigua del reservori provocarà una disminució del pH i, en conseqüència, la dissolució dels carbonats presents en el reservori. Tenint en compte que l'aigua resident és rica en sulfat, és possible la precipitació de minerals secundaris (guix o anhidrita). Aquestes reaccions poden provocar canvis en la porositat, la permeabilitat i l'estructura de por del reservori que, a la vegada, poden afectar la seva injectivitat i capacitat d'emmagatzematge.

Per tant, cal aprofundir en el **coneixement sobre els processos acoblats de precipitació de guix i dissolució de carbonats (calcita i dolomita) en solucions riques en CO_2 dissolt i les seves implicacions en les propietats hidrodinàmiques de la roca reservori**. Un primer objectiu d'aquesta tesi és poder comprendre millor aquestes reaccions acoblades mitjançant l'avaluació de l'efecte que exerceixen la pressió *P*, la pressió parcial de CO_2 pCO_2, la temperatura *T*, la mineralogia, l'acidesa i l'estat de saturació de la solució sobre aquestes reaccions. Amb aquest objectiu, s'han realitzat una sèrie d'experiments utilitzant columnes plenes de roca calcària o dolomia triturada sota diferents condicions de *P*-pCO_2 (atmosfèrica: 1-10-3.5 bar; subcrítica: 10-10 bar, i supercrítica: 150-34 bar), *T* (25, 40 i 60 ° C) i composició de la solució d'entrada (solucions subsaturades o equilibrades amb guix). Els codis numèrics CrunchFlow i PhreeqC (v.3) s'han utilitzat per realitzar simulacions de transport reactiu dels experiments en columna amb l'objectiu d'avaluar les velocitats de reacció en el sistema i quantificar la variació de la porositat al llarg de la columna.

En les condicions de *P*-pCO_2-*T* estudiades, la precipitació de guix únicament té lloc quan la solució injectada està en equilibri amb guix. A més, el volum de guix precipitat és menor que el volum de carbonat dissolt, originant sempre un augment de porositat ($\Delta\phi$ fins ≈ 4%).

Una disminució en la *T* afavoreix la dissolució de la calcària independentment de la pCO_2 degut a l'augment de la subsaturació. No obstant, la precipitació de guix està afavorida a alta *T* per condicions atmosfèriques, originant-se l'efecte contrari per condicions subcrítiques.

L'augment de la pCO_2 comporta un augment en la dissolució de calcària, fet que és directament atribuït a l'efecte del pH, que és més àcid a major pCO_2.

La dissolució de calcària comporta un retard en la precipitació de guix (llarg temps d'inducció), al contrari del que passa amb la dissolució de dolomia que promou una ràpida precipitació de guix. A més, a causa de la lenta cinètica de dissolució de la dolomita amb respecte a la de la calcita, el volum de mineral dissolt i l'augment de porositat són majors en els experiments amb calcària sota totes les condicions de pCO_2 estudiades.

La dissolució del carbonat es produeix al llarg de tota la columna quan la pCO_2 és alta (10 and 34 bar) i, en canvi, es localitza a l'entrada de la columna sota condicions atmosfèriques. Aquesta diferència és deguda a la capacitat tampó de l'àcid carbònic, ja que manté el pH al voltant de 5 i la solució subsaturada pel que fa a la calcita i a la dolomita al llarg de la columna.

Les simulacions de transport reactiu (1D) reprodueixen les dades experimentals (dissolució de carbonat i precipitació de guix per a les diferents condicions de P-pCO_2-T). En base a les lleis de velocitat de reacció que es troben en la literatura, s'han fet servir els valors de les àrees reactives per realitzar l'ajust del model a les dades experimentals. Aquests valors són bastant inferiors als inicialment calculats a partir de les àrees geomètriques, ja que les reaccions de dissolució estan controlades pel transport.

La roca reservori a Hontomín està significativament fracturada. Per tant, entendre els canvis en les propietats hidrodinàmiques de les fractures, induïts per reaccions de dissolució/precipitació, és essencial per predir els possibles fluxos subterranis tals com fuites, injectivitat o producció de fluids. Tenint en compte això, el segon objectiu d'aquesta tesi és **caracteritzar l'evolució de fractures en contacte amb solucions riques en CO_2 a diferents cabals**. També es compara la resposta geoquímica a la injecció de CO_2 de les dues roques principals del reservori (calcària i gres). Així doncs, es realitza un conjunt d'experiments de percolació que consisteixen en injectar solucions riques en CO_2 (sense sulfat i riques en sulfat) a través de roques de calcària i gres fracturades, sota P = 150 bar i T = 60 ºC i a diferents cabals compresos entre 0,2 i 60 ml/h. La variació del volum de fractura, induïda per la dissolució de calcita i la precipitació de guix, es mesura mitjançant microtomografia de raigs X (XCMT) i la química de la solució. S'avalua també la influència del cabal en l'evolució de la fractura i s'obté que el volum de calcita dissolta per unitat de temps augmenta augmentant el cabal, la qual cosa confirma que la dissolució en la fractura està controlada pel

transport. També s'observa que la formació de geometries més uniformes a cabals més ràpids pot afavorir la dissolució de la calcita.

Els patrons de dissolució varien de 'face dissolution' a 'wormhole' i a 'uniform dissolution' a mesura que s'augmenta el cabal (és a dir, número de Péclet *Pe* d'1 a 346). S'observa que la variació de permeabilitat de la fractura depèn del cabal i del patró de dissolució desenvolupat. La permeabilitat de la fractura sempre augmenta, independentment del contingut de sulfat de la solució d'entrada.

En base als resultats experimentals obtinguts amb les roques d'Hontomín, s'avalua quin seria el context geològic més favorable en el reservori per a la injecció i emmagatzematge del CO_2. A més a més, es realitzen models de transport reactiu (2D) dels experiments de percolació amb fractures per estimar els paràmetres cinètics i de flux.

Resumen

Una planta piloto para el almacenamiento geológico de CO_2 se ubica en Hontomín (Burgos). El reservorio es un acuífero salino profundo que se compone principalmente de roca caliza (80-85%) y arenisca (15-20%). Éste está situado entre dos capas de muy baja permeabilidad que actúan como rocas sello. La disolución de CO_2 en el agua presente en el reservorio provocará una disminución del pH y, en consecuencia, la disolución de los carbonatos presentes en el reservorio. Además, como la solución residente es rica en sulfato, es posible la precipitación de minerales secundarios (yeso o anhidrita). Estas reacciones pueden provocar cambios en la porosidad, permeabilidad y estructura de poro del reservorio que, a su vez, pueden hacer variar su inyectabilidad y capacidad de almacenamiento.

Por todo ello, es necesario profundizar en el **conocimiento sobre los procesos acoplados de precipitación de yeso y disolución de carbonatos (calcita y dolomita) en soluciones ricas en CO_2 disuelto y sus implicaciones en las propiedades hidrodinámicas de la roca reservorio**. Un primer objetivo de esta tesis es comprender mejor estas reacciones acopladas mediante la evaluación del efecto que ejercen la presión *P*, la presión parcial de CO_2 pCO_2, la temperatura *T*, la mineralogía, la acidez y el estado de saturación de la solución sobre estas reacciones. Con este objetivo, se han realizado una serie de experimentos utilizando columnas llenas de roca caliza o dolomía triturada bajo diferentes condiciones de *P*-pCO_2 (atmosférica: 1-$10^{-3.5}$ bar; sub-crítica: 10-10 bar, y supercrítica: 150-34 bar), *T* (25, 40 y 60 ° C) y composición de la solución de entrada (soluciones sub-saturadas o equilibradas con respecto al yeso). Los códigos numéricos CrunchFlow y PhreeqC (v.3) se han utilizado para realizar simulaciones de transporte reactivo de los experimentos en columna con el objetivo de evaluar las velocidades de reacción en el sistema y cuantificar la variación de la porosidad a lo largo de la columna.

En las condiciones de *P*-pCO_2-*T* estudiadas, la precipitación de yeso únicamente tiene lugar cuando la solución inyectada está en equilibrio con yeso. Además, el volumen de yeso precipitado es menor que el volumen de carbonato disuelto, originando siempre un aumento de porosidad ($\Delta\phi$ hasta $\approx$ 4%).

Una disminución en la *T* favorece la disolución de la caliza independientemente de la pCO_2 debido al aumento de la sub-saturación. Sin embargo, hay un aumento en la precipitación de

yeso a alta *T* para condiciones atmosféricas, viéndose el efecto contrario para condiciones sub-críticas. El aumento de la pCO_2 conlleva un aumento en la disolución de caliza, hecho que es directamente atribuido al efecto del pH, que es más ácido a mayor pCO_2.

La disolución de caliza conlleva un retraso en la precipitación de yeso (largo tiempo de inducción), lo contrario que ocurre con la disolución de dolomía que promueve una rápida precipitación de yeso. Además, debido a la lenta cinética de disolución de la dolomita con respecto a la de la calcita, el volumen de mineral disuelto y el aumento de porosidad son mayores en los experimentos con caliza bajo todas las condiciones de pCO_2 estudiadas.

La disolución del carbonato se produce a lo largo de toda la columna cuando la pCO_2 es alta (10 and 34 bar) y, en cambio, se localiza en la entrada de la columna bajo condiciones atmosféricas. Esta diferencia es debida a la capacidad tampón del ácido carbónico, ya que mantiene el pH alrededor de 5 y mantiene la solución sub-saturada con respecto a la calcita y a la dolomita a lo largo de la columna.

Las simulaciones de transporte reactivo (1D) reproducen los datos experimentales (disolución de carbonato y precipitación de yeso para las diferentes condiciones de *P*-pCO_2-*T*). En base a las leyes de velocidad de reacción que se encuentran en literatura, se han usado los valores de las áreas reactivas para realizar el ajuste del modelo a los datos experimentales. Estos valores son bastante inferiores a los inicialmente calculados a partir de las áreas geométricas, debido a que las reacciones de disolución estás controladas por el transporte.

La roca reservorio en Hontomín está significativamente fracturada. Por lo tanto, entender los cambios en las propiedades hidrodinámicas de las fracturas, inducidos por reacciones de disolución/precipitación, es esencial para predecir los posibles flujos subterráneos como fugas, inyectabilidad o producción de fluidos. Teniendo en cuenta esto, el segundo objetivo de esta tesis es **caracterizar la evolución de fracturas que estén en contacto con soluciones ricas en CO_2 a diferentes caudales**. Además, se compara la respuesta geoquímica a la inyección de CO_2 de las dos rocas principales del reservorio (caliza y arenisca). Para ello, se realiza un conjunto de experimentos de percolación que consisten en inyectar soluciones ricas en CO_2 (sin sulfato y ricas en sulfato) a través de rocas de caliza y arenisca fracturadas. Todos ellos bajo P = 150 bar y T = 60 ºC y a diferentes caudales comprendidos entre 0,2 y 60 mL/h. La variación del volumen de fractura, inducida por la disolución de calcita y la precipitación de yeso, se mide mediante micro-tomografía de rayos X (XCMT) y la química de la solución. Se evalúa también la influencia del caudal en la

evolución de la fractura, obteniéndose que aumentando el caudal el volumen de calcita disuelta por unidad de tiempo aumenta, confirmando así que la disolución en la fractura está controlada por el transporte. También se observa que la formación de geometrías más uniformes a caudales más rápidos puede favorecer la disolución de calcita.

Los patrones de disolución varían de ‘face dissolution’ a ‘wormhole’ y a ‘uniform dissolution’ a medida que aumenta el caudal (es decir, números de Péclet *Pe* de 1 a 346). Se mide también la variación de permeabilidad de la fractura encontrando que su evolución depende del caudal y del patrón de disolución desarrollado. La permeabilidad de la fractura siempre aumenta independientemente del contenido de sulfato de la solución de entrada.

En base a los resultados experimentales obtenidos con las rocas de Hontomín, se evalúa cuál sería el contexto geológico más favorable en el reservorio para la inyección y almacenamiento del CO_2. Además, se realizan modelos de transporte reactivo (2D) de los experimentos de percolación con fracturas para estimar los parámetros cinéticos y de flujo.

Agraïments

Quin moment!...això és el que diria un gran amic meu!

Ja ha arribat! i he de reconèixer que el camí no ha estat fàcil. Un camí on hi ha tants forats que agraeixes sincerament que algú et doni un cop de mà. I per això estic aquí, per agrair a tots aquells que en el algun moment s'han parat al costat meu, han vist que necessitava ajuda i me l'han ofert. Ajuda de tota mena, és clar!

....durant les hores llargues del dia, quan estem treballant: gràcies al **Víctor**, al **Francesco**, a la **Cris**, a la **Gaby**, a **l'Anna Russian** i a la **Yoar** per fer que aquestes hores passin de manera més lleugera, per distreure'm, fer-me riure i per aguantar-me en aquells moments on sembla que tot és negre. A **l'Ester** per la seva disponibilitat a l'hora d'ajudar-te en qualsevol problema o de passar una estona agradable xerrant. Al **Carles Ayora** i al **Josep Soler** per la seva ajuda incondicional. A la **Linda** per la seva ajuda amb condicions (li dec molta pasta!) però sempre amable i profitosa.

...quan arribes a casa tot cansat: gràcies al **Josevi** per ser tant pacient i agradable amb mi sempre, per treure'm un somriure i per calmar el monstre que tinc a dintre que, a vegades, vol sortir. Abans del Josevi altres m'han patit i/o gaudit. Agrair també a tots aquells que han compartir pis amb mi durant tots aquests anys menjant-se amb patates els dies bons i també els dolents: gràcies a la gent de Sant Eusebi (el **Davik,** el **Kike, l'Elisa** i la **Dèlia**) i el meu estimat amic **Lluis**.

...quan és divendres i vols trobar-te amb la teva gent, la de tota la vida o no, on tot val i tot s'entén perquè et fan sentir sempre com a casa (la família!): gràcies al **Rubén,** a la **Laura**, a **l'Anna**, a la **Rosa**, a la **Mònica**, al **Servando** i a la **Marta.** Gràcies també a les meves nenes amb les que no només he compartit això sinó quasi tota una vida: gràcies a la **Patri**, a la **Susana** i a la **Lorena.** Gràcies també a **l'Ana** pels moments tant especials juntes.

...en tots els moments: gràcies a **la meva mare**, **el meu pare** i la meva cosina **Txell** per formar una família acollidora i agradable i per sempre donar-me suport.

I sobretot gràcies al meu director de tesi, el **Jordi Cama**, perquè sense ell tot això no hagués estat possible. Gràcies per totes les vegades que m'has vist fluixa i m'has aixecat i també per aquelles que m'has vist forta i has compartit amb mi el moment. Ha estat un plaer!

Table of contents

List of figures

List of tables

Part I:

Introduction and Materials and Methods

Chapter 1

Introduction

1.1 Background and objectives

Energy is a key input into almost all activities and is fundamental to society wellbeing. However, as recently reported by the International Energy Agency (IEA), its use represents by far the largest source of greenhouse gas (GHG) emissions (83% in 2011; IEA 2013). Smaller shares correspond to agriculture, producing mainly CH_4 and N_2O from domestic livestock and rice cultivation, and to industrial processes not related to energy, producing mainly fluorinated gases and N_2O.

Fossil fuels currently supply 81% of the energy consumed globally and CO_2 resulting from the oxidation of carbon in fuels during combustion dominates the total GHG emissions (65% in 2010; Fig. 1.1). Total anthropogenic GHG emissions have risen more rapidly from 2000 to 2010 than in the previous three decades and have reached human history record in 2010 (49 ± 4.5 $GtCO_2eq/yr$; Fig. 1.1). The global economic crisis 2007-2008 has temporarily reduced global emissions but not changed the longer-term trend. Whereas more recent data are not available for all gases, initial evidence suggests that growth in global CO_2 emissions from fossil fuel combustion has continued with emissions increasing by about 3% between 2010 and 2011 and by about 1–2% between 2011 and 2012 (IPCC, 2014). These high levels of GHG emissions are the direct source of the global climate change.

The United Nations Framework Convention on Climate Change (UNFCCC) provides a structure for intergovernmental efforts to tackle the challenge posed by climate change. The

Convention's ultimate objective is to stabilize GHG concentrations in the atmosphere at a level that would prevent dangerous anthropogenic interference with the climate system.

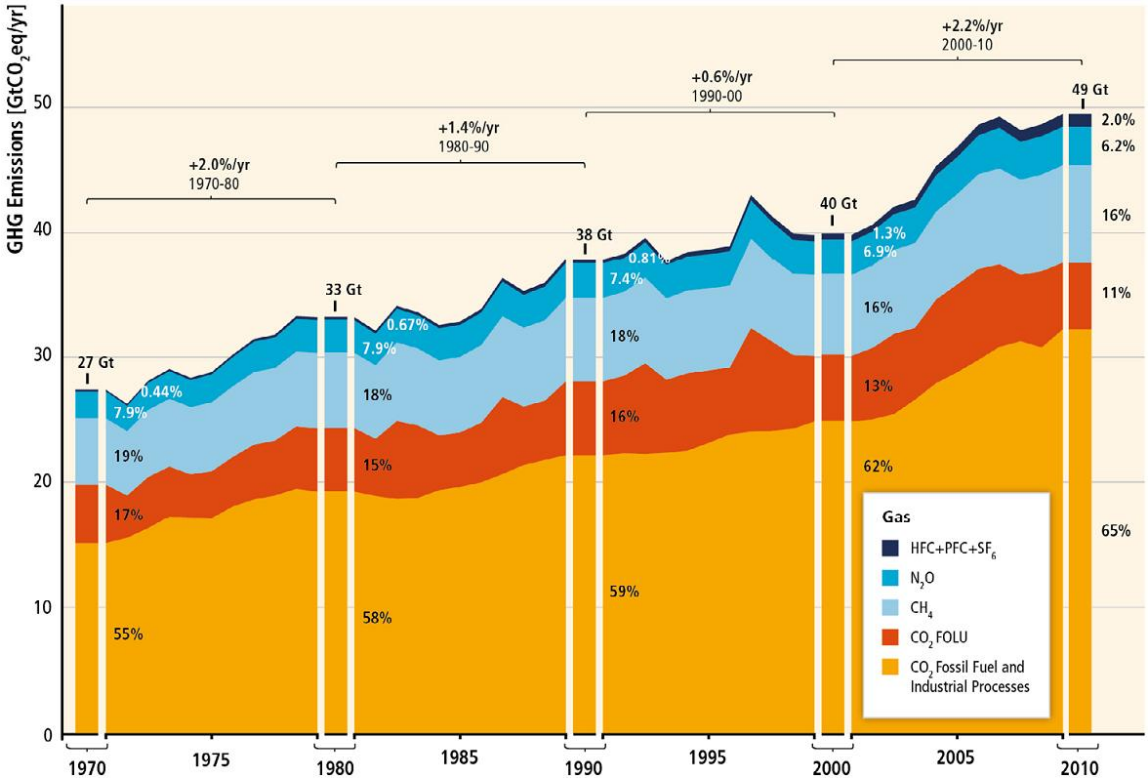

Fig. 1.1 *Total annual anthropogenic GHG emissions ($GtCO_2eq/yr$) by groups of gases 1970-2010: CO_2 from fossil fuel combustion and industrial processes; CO_2 from Forestry and Other Land Use (FOLU); methane (CH_4); nitrous oxide (N_2O); fluorinated gases covered under the Kyoto Protocol (HFC-PFC-SF_6). Average annual growth rate for each decade is highlighted with the brackets (IPCC, 2014).*

The Conference of Parties (COP) in 2010 further recognized that deep cuts in global GHG emissions are required, with a view to hold the increase in global average temperature below 2 ºC above preindustrial levels (IEA, 2013). Consequently, given that continued global economic growth will further increase energy consumption needs, meeting climate challenge will require changes in energy consumption and in the technologies used to produce energy (Global CCS Institute, 2013). However, the deployment of existing and new low-carbon technologies is not an immediate process and may take several decades. Therefore, bridge technologies are needed. Carbon Capture and Sequestration (CCS) may indeed be one of such bridge technologies that will permit the reduction of CO_2 emissions over the coming decades while a change in the energy market occurs (IEA, 2010).

CCS technology consists of the separation of CO_2 from industry and energy-related sources, transport to a storage location and long-term isolation from the atmosphere. Geological storage options for CO_2 include depleted oil and gas reservoirs, use of CO_2 in enhanced oil recovery (CO_2-EOR), use of CO_2 in enhanced coal bed methane recovery, deep-unminable coal seams and deep-saline aquifers. The latter have received particular attention due to their high CO_2 storage capacity and wide availability throughout the world (Bachu and Adams, 2003). However, CO_2-EOR projects currently dominate geological storage. Nowadays, all twelve projects in operation are in industries that separate CO_2 as part of their normal procedures – natural gas processing, fertilizer production, hydrogen production, and synthetic natural gas – and nine of these projects use the captured CO_2 for enhanced oil recovery (EOR). The remainder is dedicated to storage in geological formations containing brine or non-potable water (Global CCS Institute, 2013). The storage capacity of the twelve projects in operation totals 25 Mt/yr and the remaining projects in planning (45 projects) have the potential to store 84 Mt/yr.

The European Energy Programme for Recovery (EEPR) was established in 2009 to address both Europe's economic crisis and European energy policy objectives. Almost €4 billion were assigned to co-finance EU energy projects that would boost the economic recovery, increase the security of energy supply and contribute to the reduction of greenhouse gas emissions. The three sectors meeting these conditions were gas and electricity infrastructure, offshore wind energy and carbon capture and storage (CSS) projects. One of these CCS projects, namely The Compostilla project, is leaded by a three partner consortium (Endesa, CIUDEN (CIUDad de la ENergía foundation) and Foster Wheeler Energia Oy (FWEOy)), and is located in Ponferrada, northern Spain. The project is in charge of three Technology Development Plants (TDPs) at pilot scale: the CO_2 capture and transport TDPs in Cubillos del Sil (León, Spain) and the CO_2 geological storage TDP in Hontomín (Burgos, Spain).

This thesis falls within the context of CO_2 geological storage in Hontomín. The Hontomín reservoir formation for CO_2 storage is a deep saline aquifer in Mesozoic sedimentary sequences that is covered by a very low permeability formation which acts as a cap rock. At the storage TDP, it is programmed to inject less than 100000 tonnes of CO_2 into a 1500-meter-deep dome-like saline aquifer over a period of five years. Five existing wells (H1-5) were used to characterize the structure of the geological formation and two new wells were drilled, one for CO_2 injection (H-I) and another one for monitoring (H-A).

The 100-meter-thick host reservoir rock is mainly composed of limestone (80-85%) and sandstone (15-20%) and has an upper impermeable seal made up of marls, that should prevent escape of CO_2 to the surface, and a lower-impermeable seal mainly composed of anhydrite-containing rock (Fig. 1.2). CO_2 will be stored at depth to ensure an optimal use of the pore space available for storage. Density of CO_2 under a normal geothermal gradient increases rapidly with depth until about 800 meters where CO_2 becomes supercritical (total pressure P > 74 bar and temperature T > 31 ºC) and has a liquid-like density (about 500-800 kg/m^3) that provides the potential for efficient utilization of underground storage space and improves storage security.

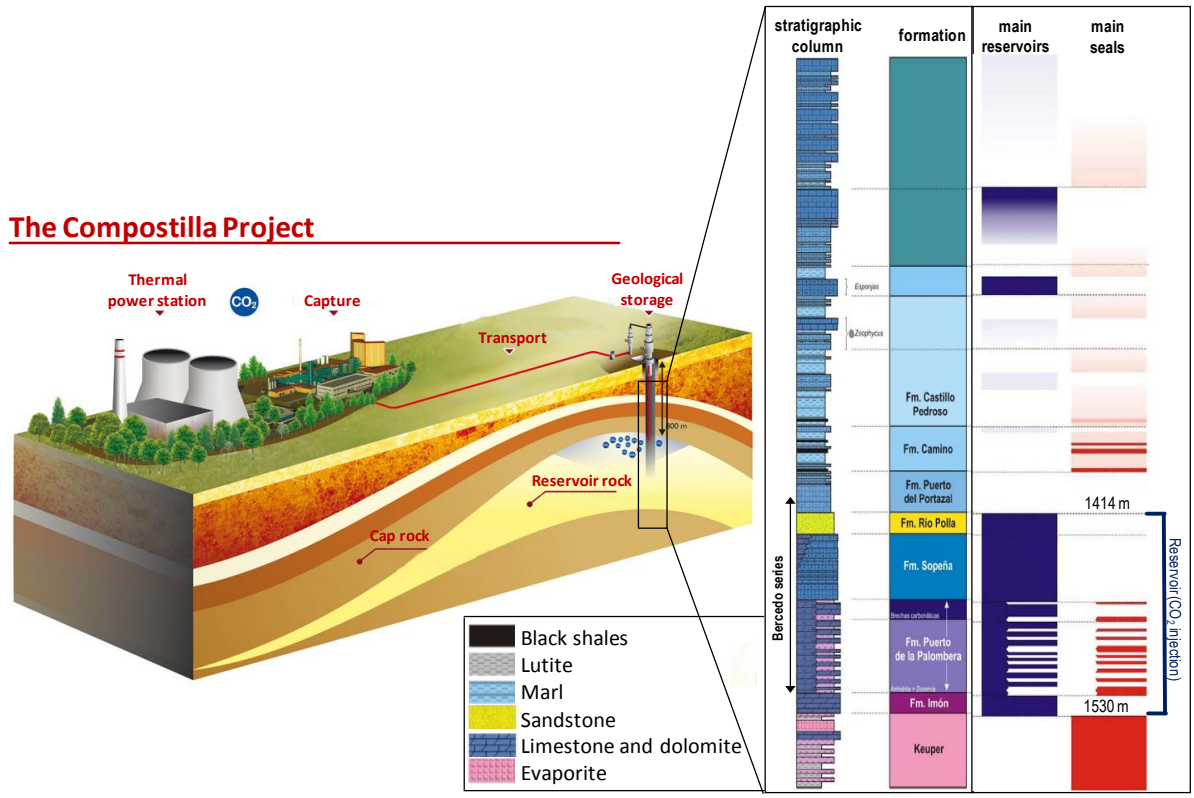

Fig. 1.2 *Scheme of The Compostilla Project (left) and stratigraphic column of the Hontomín site (right; GEOMODELS, University of Barcelona).Depth of CO_2 injection in the reservoir is between 1414-1530 m.*

Once in the reservoir, four trapping mechanisms can contribute to CO_2 retention over long periods (IPCC, 2005): stratigraphic trapping, solubility trapping, capillary trapping, and mineral trapping. The relative importance of these processes is expected to change over time as CO_2 migrates and reacts with the rocks and fluids. First, supercritical CO_2 is lighter and much less viscous than resident saline water (30-40% less viscous). Therefore, it will tend to

float until it reaches a low permeability, high-entry-pressure and mechanically stable cap rock that traps it. As a result, a CO_2-phase bubble will tend to form at the aquifer top (stratigraphic trapping). Then, the dissolution of CO_2 into the pore water can lead to trapping by solubility. The amount of gas that can dissolve into the water depends on several factors, most notably temperature, pressure and salinity of the brine (*e.g.*, Koschel et al., 2006; Oldenburg, 2007; Spycher et al., 2003). At the conditions expected for most geological sequestration (ambient to 100 ºC and a few hundred bars of total pressure), CO_2 solubility increases with increasing pressure (*i.e.*, depth) but decreases with increasing temperature and salinity. A consequence of dissolution is that the CO_2- rich water is 1-2% denser than the resident saline water (Yang and Gu, 2006) and it tends to move downwards to the bottom of the reservoir. Given that CO_2 dissolution may be rate-limited by the magnitude of the contact area between the CO_2 and the fluid phase, this downflow of dissolved CO_2-rich water will certainly contribute to CO_2 dissolution (Hidalgo and Carrera, 2009). Another trapping mechanism occurs after injection stops. Groundwater tends to fill back to the pore space and a sizable amount of CO_2 will remain trapped as residual CO_2 bubbles (capillary trapping). Finally, mineral trapping can take place when dissolved CO_2 reacts with minerals in the geologic formation, promoting precipitation of carbonate minerals (Oelkers et al., 2008). Mineral trapping is attractive because it could immobilize CO_2 for very long periods (Gunter et al., 1997). However, the process is thought to be comparatively slow because it depends on dissolution of silicate minerals, so the overall impact may not be realized for at least tens to hundreds of years (Benson and Cole, 2008).

This thesis deals with the interaction between the saline solution and the reservoir rock at Hontomín when injection of supercritical CO_2 is performed. The resident saline groundwater is sulfate-rich, equilibrated with calcite, dolomite and gypsum, with neutral pH and an ionic strength of 0.6 M (Table 1.1). Injection of supercritical CO_2 will lead to the formation of a CO_2-rich acid solution which will promote the dissolution of carbonate minerals (*e.g.*, Gherardi et al., 2007; Nogues et al., 2013; Smith et al., 2013) and in minor proportion dissolution of silicate minerals (*e.g.*, Bertier et al., 2006; Fisher et al., 2010; Wigand et al., 2008). Since the resident groundwater contains sulfate, secondary sulfate-rich mineral precipitation (gypsum or anhydrite) may occur. These reactions imply changes in the porosity, permeability and pore structure of the repository rocks.

Table 1.1 *Average composition of the Hontomín groundwater (± 10%) in terms of total concentration (mol/kgw) and pH. It was provided by CIUDEN after extraction from the H-2 well.*

Ca	SO_4^{2-}	Mg	K	Na	Cl^-	HCO_3^-	pH
4.62E-02	2.07E-02	3.72E-02	1.23E-02	4.14E-01	5.35E-01	4.90E-03	≈ 6.9

Hydrodynamic and geochemical processes responsible for trapping CO_2 in geological formations over long time frames have been extensively studied (*e.g.*, Bachu and Adams, 2003; Bachu et al., 1994; Espinoza et al., 2011; Gaus, 2010; Gunter et al., 1997, 2004; Johnson et al, 2001; Kaszuba et al., 2005; Knauss et al., 2005; Xu et al., 2005). In deep saline aquifers, the interaction between dissolved CO_2 in groundwater and carbonate and siliciclastic minerals controls the aqueous inorganic system (Bachu and Adams, 2003). Uncertainties in the mineral reaction rates may generate unreliable estimations of the CO_2-sequestration capacity. It is essential, therefore, to understand the dissolution and precipitation kinetics of the carbonate minerals (calcite, dolomite, magnesite or siderite).

Several studies have focused on the dependence of dissolution rates of pure carbonate minerals on pH, temperature, CO_2 partial pressure, presence of inhibitor ions and ionic strength (De Giudici, 2002; Gledhill and Morse, 2006; Morse and Arvidson, 2002; Plummer et al., 1978; Pokrovsky et al., 2005, 2009; Sjöberg and Rickard, 1984; Xu and Higgins, 2011). Earlier works have shown that calcite dissolution kinetics is strongly pH dependent at high undersaturations and pH $\leq$ 4, and Pokrovsky et al. (2005, 2009) demonstrated that the effect of CO_2 partial pressure is not significant compared with that of pH. Research on the influence of reactor inhibitors on calcite dissolution kinetics has shown that calcite dissolution is retarded in the presence of aqueous divalent cations at neutral to basic pH (Arvidson et al., 2006; Martin-Garin et al., 2003; Morse and Arvidson, 2002), but it does not seem to be affected under acidic conditions (Alkattan et al., 2002).

In the framework of CO_2 geological storage, CO_2-water-rock interaction at elevated temperature and pressure has been studied in detail in closed reactors (Chopping and Kaszuba, 2012; Kaszuba et al., 2003, 2005; Lu et al., 2012; Palandri and Kharaka, 2005; Rimmelé et al., 2010; Rosenbauer et al., 2005). However, the transport processes that are able to control or at least affect the reaction paths during CO_2 injection have not been taken into account. This transport effect has been studied in reactive flow-through experiments (*e.g.*, Luquot et al., 2013; Nogues et al., 2013; Noiriel et al., 2004, 2005, 2009). Luquot and Gouze (2009) performed percolation experiments under different *P-T-p*CO_2 conditions that are

found in deep saline aquifers. The results enabled them to describe mass transfer processes at different distances from the injection well. Smith et al. (2013) conducted core-flood experiments at 30 bar of pCO_2 and 60 °C with dolostone and limestone cores to gain insight into the effect of physical and chemical heterogeneity on the development of distinct reaction fronts. Elkhoury et al. (2013) performed experiments and numerical simulations to shed light on the influence of coupled geochemical alteration and mechanical deformation on calcium carbonate fracture geometry. However, in none of these studies was the importance of the coupled reactions of carbonate dissolution and gypsum precipitation assessed since the injected solutions consisted of sulfate-free brines. Singurindy and Berkowitz (2003) studied the effect of simultaneous calcium carbonate dissolution and gypsum precipitation on the evolution of hydraulic conductivity and flow patterns using columns experiments. Atanassova et al. (2013) evaluated the inhibitory effect of gypsum precipitation on calcite dissolution in acid, sulfate-rich solutions in flow-through experiments. However, these two studies were limited to atmospheric pCO_2 conditions.

Therefore, experimental knowledge about the overall process of gypsum precipitation at the expense of carbonate mineral dissolution in CO_2-rich solutions and its implication for porosity changes in limestone and dolostone reservoir rocks is scarce. ***Part II-crushed rock*** seeks to better understand these coupled reactions by assessing the effect that P, pCO_2, T, mineralogy, acidity and solution saturation state exert on these reactions. Thus, column experiments using limestone and dolostone grains and 1D reactive transport simulations were performed.

The Hontomín reservoir rock is a fractured system mainly composed of low-permeability rocks (Alcalde et al., 2014), where fractures serve as conduits for flow. In this situation long-lasting flow of fluids in disequilibrium with the rock is expected. Dissolution and precipitation processes can alter the geometry of fractures and, consequently, their hydraulic and transport properties (Noiriel et al., 2013).

Prediction of the changes in the flow and transport properties of fractures is still a challenge due to the complexity of fluid-rock interactions and the uncertain role of fracture heterogeneity. The macroscopic physical properties, such as fracture permeability, are directly related to the microstructure of the fracture, which makes the determination of fracture geometry an important issue to model flow and transport (Gouze et al., 2003; Noiriel et al., 2013; Szymczak and Ladd, 2009). Experiments conducted at the laboratory scale are

needed for this kind of characterization. In porous media, the impact of heterogeneities on the evolution of permeability and dissolution patterns has already been evaluated (Carroll et al., 2012; Luquot et al., 2014; Smith et al., 2013). Smith et al. (2013) performed core-flood experiments involving CO_2-rich brines and carbonate rocks and reported the formation of stable or unstable dissolution fronts depending on the degree of pore space heterogeneity. Their results were further investigated using 3D reactive transport models by Hao et al. (2013).

Several experimental studies have been performed to investigate fracture evolution during dissolution using non-destructive techniques (*e.g.*, nuclear magnetic resonance imaging (NMRI), X-ray computed microtomography (XCMT),…), which allow characterization of fracture geometry and flow during dynamic experiments (Detwiler, 2008; Detwiler et al., 2003; Dijk et al., 2002; Ellis et al., 2011; Gouze et al., 2003; Liu et al., 2005; Noiriel et al., 2007, 2013).

Evolution of fracture structure is directly related to fluid flow and mineral dissolution rates. Feedback between fluid flow, solute transport and mineral dissolution may lead to the formation of preferential flow paths (wormholes) under certain flow and reactivity conditions (Szymczak and Ladd, 2009). Experimental studies about dissolution patterns in a variety of porous systems (Golfier et al., 2002; Hoefner and Fogler, 1988) and in single rock fractures (Detwiler, 2008; Detwiler et al., 2003; Dijk et al., 2002; Durham et al., 2001; Gouze et al., 2003; Polak et al., 2004) have already been carried out, but the physicochemical mechanisms behind pattern formation are not yet understood in detail. Moreover, theoretical and computational models have been developed to predict this physical and chemical alteration of the fractures depending on the relative rates of transport and reaction (Péclet and Damköhler numbers) but only a few of them have been contrasted against experimental data (*e.g.*, Elkhoury et al., 2013).

Part III-Fractured cores deals with the influence of the flow rate on dissolution and precipitation features during percolation experiments with fractured limestone and sandstone cores. Fracture permeability was measured and X-ray computed microtomography was used to characterize changes in fracture volume induced by dissolution and precipitation processes. Thereafter, dissolution/precipitation-induced volume changes and variation in permeability were compared between the two reservoir rocks to evaluate their potential changes in storage

capacity and injectivity. Additionally, 2D reactive transport modeling was performed to estimate flow and reaction kinetics parameters by reproducing the experimental results.

1.2 Thesis outline

This thesis is organized in four parts and six chapters. *Chapters 2*, *3* and *4* are based on published or submitted papers and *Chapter 5* is currently in preparation for publication.

Part I-Introduction and materials and methods – *Chapters 1* and *2*

- *Chapter 1* describes the motivation and scientific context of this study, together with the state of the art and the objectives.
- *Chapter 2* presents a detailed description of (i) the experimental methodology followed to perform the column and percolation experiments (fractured cores) and (ii) the parameters used in the 1D and 2D modeling of these experiments.

Part II-Crushed rock – *Chapter 3*

- *Chapter 3* presents and discusses the experimental and modeling results of the column experiments run at different *P*-*p*CO_2-*T* conditions. The effect of *P*, *p*CO_2, *T*, mineralogy, acidity and solution saturation state on dissolution and precipitation reactions is assessed. 1D reactive transport calculations allow quantification of the mineral reaction rates and porosity variation.

Part III-Fractured cores – *Chapters 4* and *5*

- *Chapter 4* shows the flow rate effect on dissolution and precipitation features in the percolation experiments with fractured limestone and sandstone cores. Changes in permeability and fracture volume are evaluated.
- *Chapter 5* is divided into two sections. The first one compares the changes in fracture volumes and permeability between fractured limestone and sandstone cores. The second one shows the 2D reactive transport simulations of these experiments.

Part IV-Conclusions – *Chapter 6*

- *Chapter 6* provides a summary of the main contributions of this thesis.

Two appendixes are supplied:

- *Appendix A* provides the model parameters used to perform the 1D simulations of the column experiments and the 2D simulations of the percolation experiments (fractured cores).
- *Appendix B* includes additional experimental and modeling results from the column experiments.

Chapter 2

Materials and methods

2.1 Experimental methodology

This section describes the experimental procedure followed to perform the column experiments presented in *Part II: crushed rock* and the percolation experiments with fractured cores shown in *Part III: fractured cores*. Analytical techniques used to characterize rock samples and injected solutions are detailed. In addition, the different experimental equipments used under different *P* conditions and the mass transfer and fracture permeability calculations are described.

2.1.1 Sample characterization and analytical techniques

Four different sedimentary rock samples were used in this study: vuggy limestone, dolostone, oolitic limestone and sandstone. The vuggy limestone, the oolitic limestone and the sandstone were provided by CIUDEN and belong to the Bercedo series and different formations in the Hontomín reservoir rock (Fig 1.2; Table 2.1; Pujalte et al., 1998). The dolostone was provided by the Department of Mineralogy (Faculty of Geology, Barcelona University) and comes from Peñarroya, Teruel (Spain). The mineralogical composition of the samples was obtained by X-ray diffraction (XRD), performed using a Bruker diffractometer model D-5005 with Cu K- α1 radiation, and Rietveld analysis (Young, 1995) (Table 2.1).

The vuggy limestone and the dolostone rock samples were used to carry out the column experiments that are presented in *Part II: crushed rock* and the oolitic limestone and the sandstone rock samples were used to perform the percolation experiments with fractured cores that are shown in *Part III: fractured cores* (Table 2.1).

Table 2.1 *Rock samples: origin and mineralogical composition (wt.%). See also Fig. 1.2.*

Sample	Experiments	Series Formation	Mineralogical composition (wt.%) (XRD and Rietveld)			
			Calcite	Dolomite	Quartz	Microcline
Vuggy Limestone	*Part II: crushed rock*	Bercedo Puerto de la Palombera	90.7	9.3	-	-
Dolostone		-	-	100	-	-
Oolitic limestone	*Part III: fractured cores*	Bercedo Sopeña	100	-	-	-
Sandstone*		Bercedo Areniscas del Río Polla	65.7	-	27.8	6.5

*coarse-grained sandy limestone according to Mount (1985).

Rock samples used in the column experiments (*Part II: crushed rock*) were crushed to a grain size between 1 and 2 mm for the atmospheric and 10 bar pCO_2 experiments. For the 34 bar pCO_2 experiment, the limestone was ground to a grain size between 250 and 500 μm owing to the smaller diameter of the column (Fig. 2.1). Thereafter, in order to remove microparticles due to grinding, the crushed and ground samples were washed three times with pH 1 solution (HCl) and three times with deionized water. Finally, the washed samples were dried in the oven at 40 °C and were put into cylindrical columns.

X-ray fluorescence analysis of the vuggy limestone and the dolostone was performed using a Bruker spectrometer model AXS-S2 Ranger to identify minor-element composition. In the limestone sample, Ca and Mg were the major elements, Si (0.37 wt.%) and Fe (0.20 wt.%) appeared as minor components and S and Sr as trace elements (< 0.1 wt.%). In the dolostone sample, Al, Si, S, Mn and Cl appeared as minor components (from 0.1 wt.% to 1 wt.%) and Cu, Pb and K as trace elements. Fe (1.48 wt.%) was the only element, besides Ca and Mg, with a concentration higher than 1 wt.%.

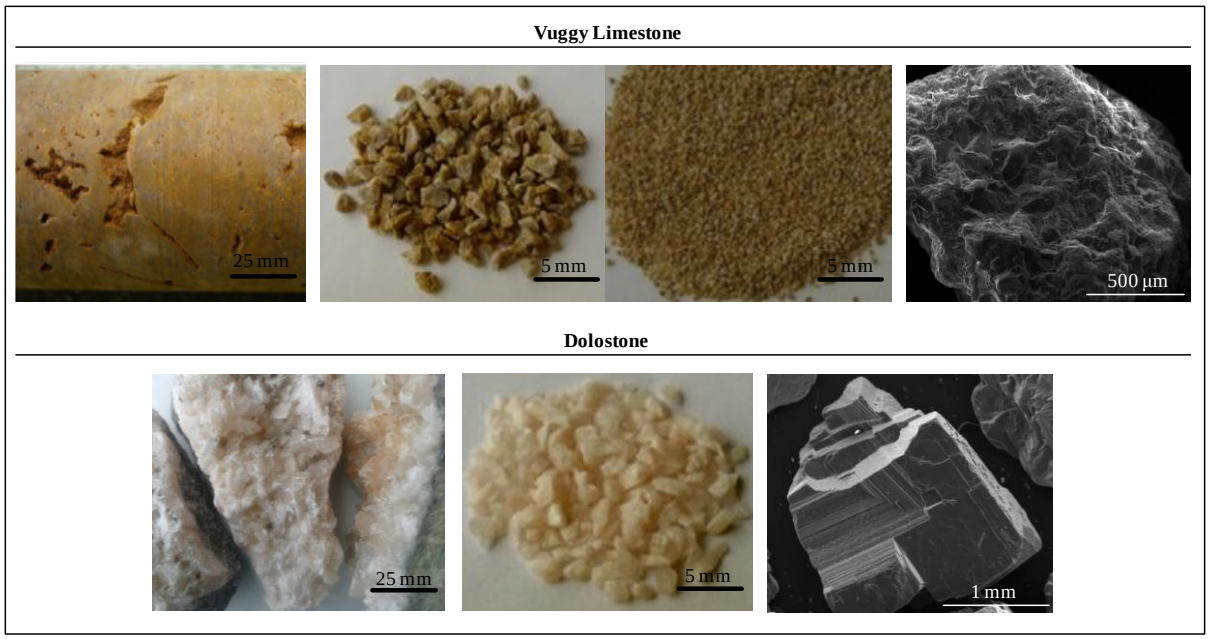

Fig. 2.1 *Rock samples used in the column experiments described in Part II: crushed rock. Top: vuggy limestone (core, crushed grains (1-2 mm)/ground grains (250-500 µm) and SEM image); bottom: dolostone (fragments, crushed grains (1-2 mm) and SEM image).*

Flow-through experiments with the dolostone rock sample were conducted to obtain dolomite dissolution rates at different pH values from 1.5 to 3.5. Assuming stoichiometric dolomite dissolution, the Ca/Mg ratio measured from the steady-state output Ca and Mg concentrations was used to obtain the structural formula of dolomite ($Ca_{1.048}Mg_{0.952}(CO_3)_2$).

Scanning electron microscopy (SEM) was performed on C-coated samples before and after the column experiments using a Hitachi H-4100 instrument under a 15-20 kV potential. The surface of the unreacted limestone grains was rough, whereas the surface of unreacted dolostone grains was flat and terraced. Microparticles attached onto the surfaces were not observed (Fig. 2.1).

Cylindrical rock cores used in *Part III: fractured cores* were cored side-by-side from the provided samples. Fifteen cores of 9 mm in diameter (d) and 18 mm in length (L) were obtained; six limestone cores and nine sandstone cores. Limestone and sandstone porosities were 5% and 6%, respectively, as reported by CIUDEN (ALM-09-008, 2010). The permeability of the rock cores ($k < 10^{-18}$ m^2) was measured by performing a permeability test using the Icare Lab CSS II apparatus (Luquot et al., 2012). Thereafter, a fracture was artificially created by sawing each core with a circular saw, during which formation of micro-cracks could happen. Nonetheless, as discussed in *Section 4.2.4.1*, their existence did not

intervene in the overall fracture dissolution. To guarantee flow exclusively through the fracture, all fractures were laterally sealed using a fiber glass thread and Duralco 4525 epoxy resin (stable mechanical and chemical properties up to 690 bar, 260 ºC and low pH) (Fig. 2.2a).

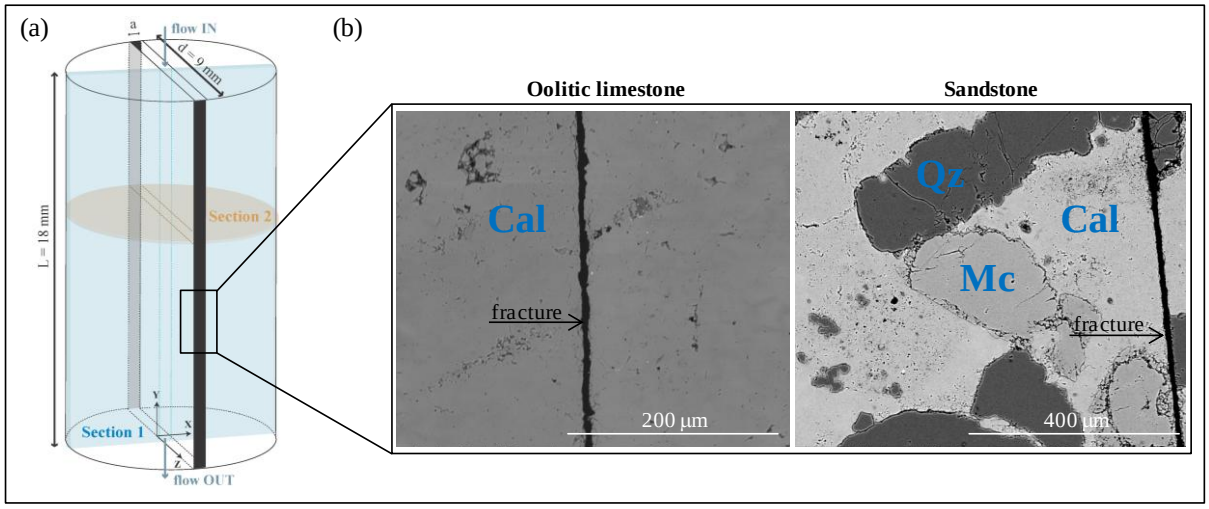

Fig. 2.2 *Fracture core dimensions (a) and SEM images (b) of the rock samples used in the percolation experiments with fractured cores shown in Part III: fractured cores. Cal = calcite; Qz = quartz and Mc = microcline.*

Some fractured cores were characterized by XCMT before and after the experiments. Data was acquired at the National Institute for Lasers, Plasma and Radiation Physics (NILPRP) (Bucharest-Magurele, Romania) using the Cone beam CT rapid scan (180° + ½ fan angle), Oblique View Cone Beam. X-ray energy was 225 kVp and maximum power was 10/15 W, using a tungsten filament source. The cores were mounted on a rotary stage, and images were collected every 0.5º. The linear detector, using 1,024 scintillator-photo diode assemblies, yielded 16-bit output digital files. The resulting pixel size was 14 µm. The processing of these X-ray microtomography data was carried out by Voxaya (Montpellier, France), providing characterization of the fracture geometry. Segmentation of the images was performed using the method "edge based snakes" (Yushkevich et al., 2006) and error calculation was carried out by changing the iteration number which corresponds to the propagated time of the segmented volume. Calculated errors of fracture volumes ranged from 0.4% to 5.6%.

After the reacted samples had been scanned, the cores were flooded with epoxy to allow sectioning and further analysis with SEM. The reacted cores were sectioned along different planes perpendicular to the fracture depending on fracture evolution (sections 1 and 2 in Fig. 2.2a). SEM analyses were performed using a Hitachi H-4100 instrument under a 15-20 kV potential to obtain the dimensions of the fracture and observe features of mineral dissolution and precipitation (Fig. 2.2b)

MicroRaman spectra, using a Jobin-Yvon LabRam HR 800 apparatus equipped with an Olympus BXFM microscope and using a wavelength of 532 nm, were obtained to identify the secondary phases in the reacted fractured cores.

2.1.2 Injected solutions

Two types of solutions were prepared. The first type was a synthetic version of the Hontomín groundwater, which is nearly in equilibrium with calcite, dolomite and gypsum/anhydrite, with a 0.6 M ionic strength and neutral pH (Table 1.1). Four modifications of this solution (named gypsum-equilibrated solution, *gp-e*) were performed varying gypsum saturation state and acidity, and yielding one solution undersaturated with respect to gypsum (gypsum-undersaturated solution, *gp-u*), one solution sulfate-free (*no-s*) and two acidic gypsum-equilibrated solutions (pH 2.1 acid solution, *a2.1*; pH 3.5 acid solution, *a3.5*) (Table 2.2). TDS of these solutions was around 30 g/L. Solutions were prepared by adding appropriate amounts of reagents $CaCl_2 \cdot 2H_2O$, $MgCl_2 \cdot 6H_2O$, NaCl, KCl, Na_2SO_4 and NaBr to Millipore MQ water (18 MΩ·cm) at room *T* (25 ± 2 ºC) and under atmospheric pressure. The amounts of reagents were based on equilibrium calculations using the CrunchFlow code (Steefel, 2009) and the EQ3/6 database (Wolery et al., 1990). The solubility product of gypsum was that included in the database ($\log K_{Gp}$ = -4.4729 at *T* = 25 ºC). However, in the gypsum-equilibrated solutions unexpected precipitation of gypsum (≈ 1.3 g in 2 L solution) occurred while stirring the solutions for 12 h. Thus, final mixtures were filtered using a 0.22 μm filter to eliminate the precipitated gypsum particles and analyzed to measure the total concentrations by inductively coupled plasma-atomic emission spectrometry (ICP-AES) using a Thermo-Jarrel Ash spectrometer equipped with a CID detector (Table 2.2). The detection limits for Ca, S, Mg, K, Na and Fe were 1.25×10^{-6} M, 1.34×10^{-6} M, 2.06×10^{-6} M, 1.28×10^{-6} M, 1.30×10^{-4} M and 3.58×10^{-7} M, respectively. Using the measured equilibrium concentrations, a new $\log K_{Gp}$ value was calculated to be $\log K_{Gp\text{-}25}$ = -4.5978 at *T*

= 25 ºC. Hence, applying the same correction factor at different temperatures, the newly obtained $logK_{Gp\text{-}40}$ and $logK_{Gp\text{-}60}$ were -4.6368 (40 °C) and -4.7383 (60 °C). These values turned out to be similar to those recently reported by Nordstrom (2013). The new gypsum logK values at 25, 40 and 60 °C were used in the calculations of this study.

For the atmospheric pCO_2 experiments the solutions were acidified to pH 2.1 and pH 3.5 (*a2.1* and *a3.5* input solutions) by adding appropriate amounts of 1M HCl solution. For the rest of experiments run under pCO_2 higher than the atmospheric one, the acidity of the solution was obtained from dissolution of CO_2. Relationship between CO_2 partial pressure and aqueous CO_2 concentration, as well as the saturation state of the injected solutions under the experimental conditions were calculated using the PhreeqC (v.3) code (Parkhurst and Appelo, 2013) and the PhreeqC database (Table 2.2). The aqueous solubility of CO_2 is temperature, pressure and ionic strength dependent, generally lower at elevated temperature and salinity and higher at elevated pressure (Duan and Sun, 2003; Takenouchi and Kennedy, 1964). pH and saturation indexes (SI) of input solutions injected in experiments performed under P = 150 bar were calculated using PhreeqC-v.3 (P effect included) and CrunchFlow (P effect not included) to quantify the non-linear effect of P (P > 20 bar) on CO_2 solubility and mineral equilibria (through the molar volume of solutes) reported by Appelo et al. (2014) (Table 2.2).

The second type of prepared solution was a sulfuric acid solution (H_2SO_4, pH = 2.5; TDS = 1.2 g/L) in equilibrium with gypsum at T = 25 °C (Table 2.2; H_2SO_4 solution, *s*). 3.162 mL of 1 M H_2SO_4 solution were poured into 2 L of Millipore MQ water. Then, approximately 20 g of fragmented gypsum were added and the mixture was stirred for 12 h. Finally, gypsum-equilibrated solutions were filtered using a 0.22 μm filter.

Five input solutions were used to perform the column experiments presented in *Part II: crushed rock* and three input solutions were used to run percolation experiment through fractured cores shown in *Part III: fractured cores* (Table 2.2).

Table 2.2 *Injected solutions: amount of reagents, experimental conditions, average concentration (from ICP-AES), experimental pH, and calculated saturation indexes (SI), pH and ionic strength (I).*

Input label	*s*	*a3.5*		*a2.1*		*gp-u*			*gp-e*					*no-s*
reactant mass (g) in 2L MQ water														
$CaCl_2{\cdot}2H_2O$	-	16.12				12.67			16.12					12.67
$MgCl_2{\cdot}6H_2O$	-	13.34				13.34			13.34					13.33
NaCl	-	37.84				40.57			37.84					45.05
KCl	-	1.69				1.69			1.69					1.69
Na_2SO_4	-	8.77				5.45			8.77					-
NaBr	-	2.34				2.34			2.34					2.34
Exp. Label	L25-atm-s	L25-atm-a3.5	L60-atm-a3.5	L25-atm-a2.1	L60-atm-a2.1	L25-10-gp-u	L40-10-gp-u		L25-10-gp-e	L40-10-gp-e	L60-10-gp-e	L60-34-gp-e		
Part II: Crushed rock	D25-atm-s									D40-10-gp-e				
Exp. Label													L0.2-gp-e, L1-gp-e, L5-gp-e, L60-gp-e,	L1-no-s, L60-no-s,
Part III: Fractured cores								S5-gp-u, S60-gp-u					S0.2-gp-e, S1-gp-e, S5-gp-e, S60-gp-e	S1-no-s, S5-no-s, S60-no-s
experimental conditions														
***T* (°C)**	25	25	60	25	60	25	40	60	25	40	60		60	60
***P* (bar)**	1					10		150	10			150	150	150
***p* CO_2 (bar)**	$10^{-3.5}$					10		62	10			34	62	62
[1]average concentration (mol/kgw) and experimental pH														
Ca^{2+}	1.55E-02	5.30E-02		4.83E-02		4.40E-02			4.94E-02					4.15E-02
SO_4^{2-}	1.85E-02	2.90E-02		2.74E-02		1.92E-02			2.68E-02					-
Mg^{2+}	1.73E-04	3.28E-02		3.22E-02		3.33E-02			3.26E-02					3.34E-02
K^+	-	1.19E-02		1.12E-02		1.15E-02			1.14E-02					1.16E-02
Na^+	-	4.02E-01		3.77E-01		3.99E-01			3.92E-01					3.99E-01
Cl^-	-	5.18E-01		5.14E-01		5.15E-01			5.02E-01					5.48E-01
Br^-	-	1.13E-02		1.13E-02		1.14E-02			1.14E-02					1.14E-02
CO_2	1.29E-05	1.30E-05	6.25E-06	1.29E-05	6.23E-06	2.79E-01	2.02E-01	6,15E-01	2.79E-01	2.02E-01	1.43E-01	3.85E-01	6.15E-01	6.15E-01
pH	2.50	3.50		2.10		3.56	3.65	-	3.51	3.62	3.73	-	-	-
[2]SI, pH and I (CrunhFlow and PhreeqC-v.3)														
Cal	-10.34	-8.01	-7.77	-10.84	-10.60	-3.45	-3.22	-3.03 (-3.35)	-3.48	-3.21	-2.88	-2.96 (-3.25)	-3.01 (-3.32)	-3.10 (-3.46)
Dol	-23.19	-16.55	-15.74	-22.18	-21.36	-7.34	-6.71	-6.16 (-6.48)	-7.47	-6.77	-5.96	-6.07 (-6.35)	-	-
Gp-25	0.09	0.05	-	-0.03	-	-0.19	-	-	0.003	-	-	-	-	-
Gp-40	-	-	-	-	-	-	-0.20	-	-	0.006	-	-	-	-
Gp-60	-	-	0.04	-	-0.09	-	-	-0.21 (-0.24)	-	-	-0.03	-0.04 (-0.07)	-0.01 (-0.05)	-
pH	2.50	3.50		2.10		3.65	3.70	3.40 (3.26)	3.61	3.68	3.78	3.53 (3.40)	3.40 (3.26)	3.37 (3.21)
I	0.05	0.63	0.62	0.61	0.59	0.60	0.61	0.60	0.61	0.62	0.58	0.6	0.62	0.64

[1] refers to the average concentrations of several prepared solutions of the same type. The largest %RSD (relative standard deviation) of the average concentration in *s* , *a2.1-3.5* , *gp-u* , *gp-e* and *no-s* solutions is 2 (for SO_4^{2-}), 0.8 (for Ca^{2+}), 3.5 (for Mg^{2+}), 4.9 (for SO_4^{2-}) and 1.2 (for Mg^{2+}), respectively.

[2] SI, I and pH values are calculated using CrunchFlow and SI and pH values in brackets are calculated using PhreeqC-v.3.

Relationship between *p* CO_2 and aqueous CO_2 concentration was calculated using PhreeqC-v.3.

TDS (Total Dissolved Solids) of all solutions is around 30 g/L except for solution *s* which is 1.2 g/L.

Cal = calcite; Dol = dolomite; Gp = gypsum; *s* = H_2SO_4 solution; *a3.5* = acid solution pH 3.5; *a2.1* = acid solution pH 2.1; *gp-u* = gypsum-undersaturated solution; *gp-e* = gypsum-equilibrated solution; *no-s* = sulfate-free solution.

a3.5 and *a2.1* input solutions were acidified to pH 3.5 and 2.1 by adding appropriate amounts of 1M HCl solution.

2.1.3 Experimental setups and conditions

Three experimental setups were used to work under three different *P* conditions (*P* = 1, 10 and 150 bar) in the column experiments presented in *Part II: crushed rock* and two experimental setups were used to work under *P* = 150 bar in the percolation experiments with fractured cores shown in *Part III: fractured cores* (Fig. 2.3). Experiments run at *P* = 1 bar and *P* = 10 bar were carried out at the IDAEA-CSIC laboratory (Barcelona, Spain) and the experiments conducted at *P* = 150 bar were performed at the Geosciences Department of Montpellier University-CNRS (Montpellier, France).

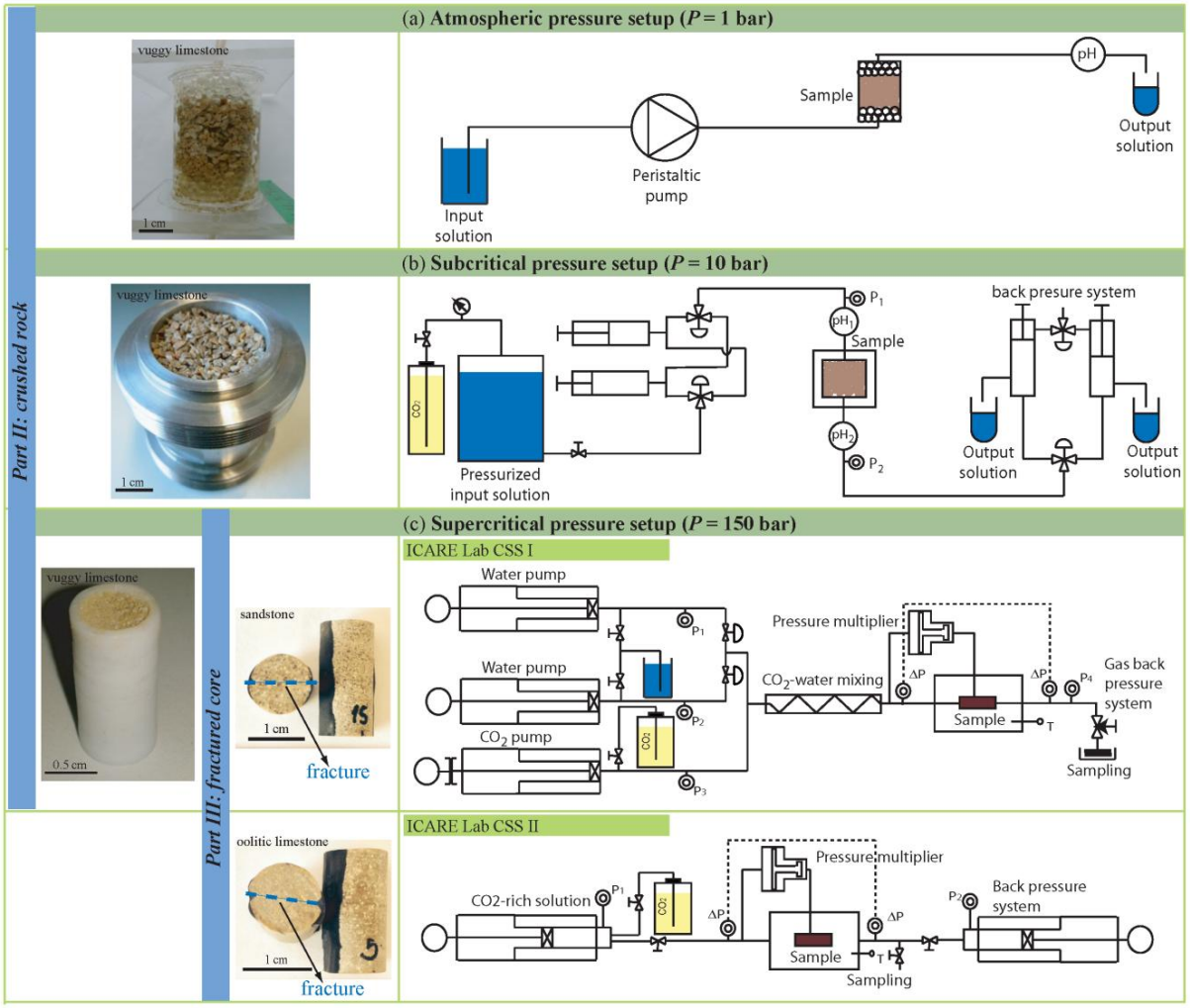

Fig. 2.3 *Experimental setups used to work under atmospheric (a), subcritical (b) and supercritical (c) CO_2 conditions.*

2.1.3.1 Atmospheric pressure setup (*P* = 1 bar)

Transparent methacrylate cylindrical columns of 2.6 cm in inner diameter (*d*) and 4 cm in length (*L*) were filled with approximately 20 g of crushed rock fragments with a grain size of 1-2 mm. A bed of glass beads of 0.7 mm in diameter was placed at the top and bottom of the cylinder to homogenize the inlet and outlet solutions. The thickness of the beds was about 0.7 cm, yielding an effective column volume (V_{bulk}) of 13.80 cm^3 (Fig. 2.3a). A 0.22 μm filter was placed at the top of the column to prevent any particle release into the output solution. Column porosity was calculated using the mass of the rock sample, the density of the rock and the effective column volume. The density of the vuggy limestone (2.72 g/cm^3) was obtained from the weight fractions of calcite (90.7 wt.%) and dolomite (9.3 wt.%) and the respective densities (2.71 g/cm^3 and 2.86 g/cm^3; Downs, 2006). Initial porosities ranged between 45% and 48%. Given the mineral mass, the rock density and the effective column volume, and assuming that the rock fragments were spheres of 1.5 mm in diameter, the geometric surface areas of vuggy limestone and dolostone fragments were approximately 2000 m^2_m/m^3_{bulk} (m: mineral; bulk: column).

Input solutions were injected from bottom to top of the column using a peristaltic pump under a constant flow rate of 0.021 ± 0.002 mL/min. The outlet solution was periodically collected. Darcy velocity ranged from 6.28×10^{-7} to 7.06×10^{-7} $m^3/m^2/s$, yielding residence times (τ) between 4.6 and 5.6 h (Table 3.1). Collected samples were immediately acidified with 1% HNO_3 to avoid changes in chemical composition. Most of the experiments were undertaken at room temperature (22-25 °C). For the experiments performed at 60 °C the columns were fully immersed in a thermostatic bath. Input and output pH at the desired temperature was measured with a conventional glass pH electrode (accuracy ± 0.02) that was calibrated using Crison buffer solutions of pH 2.02 and 7.00. Total input and output concentrations were measured by ICP-AES (see *Section 2.1.2*).

2.1.3.2 Subcritical pressure setup (*P* = 10 bar)

The experimental setup was completely designed and assembled at the Geosciences Department of the IDAEA-CSIC in collaboration with the GASLI company, a manufacturer of pressure gauges and measurement instruments located in Barcelona (Spain).

A 316 stainless steel column (3.2 cm in diameter (*d*) and 6 cm in length (*L*)) was filled with approximately 60 g of crushed rock fragments with a grain size of 1-2 mm. The mass of

the sample was weighed before and after the experiments. Two plastic filter screens of 1 mm thickness were placed at the top and bottom of the cylinder to homogenize the inlet and outlet solutions. Two pieces of 0.45 μm stainless steel mesh were likewise placed at the bottom and the top of the reaction cell to prevent any particle release into the output solution. The effective column volume (V_{bulk}) was 43.43 cm^3 (Fig. 2.3b). Initial porosities calculated using the same approach as in the atmospheric pressure setup ranged between 47% and 53%. Given the mineral mass, the rock density and the effective column volume, and assuming that the fragments were spheres of 1.5 mm in diameter, the geometric surface areas of vuggy limestone and dolostone fragments were approximately 2000 m^2_m/m^3_{bulk}.

The input solution (2.5 L) was poured into the Teflon-coated pressurized storage tank of 3 L capacity. Sufficient head space was left to inject CO_2 gas under the desired pressure (P = 10 bar). To ensure that CO_2 was the only gas phase in contact with the solution, air was removed airing the head space with CO_2 gas for 15 min approximately. Thereafter, to guarantee that the input solution was equilibrated with CO_2 before injection, the valve that connects the CO_2 bottle with the storage tank was alternatively closed and opened until no pressure drop occurred in the tank with the valve closed. Once the pressure in the closed tank was constant (after *ca.* 12 h) the solution was considered to be in equilibrium with CO_2 and ready to be injected. The CO_2-equilibrated input solution was injected from bottom to top through the crushed sample by a dual-piston pump under a constant flow rate of 0.058 ± 0.005 mL/min (Fig. 2.3b). Darcy velocity ranged from 1.14×10^{-6} to 1.31×10^{-6} $m^3/m^2/s$, yielding residence times (τ) between 5.5 and 6.7 h (Table 3.1). pH of the solution and fluid pressure were measured in line before the solution reached the column and after the reaction cell. pH was measured using Hamilton Polilyte Plus XP 120 pH electrodes (accuracy ± 0.02), which allow measurements under conditions up to 60 °C and 50 bar. The electrodes were calibrated using Crison buffer solutions of pH 2.02 and 7.00. Fluid pressure was measured using Gasli pressure transducers with a pressure range from -1 to 24 bar and an accuracy of 0.5% over the full scale.

The reacted solution was collected using two pressurized syringes of 250 mL, which worked as back-pressure system maintaining the whole setup under a total pressure of 10 bar. After filling one syringe, the solution was manually diverted to the other one. This sampling system allowed the collection of the output solution without any experimental interruption.

Collected output solutions were extracted from the syringe and immediately acidified with 1% HNO_3 to avoid any precipitation during sample depressurization. The whole sampling operation lasted less than 2 min. Total concentrations were analyzed using ICP-AES (see *Section 2.1.2*). Column experiments were performed at 22-25 °C, 40 ± 0.1 °C and 60 ± 0.1 °C. The storage tank and the column were adequately heated using a resistor and insulated for the experiments performed at 40 and 60 °C.

2.1.3.3 Supercritical pressure setup (*P* = 150 bar)

Two flow-through apparatus (Icare Lab CSS I, Luquot and Gouze, 2009, and Icare Lab CSS II, Luquot et al., 2012), which belong to the Geosciences Department of Montpellier University (France), were used to reproduce the *in situ* reservoir conditions for CO_2 sequestration (Fig. 2.3c). In both experimental devices the CO_2-equilibrated solution was injected into the percolation cell by a monitorized piston-pump system. This system was equipped with displacement encoders to obtain an accurate control of the flow rate, ranging from 0.6 to 180 mL/h in Icare Lab CSS I and from 0.05 to 40 mL/h in Icare Lab CSS II. Radial confining pressure was applied to the silicon jacket that covered the sample in the percolation cell (112% of the inlet pressure). The piston pump motion and the pneumatically-controlled valves were operated by LabView-based software.

A single column experiment in *Part II: crushed rock* was performed using the Icare Lab CSS I, with a flow rate of 0.01 mL/min and P = 150 bar and T = 60 ºC (*Third set* in Table 3.1). The CO_2 partial pressure of the inlet solution was set to be 34 bar (0.38 mol/L of CO_2). Approximately 1 g of ground sample (grain size of 250-500 μm) was placed in a Teflon cell of 0.7 cm in inner diameter (d) and 1.7 cm length (L) (Fig. 2.3c; effective column volume V_{bulk} = 0.69 cm^3). Initial porosity was calculated to be around 55%. A 0.45 μm stainless steel filter was placed at the outlet (bottom) of the Teflon cell to prevent particle escape into the output solution. Given the mineral mass, the rock density and the effective column volume, and assuming that the rock fragments were spheres of 0.375 μm in diameter, the geometric surface area of the vuggy limestone fragments was 7237 m^2_m/m^3_{bulk}. Test tubes of 10 mL were used to collect 0.5 mL of the output solution, which was acidified with 9.5 mL of 1% HNO_3 solution to avoid precipitation of carbonates during sample depressurization. Total concentrations were analyzed by ICP-AES (see *Section 2.1.2*). Darcy velocity was 4.33 $\times$ 10^{-6} $m^3/m^2/s$, yielding a residence time (τ) of 0.6 h (Table 3.1).

All percolation experiments with fractured cores shown in *Part III: fractured cores* were run using both experimental apparatus (Icare Lab CSS I and Icare Lab CSS II). The CO_2 partial pressure of the inlet solution was set to be approximately 62 bar (0.61 mol/L of CO_2) and obtained by mixing the solutions with industrial-grade pure CO_2. CO_2-rich solutions were injected under a constant volumetric flow rate corresponding to Q = 60 mL/h for five experiments using Icare Lab CSS I and Q = 0.2, 1 and 5 mL/h for ten experiments using Icare Lab CSS II (Table 4.1). The pressure difference ΔP(t) between the inlet and the outlet of the sample was recorded continuously. Periodically, 0.5 mL of the output solution were collected in 10 mL test tubes that contained 9.5 mL of 1% HNO_3 solution. The acid was used to prevent any carbonate precipitation due to sample depressurization. Total concentrations were analyzed by ICP-AES (see *Section 2.1.2*). The geometric areas of the minerals that form the sandstone rock (m^2_m/m^3_{bulk}; m: mineral, bulk: core), calculated as explained above, were 7.5×10^5 m^2_m/m^3_{bulk} (for calcite), 3605 m^2_m/m^3_{bulk} (for quartz) and 2180 m^2_m/m^3_{bulk} (for microcline). The grain radii of quartz and microcline were measured from SEM images (225 μm and 90 μm, respectively). Since calcite matrix in both the sandstone and limestone rocks was assumed to be formed of small aggregates with a radius of 2.5 μm, the geometric area of calcite in the limestone rock was 1.03×10^6 m^2_m/m^3_{bulk}.

2.1.4 Mass transfer calculations

The volume of dissolved rock at the end of the experiment was calculated from

$$V_{rock-diss}(t_f) = \sum_1^N V_{m-diss}(t_f) \quad (2.1)$$

where N is the number of minerals that compose the rock, t_f is the total experimental time and V_{m-diss} is the volume of dissolved mineral which, as in case of the volume of precipitated mineral (V_{m-ppt}), was calculated as

$$V_{m-diss/ppt}(t_f) = \upsilon_m Q \int_{t'=0}^{t'=t_f} \alpha^{-1} C_{j-diss/ppt}(t') dt' \quad (2.2)$$

where υ_m is the molar volume of the mineral m (m^3/mol), Q is the flow rate (m^3/s), α is the stoichiometric coefficient of element j in the mineral, C_j is the concentration of the element j from dissolved or precipitated mineral (C_{j-diss} or C_{j-ppt}; mol/m^3) and t' is the sampling time.

Considering that dissolution of calcite and dolomite and precipitation of gypsum were the reactions in the experiments, C_{j-diss} and C_{j-ppt} were calculated from the mass balance equations as:

$$C_{Ca-diss} = C_{Ca(out)} - C_{Ca(in)} + C_{S-ppt} \quad (2.3)$$

$$C_{Mg-diss} = C_{Mg(out)} - C_{Mg(in)} \quad (2.4)$$

$$C_{S-ppt} = C_{S(in)} - C_{S(out)} \quad (2.5)$$

where $C_{j(in)}$ and $C_{j(out)}$ are the input and output concentration of an element *j*, respectively. These concentrations were obtained from the ICP-AES measurements with an error estimated to be around 2%. The error $\varepsilon(\Delta C_j)$ in the change of concentration of element j ($\Delta C_j = C_{j(out)} - C_{j(in)}$) was estimated using the Gaussian error propagation method (Barrante, 1974). The molar volumes of calcite, dolomite and gypsum were calculated from the molecular weights and densities of these minerals (Downs, 2006) yielding 36.93×10^{-6}, 64.93×10^{-6} and 74.86×10^{-6} m^3/mol, respectively.

As for vuggy limestone dissolution, the volume of dissolved rock was calculated considering that calcite and dolomite were the dissolving minerals so that the $C_{Ca-diss}$ term included the amount of Ca release from both reactions. In the case of sandstone dissolution, the volume of dissolved rock was calculated considering that calcite is the only dissolving mineral due to the negligible Si release obtained in the experimental results. Using the calculated structural formula of dolomite ($Ca_{1.048}Mg_{0.952}(CO_3)_2$), the volume of dolostone dissolved was calculated on the basis of both Ca and Mg.

Loss of sample mass was first calculated (ΔM_{calc}) based on the dissolved and precipitated mineral volumes and then measured (ΔM_{meas}) by weighting the samples before and after the experiment.

Porosities after reaction $\phi_{(t_f)}$ in the column experiments presented in *Part II: crushed rock* were calculated on the basis of changes in solution chemistry according to Eq. (2.6):

$$\phi_{(t_f)} = \frac{V_{bulk} - \left(V_{s(t_0)} - V_{rock-diss(t_f)} + V_{m-ppt(t_f)}\right)}{V_{bulk}} \quad (2.6)$$

where V_{bulk} is the effective column volume, $V_{s(t_0)}$ is the initial solid sample volume and $V_{rock-diss(t_f)}$ and $V_{m-ppt(t_f)}$ are the volumes of dissolved rock and precipitated mineral at the end of the experiment, respectively (Eqs. 2.1 and 2.2).

In the percolation experiments with fractured cores shown in *Part III: fractured cores* the change in fracture volume at the end of the experimental time $\Delta V_{ch}(t_f)$ (ch: chemical) was calculated from aqueous chemistry using Eq. (2.7) and compared with the variation in fracture volume obtained from XCMT ($\Delta V_{Xr}(t_f)$).

$$\Delta V_{ch}(t_f) = V_{m-diss}(t_f) - V_{m-ppt}(t_f) \quad (2.7)$$

2.1.5 Permeability changes

Pressure difference between the inlet and the outlet of the fractured sample was measured in the percolation experiments shown in *Part III: fractured cores*. Change in fracture permeability over time k(t) was calculated from the pressure difference ΔP(t) measured between the inlet and the outlet of the sample and combining Darcy's law (Eq. 2.8) with a cubic law for flow through two parallel plates (Eq. 2.9); Huitt, 1956; Witherspoon et al., 1980)

$$k = \frac{\mu L Q}{S \Delta P} \quad (2.8)$$

$$Q = \frac{a_h^3 \Delta P d}{12 \mu L} \quad (2.9)$$

where μ is the dynamic viscosity of the solution (Pa·s), L is the length of the sample in the flow direction (m), Q is the volumetric flow rate (m^3/s), S is the sample cross section (m^2), ΔP is the measured pressure difference (Pa), a_h is the hydraulic aperture of the fracture (m), and d is the width of the fracture (m).

Combining Eqs. (2.8) and (2.9), the hydraulic aperture of the fracture was determined from

$$a_h(t) = \sqrt[3]{\frac{12 \mu L Q}{\Delta P(t) d}} \quad (2.10)$$

and fracture permeability from

$$k(t) = \frac{a_h^2(t)}{12} \quad (2.11)$$

ΔP between the inlet and the outlet of the fractured sample was measured from the beginning of the experiment (t_0) up to a particular point of time t_k. Due to the increase in permeability, ΔP becomes smaller over time. t_k is the time after which the value of ΔP is no longer measureable (below detection). The highest and lowest measurable ΔP values (ΔP_{max} and ΔP_{min}) were 25 and 0.06 bar in Icare Lab CSS I and 25 and 0.33 bar in Icare Lab CSS II. t_k was always ≤ 2 h.

2.2 Reactive transport modeling

1D simulations of the column experiments (*Part II: crushed rock*) and 2D simulations of the percolation experiments with fractured cores (*Part III: fractured cores*) were performed using CrunchFlow (Steefel, 2009; Steefel et al., 2014). The column experiment under CO_2 supercritical conditions (P = 150 bar, T = 60 ºC) was also modeled using PhreeqC (v.3) (Parkhurst and Appelo, 2013). Hence, the results obtained considering the P effect on equilibrium constants (from PhreeqC (v.3)) could be compared with the results that did not include this consideration (from CrunchFlow). *Section A.1.2 (Appendix A)* shows the PhreeqC input file.

2.2.1 Description of the CrunchFlow reactive transport code

The CrunchFlow code solves numerically the mass balance of solutes expressed as

$$\frac{\partial(\phi C_j)}{\partial t} = \nabla \cdot \left(D \nabla C_j\right) - \nabla\left(q C_j\right) + R_j \qquad (j = 1, 2, \ldots, n) \qquad (2.12)$$

where ϕ is porosity, C_j is the concentration of component j (mol/m^3), D is the combined dispersion-diffusion coefficient (m^2/s), q is the Darcian fluid flux (m^3/m^2/s) and R_j is the total reaction rate affecting component j (mol/m$^3_{bulk}$/s).

The total reaction rate for the component j, R_j is given by

$$R_j = -\sum_m \nu_{jm} R_m \qquad (2.13)$$

where R_m is the rate of precipitation ($R_m > 0$) or dissolution ($R_m < 0$) of mineral m in mol/m$^3_{bulk}$/s, and ν_{jm} is the number of moles of j per mol of mineral m.

Since mineral reactions are described using kinetic rate laws, initial reactive surface areas, initial mineral volume fractions and several reaction rate parameters have to be

supplied by the user as input. In this set of simulations, the reaction rate laws used in the calculations are expressed as

$$R_m = -A_m \sum_{terms} k_{r(m,T)} a_{H^+}^{n_{H^+}} \left(\prod_i a_i^{n_i}\right) f_m(\Delta G) \quad (2.14)$$

where R_m is the reaction rate for a given mineral in units of mol/m^3_{bulk}/s, A_m is the mineral surface area (m^2_m/m^3_{bulk}), k_r is the reaction rate constant (mol/m^2/s) at the temperature of interest, $a_{H^+}^{n_{H^+}}$ is the term describing the effect of pH on the rate, $a_i^{n_i}$ is a term describing a catalytic/inhibitory effect by another species on the rate, and $f_m(\Delta G)$ is the function describing the dependence of the rate on the solution saturation state. The summation term indicates that several parallel rate laws may be used to describe the dependence of the rate on pH or on other species.

The rate constant at temperature *T* (K) is calculated from

$$k_{r(m,T)} = k_{r(m,25)}\, exp\left(\frac{E_{app}}{R}\left(\frac{1}{T_{25}} - \frac{1}{T}\right)\right) \quad (2.15)$$

where $k_{r(m,25)}$ is the rate constant of a mineral m at 25 °C, E_{app} is the apparent activation energy of the overall reaction (J/mol), T is temperature in Kelvin and R is the gas constant (J/mol/K).

The $f_m(\Delta G)$ function is defined as

$$f_m(\Delta G) = \left(1 - \left(\frac{IAP}{K}\right)^{m_2}\right)^{m_1} \quad (2.16)$$

where ΔG is the Gibbs energy of the reaction (J/mol), IAP is the ionic activity product of the solution with respect to the mineral, K is the equilibrium constant for that mineral reaction (ionic activity product at equilibrium) and m_1 and m_2 are empirical coefficients.

Changes in mineral surface area A_m (m^2_m/m^3_{bulk}) due to reaction are calculated according to

$$A_m = A_{m,0}\left(\frac{\phi}{\phi_0}\right)^{2/3}\left(\frac{\phi_m}{\phi_{m,0}}\right)^{2/3} \text{dissolution} \quad (2.17)$$

$$A_m = A_{m,0}\left(\frac{\phi}{\phi_0}\right)^{2/3} \text{precipitation} \quad (2.18)$$

where $\phi_{m,0}$ is the initial volume fraction of the mineral m and ϕ_0 is the initial porosity of the medium. This formulation ensures that as the volume fraction of a mineral goes to 0, its surface area does too. Moreover, for both dissolving and precipitating minerals, the term $(\phi\ /\ \phi_0)^{2/3}$ requires that the surface area of a mineral in contact with fluid goes to 0 when the porosity of the medium goes to 0. This formulation is used primarily for primary minerals (*i.e.*, minerals with initial volume fractions > 0). For secondary minerals which precipitate, the value of the initial bulk surface area specified is used as long as precipitation occurs. If this phase later dissolves, the above formulation is used with an arbitrary initial volume fraction of 0.01.

Regardless the changes in permeability in the 2D calculations where flow was updated, the code solved Darcy's law (neglecting the buoyancy term; Eq. (2.19)), and permeability was updated at each time step according to Eq. (2.20).

$$q = -\frac{k}{\mu}\nabla P \tag{2.19}$$

$$k = k_0\left(\frac{\phi}{\phi_0}\right)^3 \tag{2.20}$$

2.2.2 One-dimensional model (*Part II: crushed rock*)

Results and discussion of the 1D reactive transport simulations that reproduce the experimental data of the column experiments are shown in *Chapter 3*. Model parameters used in 1D simulations are given in the following sections.

2.2.2.1 Numerical discretization

The one-dimensional numerical domain is composed of 20 elements in most simulations. Two simulations under atmospheric conditions with *a2.1* input solution (Table 3.1; experiments *L25-atm-a2.1* and *L60-atm-a2.1*) were run using a two-zone domain composed of 40 shorter elements at the start of the column and 16 longer elements along the rest for better resolution of changes in solution composition. See Tables A.1 and A.2 (*Appendix A*) for details of the spatial discretization.

2.2.2.2 Rock and solution composition

Two rocks were considered in the calculations: vuggy limestone and dolostone (Table 2.1). Mineral volume fractions are shown in Tables A.1 and A.2 (*Appendix A*). For each experiment, only the precipitated sulfate phase was taken into account (gypsum at all temperatures).

Rate laws for the reacting minerals were taken from the literature (Palandri and Kharaka, 2004). The fit of the model to the experimental data (aqueous Ca, S, Mg concentrations and pH) was performed by adjusting the values of the reactive surface areas (A_m in Eq. 2.14). A sensitivity study of the reactive surface areas was performed. As a result, ranges of values that could also fit the experimental concentrations within the ± 2% analytical error and experimental pH are provided. In the experiments where gypsum precipitated, the initial surface area of gypsum (area used to fit the early evolution of the system) was increased in separate calculations to fit S and Ca concentrations along the experiment (see initial and final values of the reactive area of gypsum in Tables 2.3 and 2.4).

Calculated (CrunchFlow) saturation index, ionic strength and pH of the injected solutions (input boundary condition) are given in Tables 2.3 and 2.4. In the case of the 34 bar pCO_2 experiment, the PhreeqC (v.3) calculated undersaturations with respect to calcite and gypsum are slightly larger (Table 2.4; SI_{Cal} = -3.25 and SI_{Gp} = -0.07) than the CrunchFlow values owing to the *P* effect on equilibrium constants. In all simulations, the initial solution composition inside the column was considered to be in equilibrium with calcite, dolomite and gypsum.

2.2.2.3 Flow and transport properties

The Darcy velocity q ($m^3/m^2/s$) in the column experiments was obtained dividing the flow rate Q (m^3/s) by the cross section S (m^2) calculated as $S = \pi \cdot r^2$, being r the radius of the column. Darcy velocity q, effective diffusion coefficient D_e and longitudinal dispersivity α_L used in the simulations are shown in Tables A.1 and A.2 (*Appendix A*). The effective diffusion coefficient was derived from

$$D_e = \phi^n D_0 \qquad (2.21)$$

The diffusion coefficient in water at 25 ºC D_0 and the cementation exponent n used in the simulations were 10^{-9} m^2/s and 2-2.5, respectively. They are based on common values

reported in the literature (*e.g.*, Ullman and Aller, 1982; De Marsily, 1986; Domenico and Schwarthz, 1990).

2.2.2.4 Thermodynamic and kinetic data

Thirty-seven aqueous species were considered in most simulations (experiments with *a2.1*, *a3.5*, *gp-u* and *gp-e* as input solution). Two experiments performed under atmospheric conditions used H_2SO_4 input solution in equilibrium with gypsum (*s*). In these cases, seventeen aqueous species were taken into account (Table A.3, *Appendix A*, species with *). All the equilibrium constants (log K at 25, 40 and 60 °C) and stoichiometric coefficients, which were taken from the EQ3/6 database (Wolery et al., 1990; included in the CrunchFlow code), are shown in Table A.3 (*Appendix A*). Activity coefficients were calculated using the extended Debye-Hückel formulation (b-dot model) with parameters obtained from the CrunchFlow database (EQ3/6). Three solid phases were considered in the calculations (calcite, disordered dolomite and gypsum). The equilibrium constants for the mineral reactions were also taken from the EQ3/6 database (Table A.4, *Appendix A*). At 25, 40 and 60 °C, the values of the gypsum equilibrium constants were decreased by approximately 25% to fit the experimentally observed equilibrium condition, as explained in *Section 2.1.2.*

Table 2.3 *Reactive surface area (A_m) and input boundary conditions (SI, I and pH) used in simulations under atmospheric conditions (CrunchFlow code).*

Exp. label	***D25-atm-s***	***L25-atm-s***		***L25-atm-a3.5***	***L60-atm-a3.5***	***L25-atm-a2.1***		***L60-atm-a2.1***	
ROCK COMPOSITION									
A_m (m^2_m/m^3_{bulk})									
Cal	-	120(80 - 180)							
Dol -dis	17(16 - 20)	5(4 - 7)		5(0 - 20)					
		initial	final			initial	final	initial	final
Gp-25	0.03(0.01-0.06)	0.001(0-0.01)	0.015(0.01-0.03)	0(0-0.03)	-	0.01(0-0.1)	0.1(0.02-0.2)	-	-
Gp-40	-	-	-	-	-	-	-	-	-
Gp-60	-	-	-	-	0(0-0.005)	-	-	0.01(0.015-0.03)	0.04(0.02-0.05)
INPUT BOUNDARY CONDITIONS									
Input label	***s***			***a3.5***		***a2.1***			
SI, I and pH (CrunchFlow)									
Cal	-10.33	-10.34		-8.01	-7.77	-10.84		-10.60	
Dol-dis	-22.85	-23.53		-16.55	-15.74	-22.18		-21.36	
Gp-25	0.09	0.08		0.05	-	-0.03		-	
Gp-40	-	-		-	-	-		-	
Gp-60	-	-		-	0.04	-		-0.09	
I	0.05			0.63	0.62	0.61		0.59	
pH	2.50			3.50		2.10			

A_m = Reaction surface area. A_m in brackets indicates the range of values that fits the experimental concentration data (within ± 2% uncertainty) in the sensibility study.
Cal = calcite; Dol-dis = disordered dolomite; Gp = gypsum.

2.2.2.5 Reaction rates

Kinetic rate laws used for primary minerals (calcite and dolomite) and secondary minerals (gypsum) are from Palandri and Kharaka (2004) and Xu et al. (2012). Xu et al. (2012) proposed a calcite dissolution rate that improves the rate-ΔG dependence under close-to-equilibrium conditions ($-12 \leq \Delta G \leq 1.7$ kJ/mol) with respect to the simplest TST-based rate law ($m_1 = m_2 = 1$ in Eq. (2.16)). Hence, all simulations were run based on this rate law (*i.e.*, $m_1 = 3$ and $m_2 = 1$ in Eq. (2.16)). Rate parameters and apparent activation energies are listed in Table A.5 (*Appendix A*). The two parallel rate laws for each primary mineral describe the explicit dependence of the rates on pH. Rate constants at temperatures different from 25 ºC were calculated according to Eq. (2.15).

Table 2.4 *Reactive surface area (A_m) and input boundary conditions (SI, I and pH) used in simulations under subcritical and supercritical conditions (CrunchFlow and PhreeqC (v.3) codes).*

Exp. label	***L25-10-gp-u***	***L40-10-gp-u***	***L25-10-gp-e***		***L40-10-gp-e***		***L60-10-gp-e***		***D40-10-gp-e***	***L60-34-gp-e***
ROCK COMPOSITION										
A_m (m^2_m/m^3_{bulk})										
Cal	120(80 - 180)								-	120(80 - 180)
Dol -dis	5(0 - 10)								5(3 - 20)	10(5 - 30)
			initial	final	initial	final	initial	final		
Gp-25	-	-	0.01(0-0.1)	10(1-*)	-	-	-	-	-	-
Gp-40	-	-	-	-	0.01(0-0.04)	0.3(0.1-*)	-	-	0.3(0.08-*)	-
Gp-60	-	-	-	-	-	-	0.01(0-0.1)	0.1(0.01-*)	-	0.5(0.2 -*)
INPUT BOUNDARY CONDITIONS										
Input label	***gp-u***		***gp-e***							
SI, I and pH (CrunchFlow)										
Cal	-3.45	-3.22	-3.48		-3.21		-2.88		-3.19	-2.96 (-3.25)
Dol-dis	-7.34	-6.71	-7.47		-6.77		-5.96		-6.74	-6.07
Gp-25	-0.19	-	0.00		-		-		-	-
Gp-40	-	-0.20	-		-0.01		-		0.01	-
Gp-60	-	-	-		-		-0.03		-	-0.04 (-0.07)
I	0.60	0.61	0.61		0.62		0.58		0.63	0.60
pH	3.65**	3.7**	3.61**		3.68**		3.78**		3.68**	3.53 (3.40)

A_m = Reaction surface area. A_m in brackets indicates the range of values that fits the experimental concentration data (within ± 2% uncertainty) in the sensibility study.
* Maximum value is not constrained within the experimental error; solution reached equilibrium in the column.
** CrunchFlow (charge balance) calculated pH, similar to the measured averaged pH (see Table 3.1).
Cal = calcite; Dol-dis = disordered dolomite; Gp = gypsum.
SI and pH in brackets is calculated using PhreeqC (v.3).

2.2.3 Two-dimensional model (*Part III: fractured cores*)

Two-dimensional reactive transport simulations were performed to reproduce the experimental data of three percolation experiments with fractured cores which developed

three different dissolution patterns: face dissolution (*L0.2-gp-e*), wormhole (*L1-gp-e*) and uniform dissolution (*S60-no-s*). Results and discussion of the simulations are shown in *Chapter 5*. Model parameters used in 2D simulations are given in the following sections.

2.2.3.1 Numerical discretization

Rectangular coordinates were used to model experiments which developed face and uniform dissolution patterns (*L0.2-gp-e* and *S60-no-s*), whereas rectangular and cylindrical coordinates were used in the experiment where a wormhole developed (*L1-gp-e*). Reasons to apply this modeling approach are given in *Chapter 5*. To simplify the models with rectangular coordinates only half of the core was considered given the symmetry of the fractured cores (Fig. 2.4a).

- Rectangular coordinates: The dimensions of the domain were:

R_y: 20 mm (core length).

R_x: 3.5 mm.

where R_x was computed by considering that half the core section S ($S = \pi(d/2)^2$; d = 9 mm) was equivalent to the area of a rectangle whose sides were d and R_x (Fig. 2.4a).

The domain was composed of two parts: (1) high-permeability zone (fracture, large porosity; in red in Fig. 2.4a) and (2) rock matrix (small porosity; in green in Fig. 2.4a). The fracture zone was at the left side of the rectangular domain, parallel to the flow direction (y axis) and had a thickness equal to half the experimental fracture aperture (*i.e.*, the first node along the x direction).

The domain in experiment *L0.2-gp-e* was composed of 27 elements in the x direction and 36 elements in the y direction. In experiment *S60-no-s* the domain was composed of 28 elements in the x direction and 20 elements in the y direction. This coarser discretization was applied to reduce the computational time constraint by the Courant number. The detailed spatial discretization is given in Table A.6 (*Appendix A*).

- Cylindrical coordinates: The dimensions of the domain were:

C_y: 20 mm (core length)

C_x: 4.5 mm (radius of the core)

In this case, the 2D grid had symmetry around the *y* axis (the core sample axis). The length of the interface (*z*) between two cells along *x* was proportional to the radial distance to the core sample axis. In rectangular coordinates, this length was independent of radius.

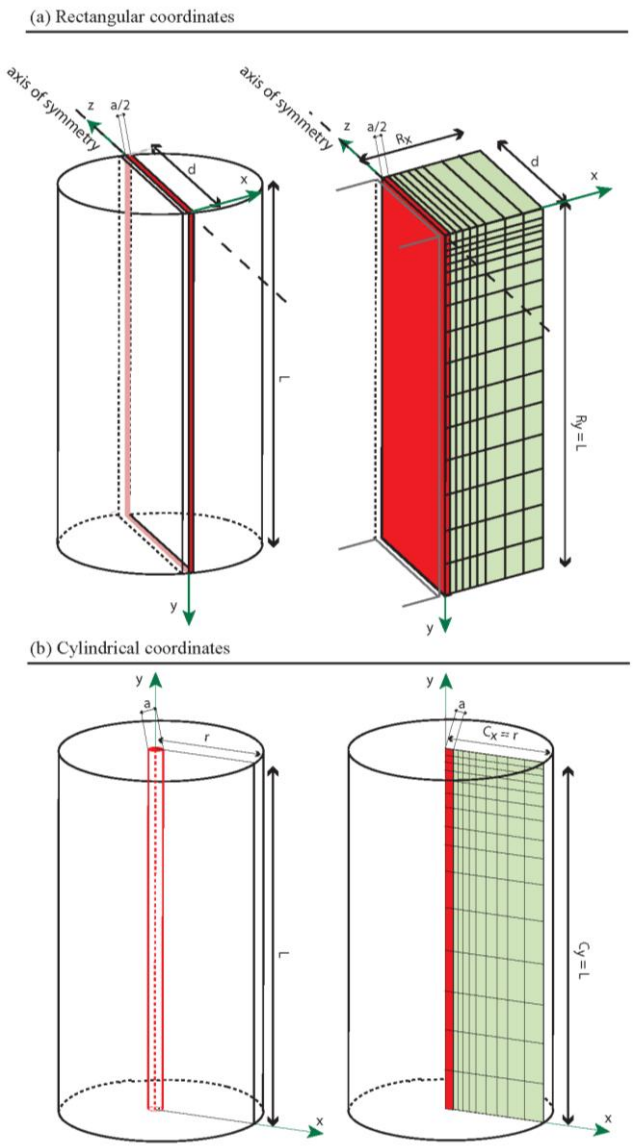

Fig. 2.4 *Scheme showing the geometry and boundary conditions of the flow domain used in the models: (a) rectangular and (b) cylindrical coordinates. Left and right boundaries are no-flow boundaries. Plots on the left show the conceptual model, and plots on the right show the implemented grid.*

The domain was composed of two zones: (1) cylindrical fracture (high porosity) and (2) rock matrix (small porosity). The fracture zone was at the left side of the rectangular domain,

parallel to the flow direction (*y* axis) and 402 μm thick (*i.e.*, 52 nodes along the *x* direction). The thickness of the fracture was varied from 6.7 μm (initial fracture aperture) to 402 μm in a sensitivity study (see *Chapter 5, Section 5.3.2*). When cylindrical coordinates were used, it was assumed that the initial fracture was already cylindrical (*i.e.*, a very small wormhole).

The domain in experiment *L1-gp-e* was composed of 133 elements in the *x* direction and 36 elements in the *y* direction. Elements along the *x* axis were rather short to avoid errors in the flux calculations. The detailed spatial discretization is given in Table A.6 (*Appendix A*).

2.2.3.2 Rock and solution composition

The initial mineralogical composition and porosity of the two described zones are given in Table 2.5. Two rocks were considered in the calculations: oolitic limestone and sandstone (Table 2.1). Fracture porosity was defined to be 100% whereas limestone and sandstone porosities were those reported by CIUDEN (ALM-09-008, 2010).

The reactive surface areas (A_m in Eq. 2.14) of calcite, quartz and microcline were initially calculated considering the geometric area (see *Section 2.1.3.3*). The calcite reactive surface area was fitted to reproduce the variation in Ca concentration. Given that quartz and microcline did not intervene in the overall process, the values of their reactive surface areas were not modified. Calculated values of saturation index, ionic strength and pH of the injected solutions are given in Table 2.2. In all simulations, the initial solution composition in the rock matrix (pore solution) was considered to be in equilibrium with calcite and gypsum.

2.2.3.3 Flow and transport parameters

Flow field was updated according to porosity and permeability changes in the simulations of the experiments that developed face and uniform dissolution (rectangular coordinates). Flow update is not implemented in CrunchFlow when cylindrical coordinates area used, and therefore fixed flow was assumed in this case. Notice that D_e was a fitted parameter in the calculations.

The molecular diffusion coefficient D_0, cementation exponent n (*e.g.*, Ullman and Aller, 1982; De Marsily, 1986; Domenico and Schwarthz, 1990), longitudinal dispersivity α_L and effective diffusion coefficient D_e derived from Eq. (2.21), are listed in Table 2.6.

Table 2.5 *Initial mineralogical composition of both the rock matrix and the high-permeability zone (fracture) and input solution used in the 2D simulations.*

Exp. label	***L0.2-gp-e***		***L1-gp-e***		***S60-no-s***	
Rock matrix						
Rock	Oolitic limestone				Sandstone	
Initial porosity ϕ_0 %	5				6	
	Vol. F.	A_m	Vol. F.	A_m	Vol. F.	A_m
Cal	0.95	2000	0.95	9500	0.612	300000
Qz	-	-	-	-	0.264	3605
Mic	-	-	-	-	0.060	2180
Gp-60	0.00	100	0.00	6	-	-
High-permeability (fracture) zone						
Initial porosity ϕ_0 %	100		100		100	
	Vol. F.	A_m	Vol. F.	A_m	Vol. F.	A_m
Gp-60	0.00	100	0.00	6	-	-
Input solution						
Input label	*gp-e*		*gp-e*		*no-s*	

A_m = Reactive surface area in m^2_m/m^3_{bulk}. Vol. F. = Volume fraction

Chemical composition, calculated pH, SI and I of the input solutions are in Table 2.2.

In the simulation of the wormhole experiment (*i.e.*, rectangular + cylindrical coordinates and fixed flow), q was fixed in the fracture zone of the numerical domain. In simulations of the experiments with face and uniform dissolution patterns (*i.e.*, rectangular coordinates and flow update), Q (m^3/s) was imposed at the first node of the high-permeability zone (node 1,1) to obtain the corresponding q ($m^3/m^2/s$).

In the experiments where flow field was updated, rock and fracture permeability varied according to Eq. (2.20). Initial fracture permeability in experiment *S60-no-s* was obtained by hydraulic measurement using Eqs. (2.10 and 2.11). However, in experiment *L0.2-gp-e*, hydraulic measurement could not be performed and hence initial fracture permeability was calculated using Eq. (2.11) and the fracture aperture measured from SEM image (a_s). In both cases, initial limestone and sandstone permeabilities (rock matrix) were assumed to be 10^{-20} m^2 based on the measured rock permeabilities (see *Section 2.1.1*). In these two simulations, left and right boundaries were no-flow boundaries. Initial pressure was set to 150 bar in the entire domain.

Table 2.6 *Initial transport properties assumed in the 2D calculations.*

Exp. label		***L0.2-gp-e***	***L1-gp-e***	***S60-no-s***
Coordinates		rectangular	rectangular + cylindrical	rectangular
Fracture permeability *k*	m^2	6.75E-12[(1)]	-	4.32E-12[(2)]
Rock permeability *k*	m^2	1.00E-20	-	1.00E-20
Initial Darcy velocity (N) *q*	$m^3/m^2/s$	6.86E-04	4.61E-3 (1) + 5.47E-4 (52)	2.56E-01
Diffusion coeff. D_0	m^2/s	1.1E-10	5.36E-09	1.1E-08
Cementation exponent *n*		2.5	2.5	2.5
Eff. diffusion coeff. D_e	m^2/s	6.0E-14	3.0E-12	9.5E-12
Long. dispersivity α_L	m	0.01	0.01	0.01
Trans. dispersivity α_T	m	-	-	-

N = number of nodes along the *x* direction with fixed flow

[(1)]Fracture permeability calculated using Eq. (2.11) and a_s.

[(2)]Fracture permeability calculated using Eq. (2.11) and a_h.

2.2.3.4 Thermodynamic and kinetic data

Thirty-seven aqueous species were considered in limestone simulations (experiments *L0.2-gp-e* and *L1-gp-e*; Table A.3, *Appendix A*) and forty-four aqueous species in the sandstone simulation (experiment *S60-no-s*; Table A.7, *Appendix A*). Equilibrium constants (log K at 60 °C) and stoichiometric coefficients, which were taken from the EQ3/6 database (Wolery et al., 1990; included in the CrunchFlow code), are shown in Tables A.3 and A.7 (*Appendix A*). Activity coefficients were calculated using the extended Debye-Hückel formulation (b-dot model) with parameters obtained from the CrunchFlow database (EQ3/6).

Two solid phases were considered in the limestone calculations (calcite and gypsum) and three solid phases in the sandstone calculations (calcite, microcline and quartz). The equilibrium constants for the mineral reactions were also taken from the EQ3/6 database (Table A.8, *Appendix A*). The values of the gypsum equilibrium constants at 60 °C were decreased by approximately 25% to fit the experimentally observed equilibrium condition, as explained in *Section 2.1.2.*

2.2.3.5 Reaction rates

Kinetic rate laws used for calcite, quartz and gypsum are from Palandri and Kharaka (2004) and Xu et al. (2012) and those for microcline are from Bandstra et al. (2008). Rate parameters and apparent activation energies are listed in Table A.9 (*Appendix A*). The two parallel rate laws for calcite and microcline describe the explicit dependence of the rates on pH.

Part II:

Crushed Rock

Chapter 3

Interaction between CO_2-rich sulfate solutions and carbonate rocks: column experiments and 1D modeling

3.1 Introduction

This chapter focuses on the understanding of the coupled reactions of calcite/dolomite dissolution and gypsum precipitation by assessing the effect that *P*, pCO_2, *T*, mineralogy, acidity and solution saturation state exert on the reactions. Experiments using columns filled with vuggy limestone or dolostone were conducted under different *P*-pCO_2 (atmospheric: 1-$10^{-3.5}$ bar; subcritical: 10-10 bar; and supercritical: 150-34 bar) and *T* (25, 40 and 60 ºC) conditions. Input solutions were injected varying the sulfate content (gypsum-undersaturated and gypsum-equilibrated solutions) and the acidity source (strong HCl and weak H_2CO_3 acids). In addition, the experimental data were reproduced by means of 1D reactive transport calculations to evaluate mineral reaction rates in the system (fitted in the model through the reactive surface area term) and to quantify the porosity variation. The CrunchFlow (Steefel, 2009) and PhreeqC (v.3, Parkhurst and Appelo, 2013) numerical codes were used to conduct the simulations.

Note: This chapter is based on the article: Garcia-Rios, M., Cama, J., Luquot, L., Soler, J.M., 2014. Interaction between CO_2-rich sulfate solutions and carbonate reservoir rocks from atmospheric to supercritical CO_2 conditions. Chem. Geol. 383, 107-122.

3.2 Results

The experimental conditions and results (output pH, volumes of dissolved rock and precipitated mineral, porosity variation, and measured and calculated loss of mass) of the column experiments are shown in Table 3.1. The output pH was measured *ex-situ* in experiments performed under atmospheric conditions and *in-situ* under subcritical conditions. In the experiment conducted under supercritical conditions output pH could not be measured and was calculated using CrunchFlow and PhreeqC (v.3). The volumes of dissolved limestone and dolostone ($V_{L\text{-}diss}$ and $V_{D\text{-}diss}$) and precipitated gypsum ($V_{Gp\text{-}ppt}$) were calculated according to Eqs. (2.1) and (2.2) based on the Ca, Mg and S input and output concentrations. The resulting porosity was computed from these values using Eq. (2.6). The mass of the sample was weighted before and after reaction in the experiments under subcritical and supercritical conditions. The measured loss of mass (ΔM_{meas}) was compared with the one calculated from mass balance (ΔM_{calc}).

In all the experiments with gypsum-equilibrated solutions, the S concentration of the output solution was smaller than that of the input solution, indicating that a sulfate-rich mineral precipitated. This phase was identified by X-ray diffraction (XRD) to be gypsum in all cases. SEM images showed the typical needle shape of gypsum crystals (Fig. 3.1).

The model fit was achieved by adjusting reactive surface areas, using values much smaller than the calculated geometric surface areas (2000 m^2_m/m^3_{bulk} in the atmospheric and 10 bar pCO_2 experiments and 7237 m^2_m/m^3_{bulk} in the 34 bar pCO_2 experiment). Reactive transport simulations using A_{Cal} = 120 m^2_m/m^3_{bulk} and $A_{Dol} \approx 5$ m^2_m/m^3_{bulk} provided a good fit to the experimental data (Fig. 3.2, 3.3 and 3.4). An explanation for the small values of area could be given by the transport (diffusion) control of the net reactions at pH < 5 (e.g., Sjöberg and Rickard, 1984). When gypsum precipitation occurred in limestone column experiments, the initial value of A_{Gp} used to fit the early stage was increased to fit the temporal variation of the experimental S deficit and Ca excess. The final value of A_{Gp} ranges from 0.015 to 10 m^2_m/m^3_{bulk} (Tables 2.3 and 2.4). By contrast, in dolostone column experiments, a single value of A_{Gp} provided a good fit for the whole duration of the experiments because of the rapid steady-state of the experimental S deficit and Ca excess. A sensitivity analysis regarding surface areas yielded a range of A_{Cal}, A_{Dol} and A_{Gp} values that matched the experimental data within the 2 % of analytical uncertainty (Tables 2.3 and 2.4).

Table 3.1 *Experimental conditions and results (pH, volume of dissolved rock and precipitated mineral, porosity variation, and measured and calculated loss of mass) of the column experiments.*

Experiment label	Sample	Input solution label	T (°C)	Initial mass (g)	V_p (cm^3)	τ (h)	pH input	pH ouput	t_f (h)	Loss of mass (g) ΔM_{meas}	$\Delta M_{calc\text{-}Ca}$	$\Delta M_{calc\text{-}Mg}$	$V_{rock\text{-}diss}$ (Ca) (cm^3)	$V_{rock\text{-}diss}$ (Mg) (cm^3)	$V_{Gp\text{-}ppt}$ (cm^3)	$\Delta\phi$ (Ca)	$\Delta\phi$ (Mg)
First Set	***atmospheric conditions (P = 1 bar; p CO_2 = $10^{-3.5}$ bar)***																
L25-atm-s	L	*s*	25	20.82	6.2	4.6	2.50	7.55	2451	-	1.43	-	0.57	-	0.06	3.72	-
D25-atm-s	D	*s*	25	21.15	6.4	5.0	2.50	7.55	2812	-	0.75	0.90	0.41	0.46	0.18	1.65	2.03
L25-atm-a2.1	L	*a2.1*	25	19.37	6.7	5.6	2.10	7.3	732	-	1.31	-	0.56	-	0.09	3.39	-
L60-atm-a2.1	L	*a2.1*	60	19.42	6.7	5.6	2.10	7.31	732	-	0.88	-	0.52	-	0.23	2.07	-
L25-atm-a3.5	L	*a3.5*	25	19.41	6.7	5.6	3.50	6.75	542	-	0.08	-	0.03	-	-	0.20	-
L60-atm-a3.5	L	*a3.5*	60	19.43	6.7	5.3	3.50	6.82	542	-	0.06	-	0.02	-	-	0.15	-
Second Set	***subcritical conditions (P = p CO_2 = 10 bar)***																
L25-10-gp-u	L	*gp-u*	25	61.60	20.8	5.5	3.56	5.22	204	1.74	1.61	-	0.59	-	-	1.36	-
L40-10-gp-u	L	*gp-u*	40	56.00	22.8	6.1	3.65	5.17	506	-	2.84	-	1.04	-	-	2.40	-
L25-10-gp-e	L	*gp-e*	25	62.61	20.4	6.1	3.51	5.21	721	4.60	3.59	-	1.71	-	0.47	2.87	-
L40-10-gp-e	L	*gp-e*	40	58.27	22	6.7	3.62	5.16	684	2.49	2.61	-	1.22	-	0.30	2.11	-
L60-10-gp-e	L	*gp-e*	60	59.23	21.7	6.6	3.73	5.13	683	1.78	1.90	-	0.81	-	0.13	1.58	-
D40-10-gp-e	D	*gp-e*	40	61.60	21.7	6.2	3.60	4.62	889	1.04	0.82	0.71	0.46	0.42	0.21	0.57	0.48
Third Set	***supercritical conditions (P = 150 bar; p CO_2 = 34 bar)***																
L60-34-gp-e	L	*gp-e*	60	0.852	0.38	0.6	*3.53*	*4.72*	121	0.05	0.07	-	0.03	-	0.004	3.82	-

Labels of the experiments are coded by rock type, T, p CO_2 and input solution label: **rock*T*-*p* CO_2-input label**.

L = limestone; D = dolostone.

V_p = pore volume.

τ = residence time; t_f = experimental time.

Input pH (10 bar p CO_2) and output pH (atmospheric and 10 bar p CO_2) are the averaged measured pH (pH value ± 0.20).

Input and output pH in italics (34 bar p CO_2) indicates CrunchFlow calculated pH (charge balance).

$V_{rock\text{-}diss}$ (Ca) and $V_{rock\text{-}diss}$ (Mg) indicate the volume of dissolved rock, calculated from Ca and Mg release, respectively.

$V_{Gp\text{-}ppt}$ indicates the volume of precipitated mineral.

The propagated error of $V_{rock\text{-}diss}$, $V_{Gp\text{-}ppt}$ and calculated loss of mass is ± 10%.

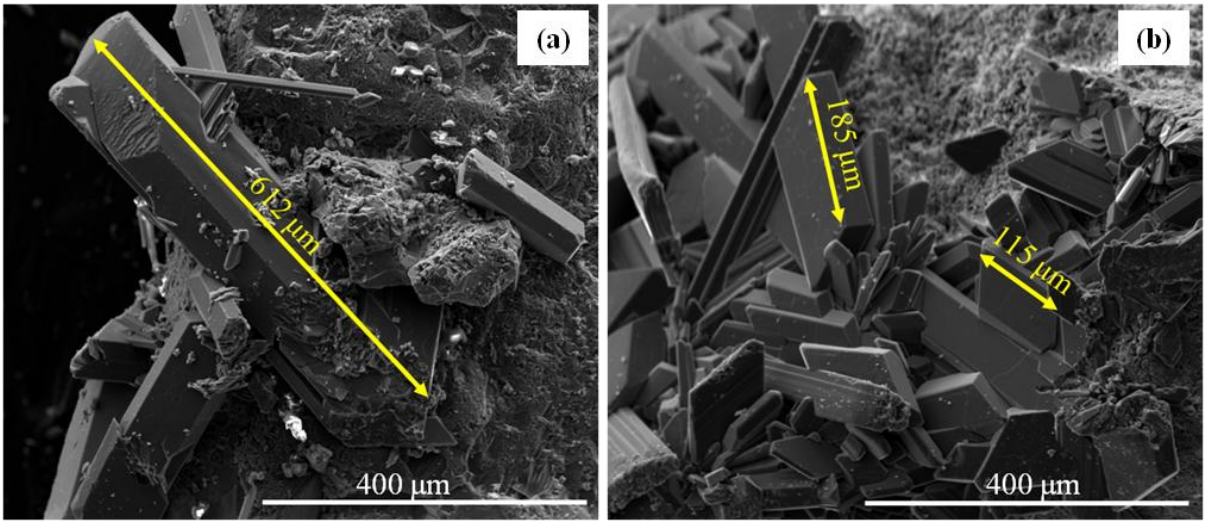

Fig. 3.1 *SEM images of the reacted limestone (a) and dolostone (b). Gypsum needles precipitated on the carbonate surfaces.*

As stated above, simulations successfully reproduced the experimental variation of Ca, Mg and S concentration over time. However, the simulated output pH matched the measured output pH of the 10 bar pCO_2 experiments (Fig. B.3b, *Appendix B*) but was systematically smaller than the measured one in experiments under atmospheric pCO_2 (Fig. B.1a, *Appendix B*). This mismatch was probably caused by CO_2 degassing when measuring the output pH under atmospheric conditions. pH was measured in line under 10 bar pCO_2 (no degassing).

3.2.1 Experiments under atmospheric conditions (P = 1 bar; $pCO_2 = 10^{-3.5}$ bar)

3.2.1.1 H_2SO_4 solution (*s*)

Fig. 3.2a, b shows the output Ca and S concentrations measured during the experiments with *s* input solution (Table 3.1; experiments *L25-atm-s* and *D25-atm-s*). The measured output pH rapidly increased from 2.50 to 7.55 and reached steady state from the start of the experiment in both limestone and dolostone column experiments (Fig. B.1a, *Appendix B*). The output Ca concentration was larger than the input one in both experiments (Fig. 3.2a). The high output pH and Ca and Mg concentrations indicate that calcite and dolomite dissolved.

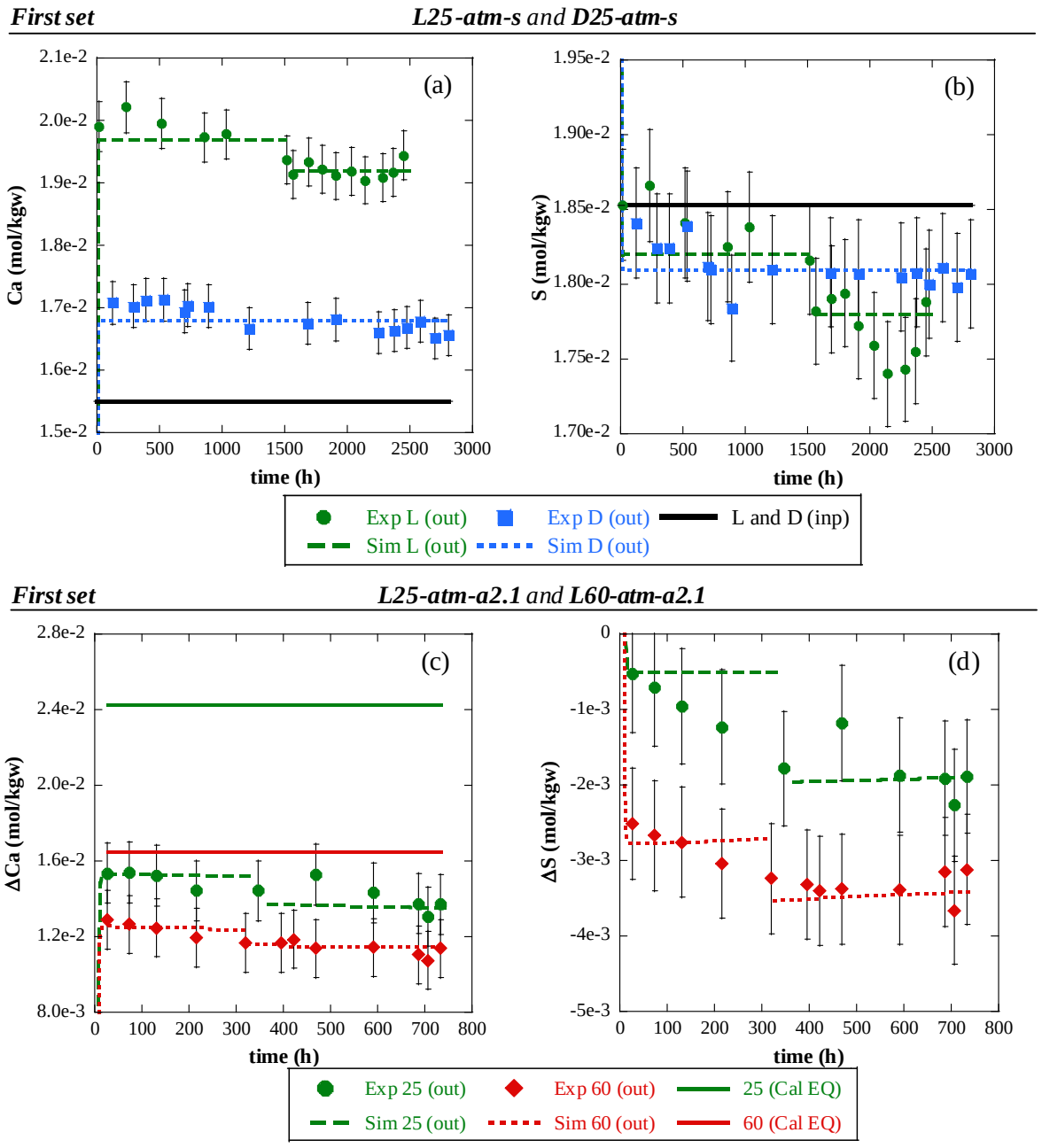

Fig. 3.2 *Top row (experiments L25-atm-s and D25-atm-s): Variation of the experimental (Exp) and simulated (Sim) output concentration of Ca (a) and S (b) with time in limestone (L; in green) and dolostone (D; in blue) column experiments. Black-solid lines indicate input solution. Dashed and dotted lines depict simulated values of limestone and dolostone column experiments, respectively. Bottom row (experiments L25-atm-a2.1 and D25-atm-a2.1): Variation of the experimental (Exp) and simulated (Sim) increase in Ca (c) and S (d) concentration with time in limestone column experiments at 25 ºC (in green) and 60 ºC (in red). Solid lines indicate the Ca concentration increase at equilibrium with calcite.*

During limestone dissolution, output pH and output Ca concentration reached equilibrium with calcite (equilibrium Ca concentration is 1.98×10^{-2} M). However, during

dolostone dissolution output Ca and Mg concentration did not achieve equilibrium with dolomite (equilibrium Ca and Mg concentrations are 1.82×10^{-2} M and 2.88×10^{-3} M, respectively). Equilibrium concentrations were calculated with PhreeqC (v.3; Parkhurst and Appelo, 2013) and the PhreeqC database. In the limestone column experiment, the output S concentration was only slightly smaller than the input one up to around 1500 h, after which it decreased and reached steady state. By contrast, in the dolomite column experiment, the output S concentration was smaller than the input concentration and steady state was reached from the start of the experiment (Fig. 3.2b). This decrease indicates that a sulfate-rich mineral precipitated after around 1500 h in the limestone column experiment and almost from the start in the dolomite column experiment. The precipitated sulfate-rich mineral was identified by XRD to be gypsum in both cases. In the column experiments performed by Singurindy and Berkowitz (2003), clogging of the column due to gypsum precipitation was favored under flow rates between 1 and 2.2 mL/min and H^+/SO_4^{2-} ratios between 2 and 2.5. The range of H^+/SO_4^{2-} ratios and flow rates used in their study were significantly higher than those used in our experiments.

3.2.1.2 Acidic gypsum-equilibrated solution (*a2.1* and *a3.5*)

Two limestone column experiments with *a2.1* input solution were performed at 25 and 60 ºC (Table 3.1; experiments *L25-atm-a2.1* and *L60-atm-a2.1*). Fig. 3.2c and d shows the experimental and simulated Ca and S concentration increase versus time. In these experiments, the measured output Ca concentration and pH were higher than the respective input values. The output Ca concentration was slightly larger at 25 than at 60 ºC. The solution saturation state was close to calcite equilibrium at both temperatures, but closer at 60 ºC (Fig. 3.2c; PhreeqC (v.3)-calculated equilibrium Ca concentrations at 25 and 60 ºC were 7.28×10^{-2} M and 6.45×10^{-2} M, respectively). At both temperatures, S concentration was immediately smaller than the input one, indicating immediate precipitation of sulfate-rich mineral. According to the S deficit, mineral precipitation at 60 ºC was higher than at 25 ºC (Fig. 3.2d).

The precipitated sulfate-rich mineral at 25 and 60 ºC was identified by XRD to be gypsum even if thermodynamically the most stable phase at 60 ºC was considered to be anhydrite. The fact that gypsum was the precipitated phase at 60 ºC was not rare owing to the existence of a marked inconsistency between the thermodynamics of calcium sulfate and its crystallization behavior (Van Driessche et al., 2012). Ossorio et al. (2013) reported that

salinity and temperature strongly influence the type and stability of the precipitated phase (gypsum, bassanite and anhydrite), yielding gypsum stability up to 10 months at 80 ºC under 0.8 M NaCl conditions. Increasing salinity (4.3 M NaCl), bassanite precipitation prevails and gypsum stability decreases.

In the limestone column experiments run with *a3.5* input solution (Table 3.1; experiments *L25-atm-a3.5* and *L60-atm-a3.5*), the output Ca concentration was only slightly larger than the input one (Fig. B.2a, *Appendix B*), and the input and output Mg and S concentrations were the same within error. Therefore, at this input pH, limestone dissolution was small and there was no precipitation. The output pH increased up to 6.75 (25 ºC) and 6.82 (60 ºC) (Fig. B.2b, *Appendix B*).

3.2.2 Experiments under subcritical conditions ($P = pCO_2 = 10$ bar)

3.2.2.1 Gypsum-undersaturated solution (*gp-u*)

In the limestone column experiments with *gp-u* input solution (Table 3.1; experiments *L25-10-gp-u* and *L40-10-gp-u*), the output Ca concentration was larger than the input concentration at both temperatures (25 and 40 ºC), reached steady state at the start of the experiment, and was greater at 25 ºC than at 40 ºC (Fig. B.3a, *Appendix B*). The output pH increased up to 5.22 (25 ºC) and 5.17 (40 ºC) (Fig. B.3b, *Appendix B*). The input and output Mg and S concentrations were the same within error. Therefore, calcite dissolution was the only occurring reaction. In both experiments, the solution saturation state did not reach equilibrium with calcite (Fig. B.3a, *Appendix B*; PhreeqC (v.3)-calculated equilibrium Ca concentrations at 25 and 40 ºC were 7.04×10^{-2} M and 6.31×10^{-2} M, respectively). In the experiment performed at 25 ºC, the measured loss of mass calculated by subtracting the final weight of the sample from the initial weight was 8% higher than the calculated loss of mass based on the aqueous chemistry (comparison of ΔM_{meas} and $\Delta M_{calc\text{-}Ca}$ in Table 3.1). However, these values were within the calculated propagated error (≈ 10%).

3.2.2.2 Gypsum-equilibrated solution (*gp-e*)

Three limestone column experiments with *gp-e* input solution were performed at 25, 40 and 60 ºC (Table 3.1; experiments *L25-10-gp-e*, *L40-10-gp-e* and *L60-10-gp-e*).

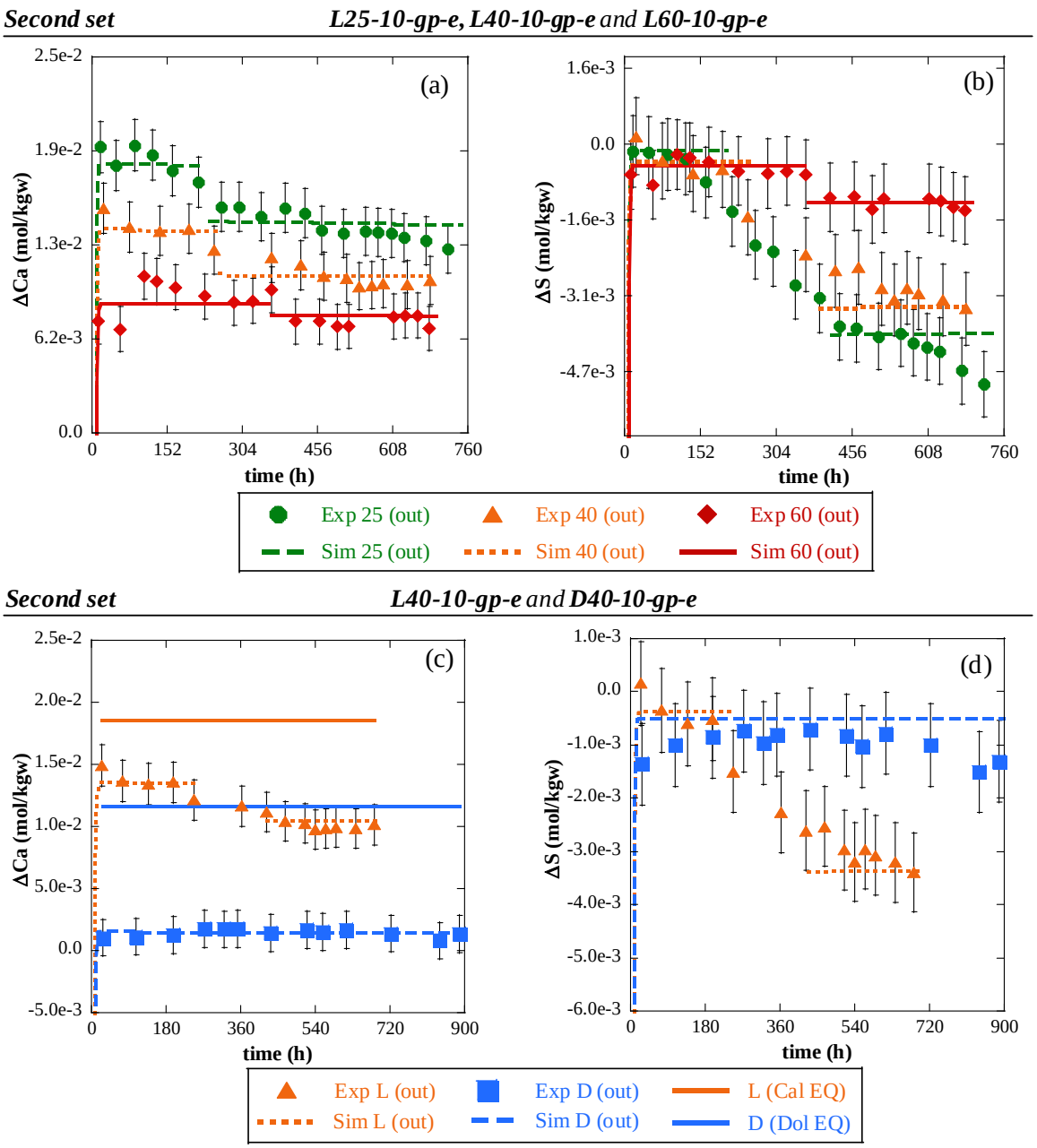

Fig. 3.3 *Top row (experiments L25-10-gp-e, L40-10-gp-e and L60-10-gp-e): Variation of the experimental (Exp) and simulated (Sim) increase in Ca (a) and S (b) concentration with time in limestone column experiments at 25 ºC (in green), 40 ºC (in orange) and 60 ºC (in red). Dashed, dotted and red-solid lines show simulated values at 25, 40 and 60 ºC, respectively. Bottom row (experiments L40-10-gp-e and D40-10-gp-e): Variation of the experimental (Exp) and simulated (Sim) increase in Ca (c) and S (d) concentration versus time in limestone (L; in orange) and dolostone (D; in blue) column experiments. Dotted and dashed lines show simulated values of limestone and dolostone experiments, respectively. Solid lines in (c) represent the Ca concentration increase in equilibrium with calcite (in orange) and dolomite (in blue).*

The results of this set of experiments showed that the output pH immediately increased up to 5.21 (25 ºC), 5.16 (40 ºC) and 5.13 (60 ºC) and reached steady state. The output Ca

concentration exceeded that of the input in all experiments and decreased with time at 25 and 40 ºC, reaching steady state at 60 ºC. Ca release decreased with temperature (Fig. 3.3a; $\Delta Ca_{25ºC} > \Delta Ca_{40ºC} > \Delta Ca_{60ºC}$). In all experiments, the solution saturation state did not reach equilibrium with calcite, being slightly further from equilibrium at 25 ºC (PhreeqC (v.3)-calculated equilibrium Ca concentrations at 25, 40 and 60 ºC were 7.55×10^{-2} M, 6.93×10^{-2} M and 6.08×10^{-2} M, respectively). The input and output Mg concentrations were the same within error. The output S concentration was smaller than the input concentration in all experiments. This S deficit gradually increased with time at 25 and 40 ºC and showed little variation with time at 60 ºC. Output S concentration increased with temperature, which implies that $|\Delta S_{60ºC}| < |\Delta S_{40ºC}| < |\Delta S_{25ºC}|$ (Fig. 3.3b). Thus, according to the resulting trend of ΔCa and ΔS, the amounts of dissolved calcite and precipitated gypsum (identified by XRD) were larger at lower temperatures.

Using *gp-e* as input solution, the dolostone column experiment at 40 ºC (Table 3.1; experiment *D40-10-gp-e*) showed that the output pH increased up to 4.62. ΔCa and ΔS variations with time are shown in Fig. 3.3c and d. The output Ca and Mg concentrations only increased very slightly (zero within error) and immediately reached steady state. The solution saturation state did not reach equilibrium with dolomite. In contrast to the limestone experiment, the output S concentration decreased immediately and reached steady state (Fig. 3.3d). However, the drop in concentration was very small (zero within error).

In this set of experiments, the measured loss of mass was different from the calculated loss of mass by a factor of 5-28% (Table 3.1).

3.2.3 Experiment under supercritical conditions (P = 150 bar; pCO_2 = 34 bar)

The output pH in the limestone column experiment with *gp-e* input solution at 34 bar of pCO_2, P of 150 bar and T of 60 ºC (Table 3.1; experiment *L60-34-gp-e*) could not be measured. The simulated output pH rapidly increased up to 4.72 (CrunchFlow) and 4.47 (PhreeqC (v.3)) and reached steady state. The output Ca and Mg concentrations were larger than the input concentrations (Fig. 3.4a), and the output S concentration was slightly smaller (Fig. 3.4b). Hence, limestone dissolved and gypsum (identified by XRD) precipitated. The calculated loss of mass (0.07 g) was 40% higher than the measured loss of mass (0.05 g) (Table 3.1), the difference being due to the small mass value.

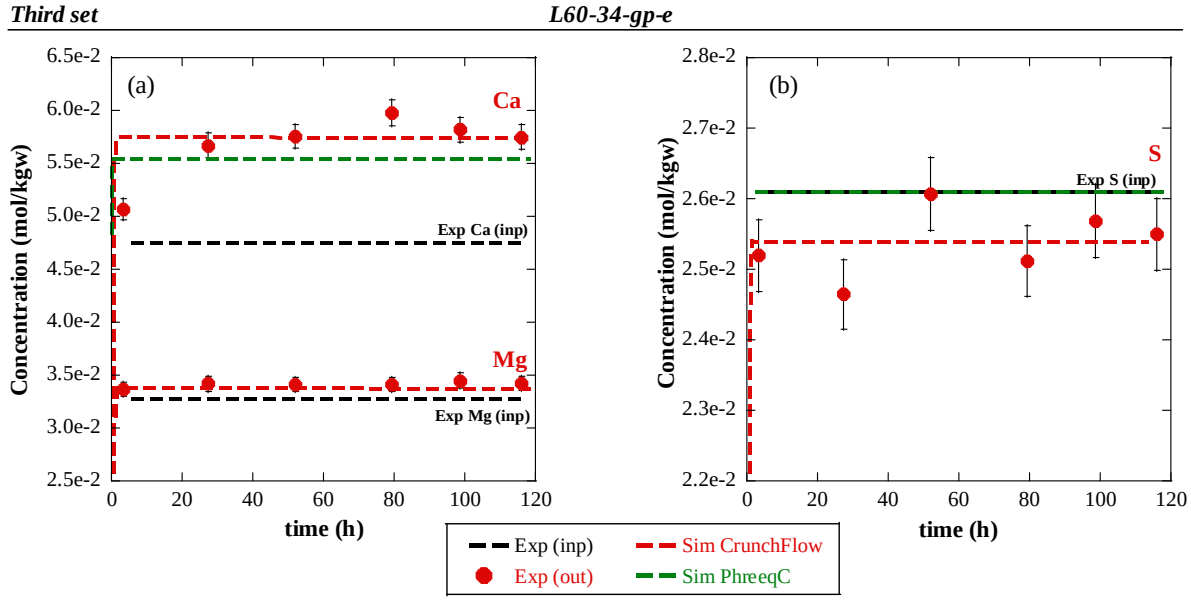

Fig. 3.4 *Variation of the experimental (Exp) and simulated (Sim) output Ca and Mg (a) and S (b) concentration with time in the limestone column experiment under supercritical conditions (L60-34-gp-e). Red and green dashed lines indicate simulated values of output concentrations using CrunchFlow and PhreeqC (v.3), respectively. In the PhreeqC (v.3) calculation, dolomite was not considered and the calculated output S concentration coincides with the input value.*

3.3 Discussion

The influence of the variation in *T*, mineralogy and pCO_2 on the dissolution and precipitation processes was evaluated using the experimental and modeling results. Overall, it was observed that (1) by lowering temperature, the amount of dissolved limestone increased under any pCO_2 condition and gypsum precipitation was only favored at high pCO_2; (2) as expected, the amount of mineral dissolved and porosity increase were noticeably larger in the limestone experiments than in the dolostone ones, regardless of solution composition, temperature and dissolved CO_2; gypsum precipitated immediately as dolostone dissolved and only after some time as limestone dissolved; and (3) by increasing pCO_2 the amounts of dissolved limestone and precipitated gypsum increased, enhancing the porosity over a longer column length.

Moreover, under all *P*-pCO_2-*T* conditions, the volume of precipitated gypsum was always smaller than the volume of dissolved rock (either limestone or dolostone), yielding in all cases a porosity increase. Detailed explanation of the mechanisms that control the occurring processes is given as follows and is illustrated by the plots in Fig. 3.5 and 3.6.

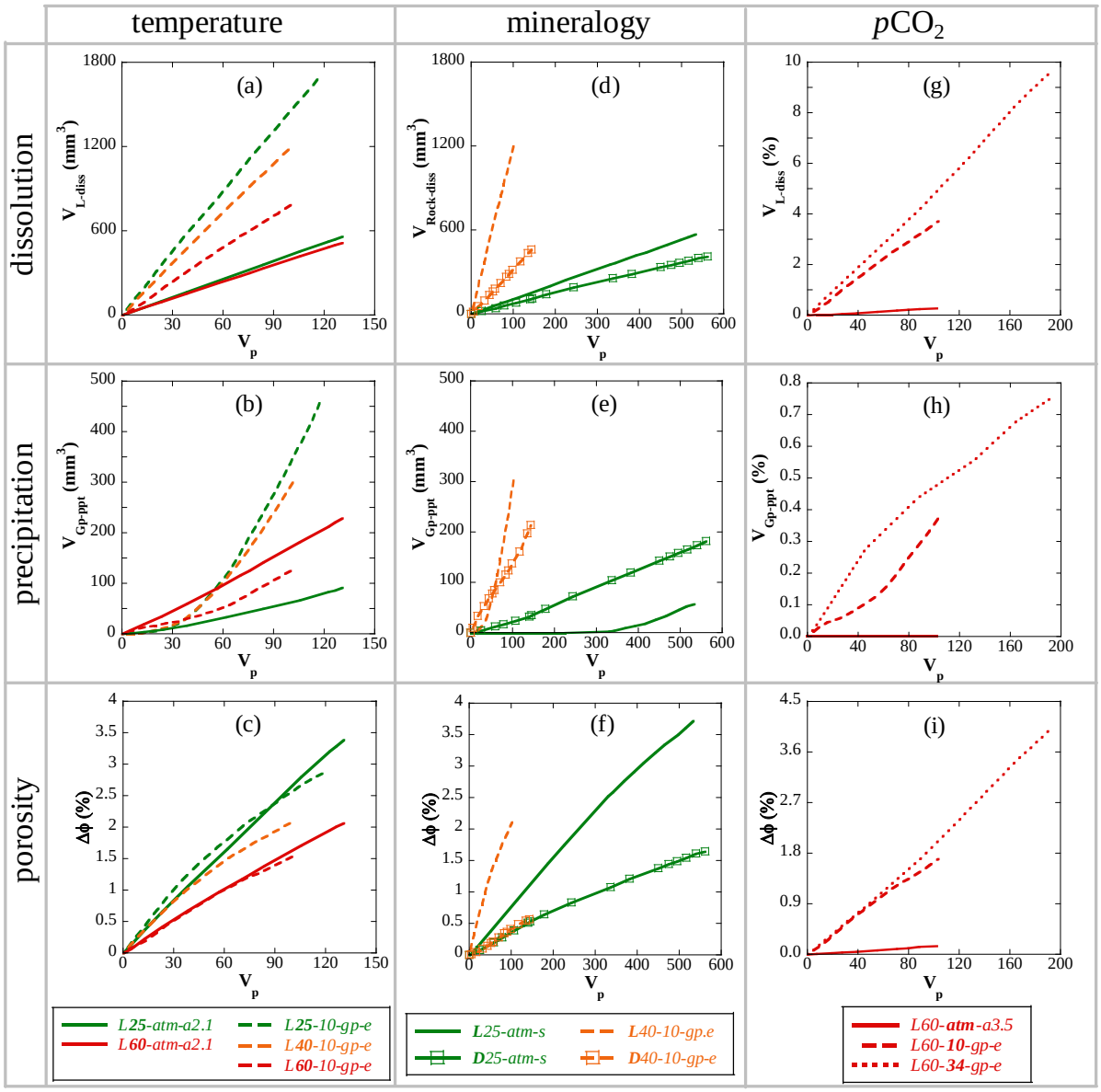

Fig. 3.5 *Experimental variation of volume of dissolved rock $V_{rock\text{-}diss}$ (a and d), percentage of volume of dissolved limestone (g), volume of precipitated gypsum $V_{Gp\text{-}ppt}$ (b and e), percentage of volume of precipitated gypsum (h) and porosity $\Delta\phi$ (c, f and i) with number of pore volumes V_p in experiments performed at 25 ºC (in green), 40 ºC (in orange) and 60 ºC (in red). Solid, dashed and dotted lines (plots of T and pCO_2) represent atmospheric, 10 bar and 34 bar pCO_2 conditions, respectively. Solid lines and solid lines with empty squares (plots of mineralogy) indicate experiments with limestone (L) and dolostone (D), respectively. $V_{L\text{-}diss}$ (%) and $V_{Gp\text{-}ppt}$ (%) are percentages of dissolved and precipitated volumes with respect to each initial sample volume.*

(1) *T* effect: Comparison between two groups of experiments with gypsum-equilibrated solution and temperature ranging from 25 to 60 ºC was used to assess the *T* effect on porosity changes (Table 3.1; the first group was conducted under atmospheric pCO_2 (*L25-atm-a2.1* and *L60-atm-a2.1*) and the second group under 10 bar of pCO_2 (*L25-10-gp-e*, *L40-10-gp-e* and *L60-10-gp-e*)). Fig. 3.5a shows that the amount of limestone dissolved

increased by decreasing the temperature, and that the difference between $V_{L\text{-}diss}$ at 25ºC and $V_{L\text{-}diss}$ at 60ºC considerably increased with pCO_2. Indeed, after 100 pore volumes, $V_{L\text{-}diss}$ (25ºC)/$V_{L\text{-}diss}$ (60ºC) was 1.08 under atmospheric conditions and 1.99 under 10 bar of pCO_2.

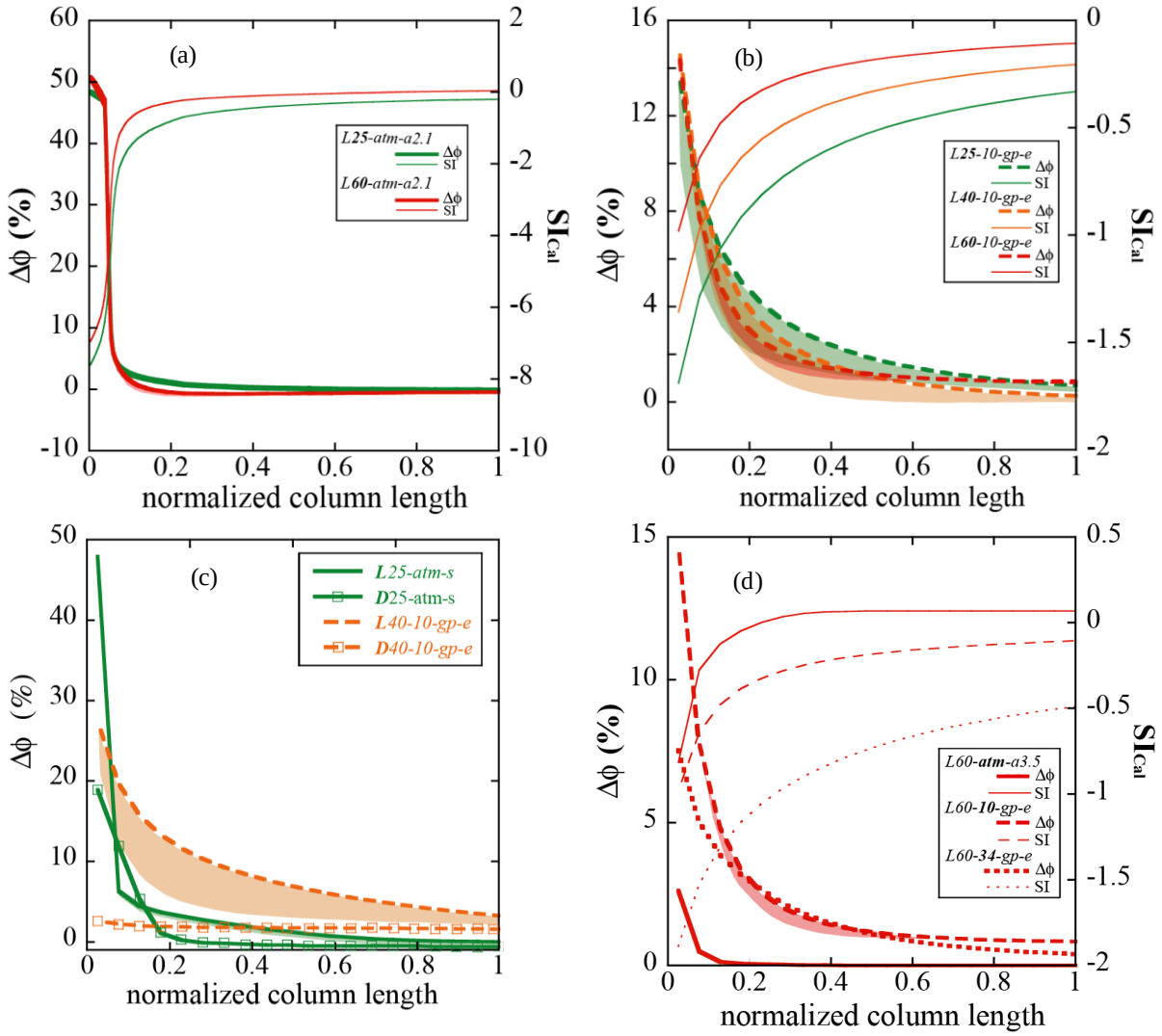

Fig. 3.6 *Modeled porosity variation along the column during experiments at 25 ºC (in green), 40 ºC (in orange) and 60 ºC (in red). Solid, dashed and dotted lines represent atmospheric, 10 bar and 34 bar pCO_2 conditions, respectively, and plain and empty-square lines indicate experiments with limestone and dolostone, respectively. Colored areas indicate simulated values using the initial ($A_{Gp\text{-}0}$) and final ($A_{Gp\text{-}f}$) gypsum reactive area. T effect under atmospheric and 10 bar of pCO_2, respectively (a and b), mineralogy effect (c) and pCO_2 effect on porosity changes (d). Variation of calcite saturation index (SI_{Cal}) along the column is shown in (a, b and d).*

It should be noted that the limestone dissolution rate decreased with temperature under both pCO_2 conditions in contrast to the reported increase in the calcite dissolution rate constants with temperature from 25 to 100 ºC and under pCO_2 from atmospheric to 55 bar (Pokrovsky

et al. 2005, 2009). An explanation for the observed *T* effect on the calcite dissolution rate was provided by the different solution saturation state along the column at different temperatures. From the CrunchFlow simulations run with the same reactive surface area of calcite (A_{Cal} = 120 m^2_m/m^3_{bulk}), it was deduced that dissolution at 25 ºC took place under more undersaturated conditions than at 60 ºC under all pCO_2 conditions (*i.e.*, SI_{Cal} is further from equilibrium at lower *T*; see SI_{Cal} variation of atmospheric and 10 bar pCO_2 experiments in Fig. 3.6a, b, respectively). Hence, the trend (faster dissolution rate at lower *T*) is driven by the solution saturation state rather than by the temperature dependence of the dissolution rate constant. The fact that CO_2 solubility is higher with decreasing temperature (Duan and Sun, 2003) also contributes to the observed trend of faster dissolution rate with decreasing temperature. The higher solubility results in buffering of the solution pH at lower values (see smaller pH values at lower *T* in Tables 2.4 and 3.1).

As regards the *T* effect on gypsum precipitation, results show that by lowering temperature, gypsum precipitation rate was favored under 10 bar of pCO_2 and not favored under atmospheric pressure (Fig. 3.5b). Under all pCO_2 conditions, two stages were distinguished in limestone column experiments where gypsum precipitated. In the first stage, to match the small initial S deficit, the same value of gypsum reactive area for all experiments was used ($A_{Gp} \approx 0.01$ m^2_m/m^3_{bulk}). In the second stage, this initial value was increased to match the growing S deficit as gypsum kept on precipitating. In the former stage, although the solution was slightly more supersaturated with respect to gypsum at the lowest *T*, the gypsum precipitation rate was faster at the highest *T*. This demonstrated that in this first stage the increased rate constants prevailed over the solution saturation state. In the latter stage, the dependence of the gypsum precipitation rate on *T* shows differences between experiments run under atmospheric and 10 bar of pCO_2 conditions. Under atmospheric pCO_2 conditions, since the difference in calcite dissolution rates at 25 and 60 ºC was slight, the initial trend remained and the gypsum precipitation rate was faster at the highest *T*. By contrast, under 10 bar of pCO_2 conditions the trend changed and the gypsum precipitation rate was faster at the lowest *T* owing to the larger Ca concentration at this *T* (Fig. 3.3a, b).

Overall, the coupled process of limestone dissolution and gypsum precipitation always increased porosity (under any pCO_2), the increase being higher at the lowest temperature (Fig. 3.5c). Simulations showed that an increase in temperature does not affect the trend of porosity variation along the column but reduces porosity creation under all pCO_2 conditions (Fig. 3.6a, b).

Likewise, in the experiments performed with the gypsum-undersaturated solution under 10 bar of pCO_2 (Table 3.1; *L25-10-gp-u* and *L40-10-gp-u*), the trend in limestone dissolution and porosity variation with temperature was the same (faster dissolution rate and larger increase in porosity at the lowest temperature). In these cases, gypsum did not precipitate and the amount of dissolved limestone and the porosity increase were slightly enhanced (Fig. B.4, *Appendix B*) with respect to those using gypsum-equilibrated solution under the same T and pCO_2 (Table 3.1; *L25-10-gp-e* and *L40-10-gp-e*). Given that calcite dissolution at the same T took place under very similar solution saturation states (Table 2.4; SI_{Cal} was -3.45 and -3.48 at 25 ºC with gypsum-undersaturated and gypsum-equilibrated solutions, respectively), the slightly smaller amount of dissolved limestone in experiments with a high sulfate content can be attributed to a sulfate inhibitory effect on the calcite dissolution rate (Gledhill and Morse, 2006; Sjöberg, 1978). Nonetheless, a passivation process due to formation of gypsum coatings on the calcite grain surfaces cannot be neglected (Offeddu et al., 2014, 2015).

(2) Mineralogy effect: Fig. 3.5d-f shows the differences between limestone and dolostone reactivity based on the results from two groups of experiments (Table 3.1; the first group performed under atmospheric pCO_2 (*L25-atm-s* and *D25-atm-s*) and the second group under 10 bar of pCO_2 (*L40-10-gp-e* and *D40-10-gp-e*)). The only difference between the two experiments in the same group is in the initial mineralogy: limestone (L) or dolostone (D). As a result of the slower dolomite dissolution kinetics (given by the values of the rate constants and the n^{H^+} exponents), $V_{L\text{-}diss}$ was higher than $V_{D\text{-}diss}$ regardless of solution composition, temperature and dissolved CO_2, but the difference between $V_{L\text{-}diss}$ and $V_{D\text{-}diss}$ increased with pCO_2 (Fig. 3.5d). For instance, after 100 pore volumes, $V_{L\text{-}diss}$ /$V_{D\text{-}diss}$ was 1.39 under atmospheric pCO_2 and 3.91 under 10 bar of pCO_2. This difference is also supported by the different increase between calcite and dolomite dissolution rates with increasing T (from 25 to 60 ºC) and pCO_2 (from atmospheric to 10 bar) reported in Prokrovsky et al. (2009). The reported increase in calcite dissolution rate is 5 times larger than in the case of dolomite. Therefore, the increase in T and pCO_2 in the experiments of this study was expected to have a larger effect on calcite than on dolomite.

The variation of volume of precipitated gypsum ($V_{Gp\text{-}ppt}$) versus the number of pore volumes (Fig. 3.5e) shows that under atmospheric pCO_2 conditions the amount of precipitated gypsum was smaller in the limestone experiments than in the dolostone

experiments. Under 10 bar of pCO_2, the gypsum precipitation rate was much faster than at atmospheric pCO_2 being faster in the limestone experiment than in the dolostone experiment. Gypsum precipitated immediately in the dolostone columns and only after 225 (atmospheric pCO_2) and 11 (10 bar of pCO_2) pore volumes in the limestone columns (Fig. 3.5e). Moreover, the gypsum precipitation rates as dolostone dissolved were fairly constant in contrast to the gradual increase in the gypsum precipitation rates that occurred during limestone experiments (Fig. 3.2b and 3.3d). The difference between the early and late gypsum precipitation could be attributed to the mineral induction time, which is the time elapsed between the establishment of supersaturation in a solution and the detection of a new phase in the system (nucleation; Söhnel and Mullin, 1988). This term is influenced by the presence of impurities in solution (*e.g.*, Al^{3+}, Mg^{2+}, Fe^{2+}; Gao et al., 2008; Rashad et al., 2004) and other parameters (*e.g.*, ionic strength and calcium content; Prisciandaro et al., 2001; Reznik et al., 2012).

Overall, as a result of the coupled processes of calcite and dolomite dissolution and gypsum precipitation, porosity increase was significantly larger in the limestone experiments than in the dolostone ones under both pCO_2 and T conditions (Fig. 3.5f). Under the same pCO_2, the trend of porosity variation along the column was similar in the limestone and dolostone experiments. However, the formation of porosity was greater at the inlet of the limestone experiments than in the dolostone experiments owing to the slower dolomite dissolution rate (Fig. 3.6c).

(3) pCO_2 effect: Limestone reactivity under different pCO_2 conditions was assessed by comparing the results of the experiments run under atmospheric, 10 and 34 bar of pCO_2 using gypsum-equilibrated solutions at 60 ºC (Table 3.1; experiments *L60-atm-a3.5, L60-10-gp-e and L60-34-gp-e*). Output pH rose to around 6.82 under atmospheric pCO_2 conditions but it increased only to 5.13 and 4.72 under 10 and 34 bar of pCO_2 (Table 3.1). The percentage of dissolved limestone and precipitated gypsum with respect to each initial sample volume was higher at the greater pCO_2. For instance, after 100 pore volumes $V_{L\text{-}diss}$ (%) and $V_{Gp\text{-}ppt}$ (%) were 0.28, 3.64, 4.95 and 0, 0.58, 0.77 under atmospheric, 10 and 34 bar of pCO_2, respectively (Fig. 3.5g, h). Likewise, porosity increased with pCO_2, being noticeably higher in the two high pCO_2 experiments (Fig. 3.5i).

The calcite dissolution rate was faster along the column under higher pCO_2 conditions. This behavior is directly attributed to the decrease in pH with increasing dissolved CO_2. Given that the input pH is around 3.5 in the three experiments, the faster calcite

dissolution rate at high pCO_2 (10 and 34 bar) is related to the weak character of the H_2CO_3 acid in contrast to the strong nature of the HCl acid used under atmospheric pCO_2. As a weak acid, H_2CO_3 acts as a pH buffer and dissociates partially yielding lower solution pH all over the column. As a result, under atmospheric pCO_2 the increase in porosity occurred exclusively near the inlet in contrast to the significant porosity increase along the column under 10 and 34 bar pCO_2 (Fig. 3.6d). This behavior is ascribed to the solution saturation state, which varies differently depending on pCO_2. Under atmospheric pCO_2, the solution reached equilibrium with calcite after a short distance from the inlet, whereas under 10 and 34 bar of pCO_2 it remained undersaturated along the column (Fig. 3.6d). Therefore, an increase in pCO_2 changed the pattern of porosity variation along the column, increasing the distance affected by dissolution. As regards gypsum precipitation, it took place primarily near the inlet, where the amount of dissolved limestone was greater.

The difference in calcite dissolution rates under different pCO_2 conditions in the experiments of this study in which TDS is about 30 g/L could diminish if ionic strength was higher, as argued by Gledhill and Morse (2006). These authors demonstrated that differences between rates under different pCO_2 conditions diminished with increasing solution concentration from 40 to 200 g/L and the effect was more pronounced at higher pCO_2.

Finally, to test the non linear effect of P on CO_2 solubility and mineral equilibria (through the molar volume of solutes) reported by Appelo et al. (2014), simulations using the CrunchFlow and PhreeqC (v.3) codes were compared. Using the same A_{Cal} value (120 m^2_m/m^3_{bulk}), despite the fact that the respective simulated output Ca concentration barely differed (Fig. 3.4a), gypsum did not precipitate in the PhreeqC (v.3) simulation because gypsum solubility increased owing to the P effect (Fig. 3.4b). Therefore, at $pCO_2 > 20$ bar, model calculations should consider the P effect on equilibrium constants to yield more reliable predictions.

3.4 Summary and conclusions

Experiments using columns filled with crushed limestone and dolostone with initial porosity of about 50% proved useful in gaining further insight into the effect exerted by mineralogy, temperature, injected synthetic solution composition and pCO_2 on reservoir rock reactivity.

As for the temperature effect, under all pCO_2 conditions, low temperature favored limestone dissolution rate although the calcite dissolution rate constants increase with temperature (up to 100 ºC; Pokrovsky et al., 2009). This inverse tendency was explained by the fact that limestone undersaturation increased by decreasing the temperature, which suggested that the process was thermodynamically controlled. Gypsum precipitated only if the injected solution was gypsum-equilibrated. Under the conditions of this study anhydrite precipitation did not occur. Using gypsum-undersaturated solutions, the amount of dissolved limestone was found to be slightly higher than that obtained with gypsum-equilibrated solutions. The high sulfate content in the latter solution probably inhibited calcite dissolution rate (Gledhill and Morse, 2006)).

As expected under our experimental conditions, the volume of dissolved limestone was larger than that of dolostone owing to the well-known faster calcite dissolution kinetics. Likewise, a pCO_2 increase implies a pH decrease that enhances substantially calcite dissolution rate with respect to that of dolomite (Pokrovsky et al., 2005, 2009). The volume of precipitated gypsum was always smaller than the volume of dissolved rock (whether limestone or dolostone), yielding in all cases a porosity increase. In addition, gypsum induction time was longer when limestone dissolved and precipitation increased gradually. When dolostone dissolved, gypsum precipitated quickly and precipitation remained steady.

When raising pCO_2, the limestone dissolution rate increased along the column because of the direct pH effect on the calcite dissolution rate. Dissolution of the carbonate minerals in acidic pH is controlled, under atmospheric pressure, by the protons provided by the strong acid (HCl or H_2SO_4), whereas under high pCO_2, H_2CO_3 partial dissociation controls the dissolution. Model results show that if solution acidity is controlled by a strong acid, dissolution occurs exclusively at the first rock-solution contact, raising the pH at ≈ 7 and limiting the limestone dissolution further away. In contrast, simulations under high pCO_2 conditions show that pH remains acidic (≈ 5) and the solution is permanently undersaturated with respect to calcite and dolomite (due to the carbonic acid buffer capacity), yielding a higher increase in porosity all over the rock-solution contact.

A good match between the CrunchFlow and PhreeqC (v.3) reactive transport calculations and the experimental data was obtained. Rate laws including the values of the rate constants were taken from literature. The fit of the model to the experimental data was performed by adjusting the values of the reactive surface areas. The calcite and dolomite

reactive surface area values had to be diminished by two orders of magnitude from the initially calculated geometric surface areas. A possible explanation for the small areas could be given by the transport (diffusion) control of the dissolution reactions at pH < 5. It should be noted that a single value of the reactive area for calcite provided a good fit of the model to all experimental results, supporting the applicability of this modeling approach. The values for dolomite were more variable but continued to be within the model uncertainty.

Part III:

Fractured Cores

Chapter 4

Influence of the flow rate on dissolution and precipitation features during percolation experiments with fractured limestone and sandstone cores

4.1 Introduction

This chapter presents the experimental results of a set of percolation experiments which consist of injecting CO_2-rich solutions through fractured core samples under Hontomín reservoir conditions. Cores were made of limestone and sandstone rocks from the Hontomín reservoir. Experiments were run under different flow rates and sulfate content of the injected solution. X-ray computed microtomography (XCMT) was used to characterize changes in fracture volume induced by dissolution and precipitation processes. In addition, measurement of the pressure difference between the inlet and the outlet of the sample and of the aqueous chemistry enabled the determination of permeability changes and net reaction rates. A discussion including the influence of flow rate on the reactions, evolution of dissolution patterns and permeability changes during fracture dissolution is likewise presented.

Note: This chapter is based on the submitted article to Int. J. Greenh. Gas Control: Garcia-Rios, M., Luquot, L., Soler, J.M., Cama, J. 2015. Influence of the flow rate on dissolution and precipitation features during percolation of CO_2-rich sulfate solutions through fractured limestone samples.

4.2 Results

Table 4.1 shows the list of the percolation experiments. Core and fracture dimensions and mineralogical composition of limestone and sandstone samples were described in *Section 2.1.1* (Table 2.1, Fig. 2.2). Three different input solutions were injected through the fractured limestone and sandstone cores (sulfate-free solution *no-s*, gypsum-undersaturated solution *gp-u* and gypsum-equilibrated solution *gp-e*; *Section 2.1.2*; Table 2.2). All experiments were run under P = 150 bar, pCO_2 = 62 bar and T = 60 ºC, and flow rates varied from 0.2 to 60 mL/h. Two flow-through apparatus (Icare Lab CSS I, Luquot and Gouze, 2009, and Icare Lab CSS II, Luquot et al., 2012) were used to reproduce the *in situ* reservoir conditions for CO_2 sequestration (*Section 2.1.3*; Fig. 2.3c).

Table 4.1 *List of the percolation experiments.*

Experiment label	Q (mL/h)	Input solution label
LIMESTONE (L)		
L1-no-s	1	*no-s*
L60-no-s	60	*no-s*
L0.2-gp-e	0.2	*gp-e*
L1-gp-e	1	*gp-e*
L5-gp-e	5	*gp-e*
L60-gp-e	60	*gp-e*
SANDSTONE (S)		
S1-no-s	1	*no-s*
S5-no-s	5	*no-s*
S60-no-s	60	*no-s*
S5-gp-u	5	*gp-u*
S60-gp-u	60	*gp-u*
S0.2-gp-e	0.2	*gp-e*
S1-gp-e	1	*gp-e*
S5-gp-e	5	*gp-e*
S60-gp-e	60	*gp-e*

Labels of the experiments are coded by rock type, flow rate Q and input solution label: **rock*Q*-input label.**
All experiments were run under P = 150 bar, $p\,CO_2$ = 62 bar and T = 60 °C.
no-s = sulfate-free solution.
gp-u = gypsum-undersaturated solution.
gp-e = gypsum-equilibrated solution.

4.2.1 Initial fracture characterization

The initial fracture aperture was obtained by means of three independent experimental measurements: (1) hydraulic aperture a_h determined from hydraulic test using Eq. (2.10), (2) geometric aperture a_{Xr} obtained from X-ray computed microtomography (XCMT) data, and (3) geometric aperture a_s obtained from scanning electron microscopy (SEM) examination. The relationship between the aperture $a(t)$ and the volume $V(t)$ of the fracture at initial time ($t = t_0$) was considered to be $V(t_0) = d \cdot L \cdot a(t_0)$, assuming that the initial fracture volume was defined as a parallelepiped. Table 4.2 shows the obtained fracture aperture and fracture volume values at $t = t_0$ (comparison of a_h, a_{Xr} and a_s).

Table 4.2 *Measured (weighted) mass of fractured core (M_{meas}), fracture permeability (k), and fracture geometry (a and V) obtained by hydraulic measurement (a_h and V_h), XCMT (a_{Xr} and V_{Xr}) and SEM (a_s and V_s) at initial time ($t = t_0$).*

t = t_0		**Hydraulic measurement**			**XCMT**		**SEM**		**comparison**	
Experiment label	**M_{meas}** g	***k*** m^2	**a_h** µm	**V_h** mm^3	**a_{Xr}** µm	**V_{Xr}** mm^3	**a_s** µm	**V_s** mm^3	**a_h/a_s**	**a_{Xr}/a_s**
LIMESTONE										
L1-no-s	2.995	9.25E-13	3.33	0.56	-	7.47	6.4	1.07	0.5	-
L60-no-s	3.015	-	-	-	-	4.84	4.1	0.70	-	-
L0.2-gp-e	-	-	-	-	-	-	9.0	1.48	-	-
L1-gp-e	2.739	-	-	-	30.91	8.06	6.7	1.06	-	4.6
L5-gp-e	2.850	4.64E-13	2.36	0.37	-	5.71	5.3	0.82	0.4	-
L60-gp-e	2.690	8.49E-12	10.10	1.57	38.07	7.94	8.1	1.26	1.2	4.7
SANDSTONE										
S1-no-s	2.974	6.72E-13	2.84	0.49	-	-	7.1	1.22	0.4	-
S5-no-s	2.896	3.44E-13	2.03	0.33	-	2.85	2.5	0.41	0.8	-
S60-no-s	2.831	4.34E-12	7.22	1.19	-	10.52	9.2	1.51	0.8	-
S5-gp-u	2.852	-	-	-	-	4.33	3.8	0.62	-	-
S60-gp-u	2.685	-	-	-	-	7.67	7.2	1.10	-	-
S0.2-gp-e	3.101	-	-	-	-	-	9.2	1.56	-	-
S1-gp-e	2.865	-	-	-	35.78	7.44	6.4	1.06	-	5.6
S5-gp-e	2.850	1.76E-12	4.60	0.74	-	-	5.2	0.84	0.9	-
S60-gp-e	3.092	1.24E-11	12.19	2.10	-	11.38	9.50	1.63	1.3	-

a_h and V_h = hydraulic aperture and volume.

a_{Xr} and V_{Xr} = geometric aperture and volume from XCMT; V_{Xr} values with grey background correspond to experiments where XCMT was not performed, and were calculated using the relationship between SEM and XCMT results of experiments *L1-gp-e*, *L60-gp-e* and *S1-gp-e* (see *Section 4.3.1*).

a_s and V_s = geometric aperture and volume from SEM.

Initial hydraulic aperture $a_h(t_0)$ and fracture permeability $k(t_0)$ could only be calculated according to Eqs. (2.10) and (2.11) in the eight percolation experiments where ΔP was measurable (Table 4.2; $k(t_0)$, $a_h(t_0)$ and $V_h(t_0)$). In the other seven experiments ΔP was smaller than the minimum measurable value from the beginning of the experiment. Three unreacted fractured cores were characterized by XCMT (Table 4.2; $a_{Xr}(t_0)$ and $V_{Xr}(t_0)$; exp. *L1-gp-e*, *L60-gp-e* and *S1-gp-e*). Data was acquired at the National Institute for Lasers, Plasma and Radiation Physics (NILPRP; Bucharest-Magurele, Romania), and the processing of the X-ray microtomography data was carried out by Voxaya (Montpellier, France), providing characterization of the fracture geometry. Once the percolation experiments were finished, SEM analyses of all fractured samples were performed to obtain the dimensions of the fracture and observe features of mineral dissolution and precipitation. From SEM images, the initial fracture aperture could be measured in unaltered fracture regions, near the outlet and far away from the dissolution front (Table 4.2; $a_s(t_0)$ and $V_s(t_0)$). Detailed information about XCMT data acquisition and SEM analyses is presented in *Section 2.1.1*.

Initial fracture characterization was performed by all three methods mentioned only for experiment *L60-gp-e*. Good agreement was observed between the measured parameters using hydraulic and SEM methods (Table 4.2; $a_h(t_0)/a_s(t_0)$ = 1.2). In contrast, results from XCMT were noticeably higher (Table 4.2; $a_{Xr}(t_0)/a_s(t_0)$ = 4.7).

Good agreement between hydraulic measurement and SEM was also obtained in the four other experiments where $a_h(t_0)/a_s(t_0)$ varied from 0.8 to 1.3, and was poorer in the three other experiments where $a_h(t_0)/a_s(t_0)$ ranged from 0.4 to 0.5 (Table 4.2). Discrepancy between these two methodologies could be explained by the fact that the initial fracture apertures obtained from hydraulic measurement correspond to the minimum aperture of the fracture (controlling permeability), whereas those from SEM were an average of four measured values where reaction was not supposed to occur. However, significantly larger discrepancies existed when XCMT results were compared with those obtained with hydraulic measurement and SEM, which could be attributed to the limited resolution of the technique (14 μm of pixel size) and the high background noise from the data. For the three experiments where the sample was characterized by XCMT, $a_{Xr}(t_0)/a_s(t_0)$ was around 5.

4.2.2 Aqueous chemistry

Fig. 4.1 illustrates the variation in Ca and S concentration over time during limestone experiments, and Fig. 4.2 shows the variation in Ca, S and Si concentration over time during sandstone experiments. Note that variation in chemical composition of experiment *S5-no-s* is not shown in Fig. 4.2 because technical problems prevented the measurement.

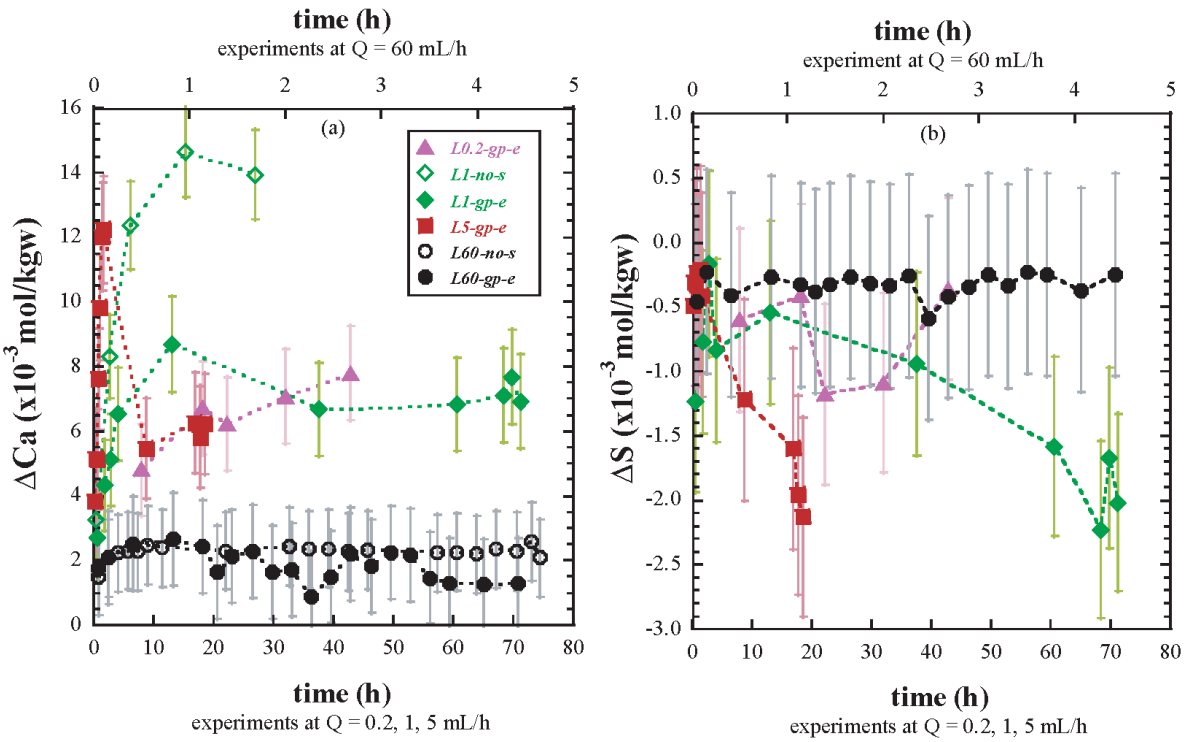

Fig. 4.1 *Variation in the increase of Ca (a) and S (b) concentrations over time in the percolation experiments with fractured limestone cores, using no-s input solution (open symbols) and gp-e input solution (solid symbols) at Q = 0.2 mL/h (in violet), Q = 1 mL/h (in green), Q = 5 mL/h (in red) and Q = 60 mL/h (in black). Time for experiments at Q = 0.2, 1 and 5 mL/h is plotted in the lower x-axis and time for experiments at Q = 60 mL/h is plotted in the upper x-axis.*

The output Ca concentration in both limestone and sandstone experiments was always higher than the input concentration throughout the entire experimental run ($\Delta Ca > 0$), indicating calcite dissolution (dotted lines in Fig. 4.1a and Fig. 4.2a). Overall, the Ca concentration increase was larger at slow flow rates (Q from 0.2 to 5 mL/h) than at the highest flow rate (Q = 60 mL/h). At the slowest flow rate (Q = 0.2 mL/h), the output Ca concentration continuously increased throughout the experiment. In some experiments with Q from 1 to 5 mL/h, Ca was released in two stages defined by an initial peak of ΔCa followed by a sharp decrease to approach an almost unvarying concentration (*e.g.*, exp. *L1-gp-e* and

L5-gp-e). At Q = 60 mL/h, ΔCa was fairly constant during the entire experimental run. Moreover, in the experiments run at the same flow rate (Q = 1, 5 or 60 mL/h) but with different input solution (*no-s*, *gp-u* or *gp-e*), ΔCa was larger in those with lower input S concentration (open and semi-solid symbols in Fig. 4.1a and Fig. 4.2a).

In both the limestone and sandstone experiments with S concentration in the injected solution (*gp-u* and *gp-e*), the output S concentration was always lower than the input one, leading to a permanent S deficit (ΔS < 0; dashed lines in Fig. 4.1b and Fig. 4.2b). In experiments run under slow flow rates (Q = 0.2, 1 and 5 mL/h) ΔS was very small (zero within the analytical error) during the early stage, whereas in the experiments with the fastest flow rate (Q = 60 mL/h) this small value was observed during the whole experiment. Sulfur deficit indicated precipitation of a sulfur-rich mineral.

In sandstone experiments the measured output Si concentration was slightly higher than the input one (solid lines in Fig. 4.2b). Given that the calculated pH ranged from 3.3 to 4.4 during the experiments (*Chapter 5*), Si was only released from dissolving microcline since quartz dissolution rate is negligible at acid pH (Bandstra et al., 2008). In addition, Si concentration increased by decreasing flow rate. Owing to the obtained low output Si concentration, microcline dissolution was not taken into account to calculate the changes in fracture volume shown in *Section 4.3.1*.

4.2.3 Permeability

Fracture permeability $k(t)$ was calculated according to Eq. (2.11) in the eight percolation experiments where $\Delta P(t)$ could be measured (Table 4.2). In the other seven experiments, $\Delta P(t)$ was initially smaller than the minimum measurable value ($\Delta P < \Delta P_{min}$) preventing $k(t)$ calculation. Fig. 4.3 shows that fracture permeability increased over time in the eight experiments regardless of the sulfur content of the injected solution. Note that precipitation of a S-rich phase did not prevent the permeability increase.

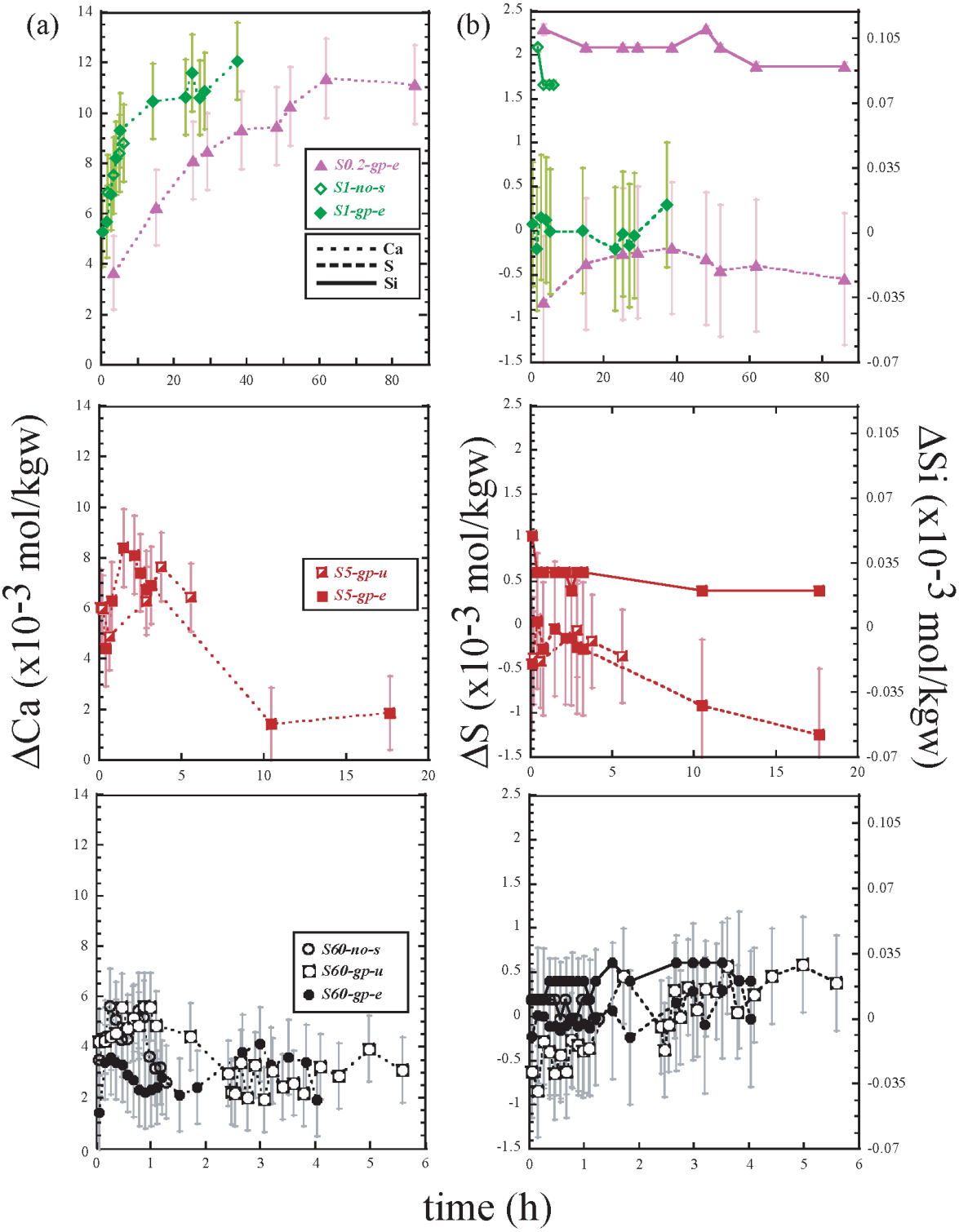

Fig. 4.2 *Variation in the increase of Ca (left column-a) and S and Si (right column-b) concentrations over time in the percolation experiments with fractured sandstone cores, using no-s input solution (open symbols), gp-u solution (semi–solid symbols) and gp-e input solution (solid symbols) at Q = 0.2 mL/h (in violet), Q = 1 mL/h (in green), Q = 5 mL/h (in red) and Q = 60 mL/h (in black). Dotted lines in (a) indicate Ca concentrations and solid and dashed lines in (b) indicate Si and S concentrations, respectively.*

In all limestone experiments, two stages were observed (Fig. 4.3a). In the initial stage the increase in permeability was much slower than in the second one. In particular, in the S-rich experiments (*L5-gp-e* and *L60-gp-e*), the initial stage was longer than in the S-free experiment (*L1-no-s*) and shorter in the experiment with the fastest flow rate (*L60-gp-e*). All sandstone experiments showed a stepped increase in permeability with steps becoming shorter by increasing flow rate (Fig. 4.3b). Exceptionally, in experiment *S5-gp-e*, the permeability increased similarly to that in limestone experiments (*i.e.*, an initial slow stage followed by a fast one). The different behavior of permeability increase between limestone and sandstone experiments is related to different developed dissolution patterns, as explained in *Section 4.3.4*. Note also that in experiment *S60-gp-e* the permeability increase was suddenly interrupted by a sharp fall, likely caused by detachment of quartz grains. Nonetheless, an immediate recover of permeability indicated that this phenomenon itself was unable to prevent the permeability increase in contrast to reported permeability reduction by transport of particles in limestone percolation experiments (Luquot et al., 2014).

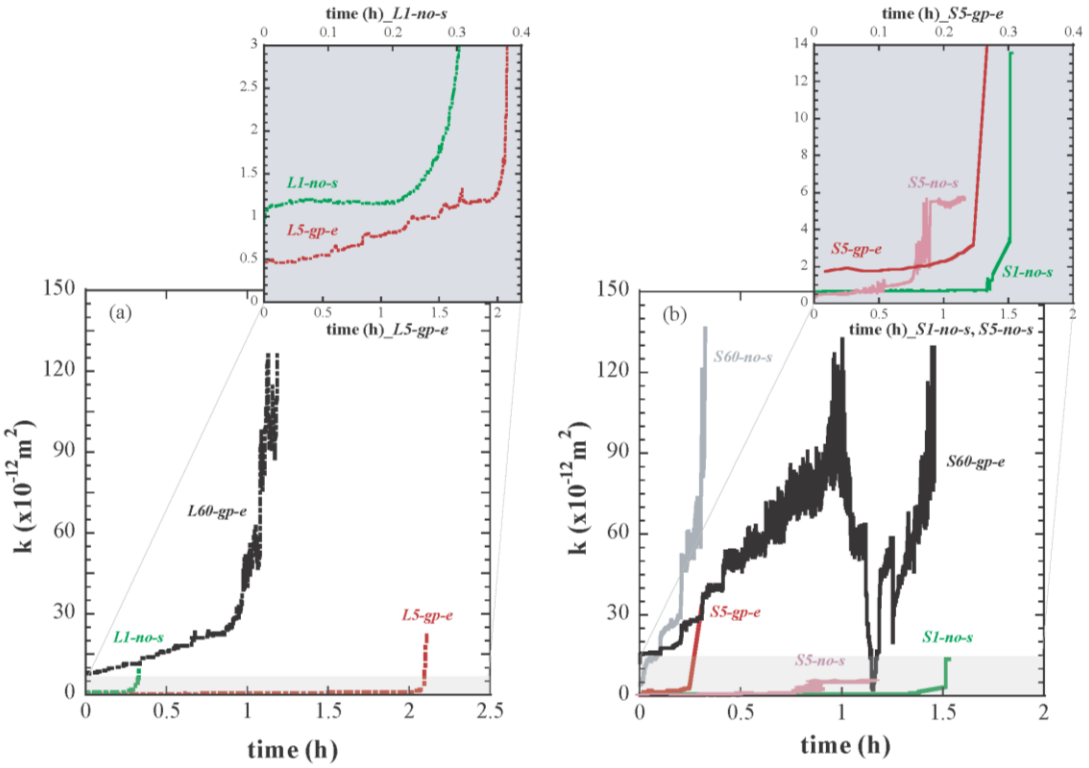

Fig. 4.3 *Variation in fracture permeability during limestone (dashed lines-a) and sandstone (solid lines-b) experiments. Q = 1 mL/h (green line), Q = 5 mL/h (red and pale red lines) and Q = 60 mL/h (black and grey lines). In the plots with grey background, upper-x axis indicates time for exp. L1-no-s and S5-gp-e and lower-x axis shows time for exp. L5-gp-e, S1-no-s and S5-no-s.*

4.2.4 Identification of dissolution and precipitation processes

The most prominent mineralogical change during any CO_2-flooding experiment is carbonate dissolution (Weibel et al., 2011). Indeed, the changes in solution chemistry observed in the current limestone and sandstone experiments were mostly bound to calcite dissolution ($\Delta Ca > 0$). In the sandstone experiments, the low Si release ($\Delta Si > 0$) was associated to microcline dissolution. Feldspar dissolution is commonly reported in CO_2 experiments (*e.g.*, Fisher et al., 2010; Wandrey et al., 2011). However, given the slow feldspar dissolution rate relative to that of calcite (about five orders of magnitude) at the pH of this study (3.3-4.4), and the short duration of the experiments (up to ≈ 100 h), feldspar dissolution is of little significance in these experiments.

Changes in solution chemistry in the experiments with S-rich injected solution indicated precipitation of a S-rich phase ($\Delta S < 0$). MicroRaman analysis showed that this S-rich phase was always gypsum (Fig. 4.4).

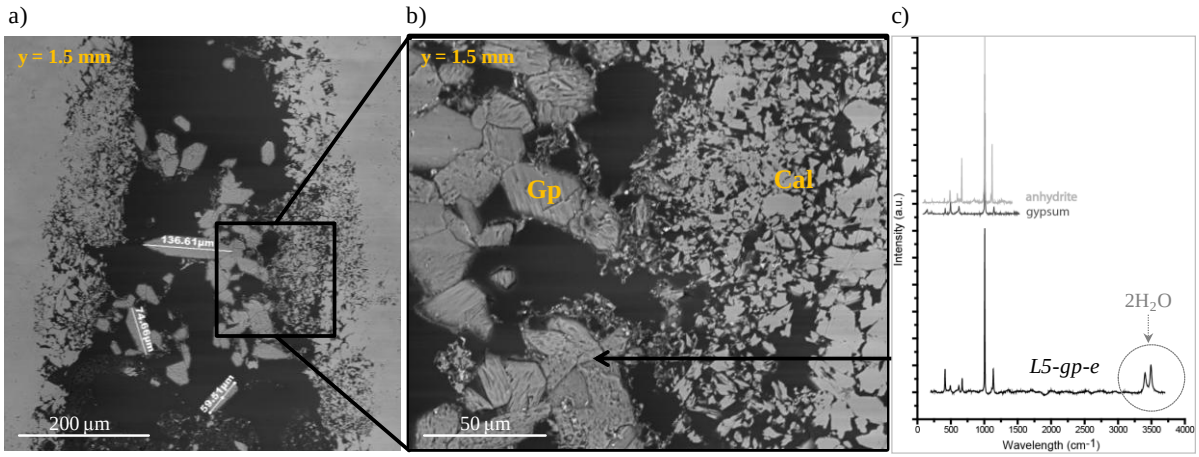

Fig. 4.4 *SEM images and MicroRaman spectrum of a thin section (section 2 in Fig. 2.2a) from the reacted fracture in experiment L5-gp-e: (a) dissolved calcite in the fracture surfaces and precipitated gypsum crystals. (b) Detailed view of the gypsum (Gp) crystals that grow at the expense of calcite (Cal) dissolution. Note the strong alteration of the fracture surfaces leading to formation of high microporosity. The y values indicate the distance from the inlet (y = 0) of the fracture along the flow direction (y). (c) MicroRaman spectra. The presence of the two characteristic peaks of water at ≈ 3500 cm^{-1} confirms that gypsum is the sulfate precipitated phase. The standard spectra of gypsum and anhydrite are from Downs (2006).*

XCMT and SEM were used to identify and localize these reactions along the fractures. In the limestone samples, two different types of thin sections were prepared from the reacted cores according to the observed fracture evolution. Sections parallel to the flow

direction (section 1 in Fig. 2.2a) were prepared in cores where partial or no wormhole formation occurred (*L1-no-s* and *L0.2-gp-e*). Several sections perpendicular to the flow direction (section 2 in Fig. 2.2a) were prepared from cores with a well-formed wormhole (*L60-no-s*, *L1-gp-e* and *L5-gp-e*), allowing better visualization of wormhole characteristics (*e.g.*, diameter) and accompanying structures (dissolution patterns, gypsum growth, etc.). In the sandstone samples, only sections parallel to the flow direction (section 1 in Fig. 2.2a) were sufficient to characterize the resulting more uniform dissolution features in the evolved fractures. Sectioning could induce formation of micro-cracks but, as it is explained in the following sections, they did not intervene in the fracture reactivity. SEM images of the thin sections (limestone: Fig. 4.5 and Fig. 4.6; sandstone: Fig. 4.9 and Fig. 4.10) and XCMT images (limestone: Fig. 4.7; sandstone: Fig. 4.11) illustrate the evolved morphology of the fractures.

4.2.4.1 Limestone samples

SEM images of the experiments with *no-s* input solution (only calcite dissolution; Fig. 4.5) showed significant dissolution from the inlet to near the outlet in the 1 mL/h experiment (*L1-no-s*; Fig. 4.5a) and formation of a single wormhole with a regular diameter (≈ 800 μm) in the 60 mL/h experiment (*L60-no-s*; Fig. 4.5b). In both cases the reacted fracture surfaces showed different alteration, yielding a rough surface in the former and a smooth surface in the latter, where the flow rate was faster. Additionally, Fig. 4.5a showed the existence of some micro-cracks parallel to the fracture likely formed during sectioning. Given that they were not percolated fractures and did not display any dissolution feature, it was assumed that they did not intervene in the overall fracture reactivity. Values of the initial fracture aperture shown in Table 4.2 ($a_s(t_0)$ and $V_s(t_0)$) were measured from the unreacted fracture regions near the outlet (indicated by red-dotted arrows in Fig. 4.5). In the 1 mL/h experiment, the dissolution feature observed in the SEM image was confirmed to be a wormhole by means of the XCMT image. This wormhole diverted and developed branching near the outlet (Fig. 4.7a). XCMT images of the 60 mL/h experiment corroborated the development of a single wormhole with regular morphology that formed along the left side of the fracture (Fig. 4.7b).

SEM and XCMT images of the experiments with *gp-e* input solution are shown in Fig. 4.6 and Fig. 4.7c-e, respectively. Precipitation of gypsum induced by calcite dissolution in S-rich solutions was solely observed in the 1 and 5 mL/h experiments (*L1-gp-e* and *L5-gp-*

e). In the 0.2 and 60 mL/h experiments (*L0.2-gp-e* and *L60-gp-e*), gypsum precipitation was not observed, yet it was indicated by aqueous chemistry (Table 4.3; $V_{Gp-ppt}(t_f)$). Possible reasons are described in *Section 4.3.1*.

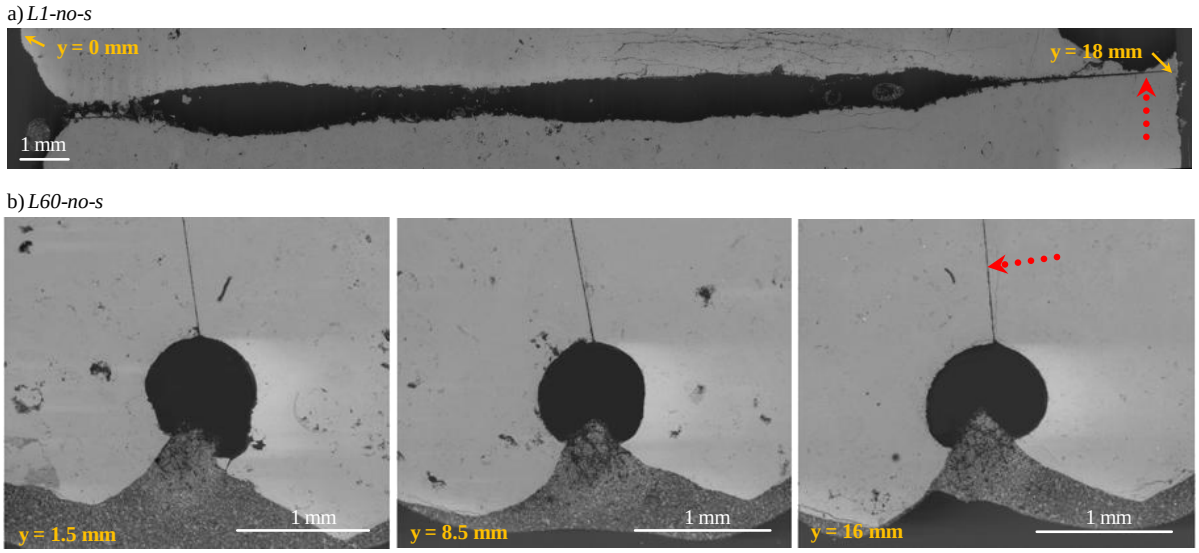

Fig. 4.5 *SEM images of the reacted limestone fractures in experiments with no-s input solution at (a) Q = 1 mL/h (L1-no-s, section 1) and (b) Q = 60 mL/h (L60-no-s, section 2). Red-dotted arrows indicate where the initial fracture aperture was measured (Table 4.2). The y values indicate the distances from the inlet (y = 0) of the fracture along the flow direction (y). Yellow arrows in (a) point out core heights, which are given by the y values (mm).*

Fig. 4.6a shows that, for the 0.2 mL/h experiment, little calcite dissolution occurred along the fracture, being more intense at the inlet (Fig. 4.6a; y = 0 mm; maximum fracture aperture of 24 μm). Development of microporosity was not observed in the SEM image likely due to minor calcite dissolution. A micro-crack parallel to the fracture was also observed in this sample, likely formed during sectioning but, as occurred in experiment *L1-no-s*, it did not intervene in fracture reactivity.

In the 1 mL/h experiment, SEM images in Fig. 4.6b show a single wormhole along the fracture with greater diameter at the inlet (1.12 mm) than at the outlet (850 μm) and development of microporosity in the fracture surfaces. Significant gypsum precipitation, that was inferred from the aqueous chemistry, was readily detected. The amount and size of gypsum crystals decreased along the wormhole (Fig. 4.6b). The wormhole started at the center of the fracture, where the initial permeability was probably higher due to

heterogeneity. Thereafter, it evolved parallel to a side of the core where a zone with high permeability formed owing to the lateral sealing of the fracture (Fig. 4.7c).

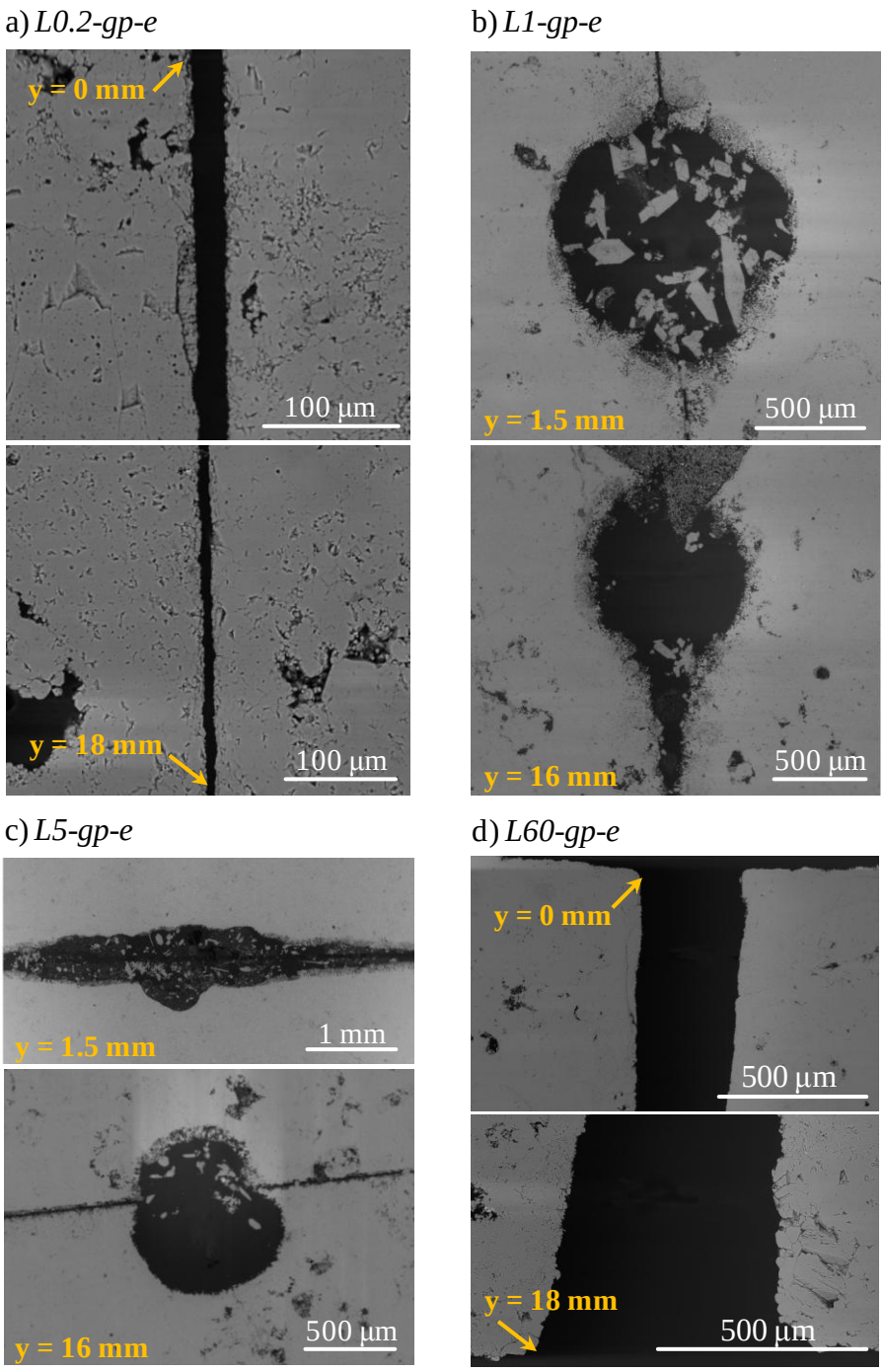

Fig. 4.6 *SEM images of the reacted limestone fractures in experiments with gp-e input solution at (a) Q = 0.2 mL/h (L0.2-gp-e, section 1), (b) Q = 1 mL/h (L1-gp-e, section 2), (c) Q = 5 mL/h (L5-gp-e, section 2) and (d) Q = 60 mL/h (L60-gp-e, section 1). Precipitated gypsum and development of microporosity (rough fracture surface) are observed in experiments at Q = 1 and 5 mL/h. Smooth fracture surface is observed in the experiment at Q = 60 mL/h. The y values indicate the distances from the inlet (y = 0) of the fracture along the flow direction (y). Yellow arrows in (a) and (d) point out the core height, which is given by the y value (mm).*

In the 5 mL/h experiment, uniform dissolution occurred up to around 3.5 mm from the inlet. From this point onwards, a single wormhole developed with a regular diameter (850 μm) (Fig. 4.6c and Fig. 4.7d). As in the 1 mL/h experiment, gypsum precipitation was readily detected and the amount and size of gypsum crystals decreased along the wormhole. Gypsum grew abundantly in localized areas of the wormhole, where the roughness of calcite surface increased (Fig. 4.6c; y = 16 mm; large development of microporosity in calcite surface).

SEM images of the 60 mL/h experiment showed significant dissolution near the inlet and the outlet of the fracture, as well as smooth fracture surfaces (Fig. 4.6d). The XCMT image of the reacted fracture (Fig. 4.7e) shows the wormhole to be wider near the inlet and that was displaced to a side of the core further downstream, probably because of the heterogeneity induced by the lateral resin sealing (as occurred in the exp. with Q = 1 mL/h shown in Fig. 4.7c). The preferential path started to form in the region where initial permeability was high due to existence of heterogeneity (see A' in Fig. 4.7e).

The fracture-length profiles from XCMT depicted in Fig. 4.8 show distinct evolution of the dissolution and precipitation processes along the fractures. Blue lines indicate the initial fracture volumes for experiments *L1-gp-e* and *L60-gp-e*. Black lines correspond to the total fracture volume after reaction, which includes initial fracture volume and volume obtained from dissolution ($V_{Xr} + V_{Xr-ppt}$; Table 4.3), and orange lines show the largest connected volume from dissolution (*e.g.*, wormhole).

If localized dissolution (wormhole) occurs along the fracture, the difference between the total and the connected volume from dissolution should be practically the initial fracture volume. However, if uniform dissolution occurs along the fracture it is to be expected that the profiles of total and connected fracture volumes are very similar (*e.g.*, from y = 13 to 16 mm in Fig. 4.8a and Fig. 4.7a; from y = 0 to 3 mm in Fig. 4.8d and Fig. 4.7d). It was also observed that deviations of the preferential channel were directly connected with an increase in dissolution (bends in Fig. 4.7 and increases in dissolution in Fig. 4.8 are both marked with blue arrows). Volume profiles also corroborated that precipitation occurred all over the fracture being more intense at the inlet where significant dissolution took place (Fig. 4.8c, d).

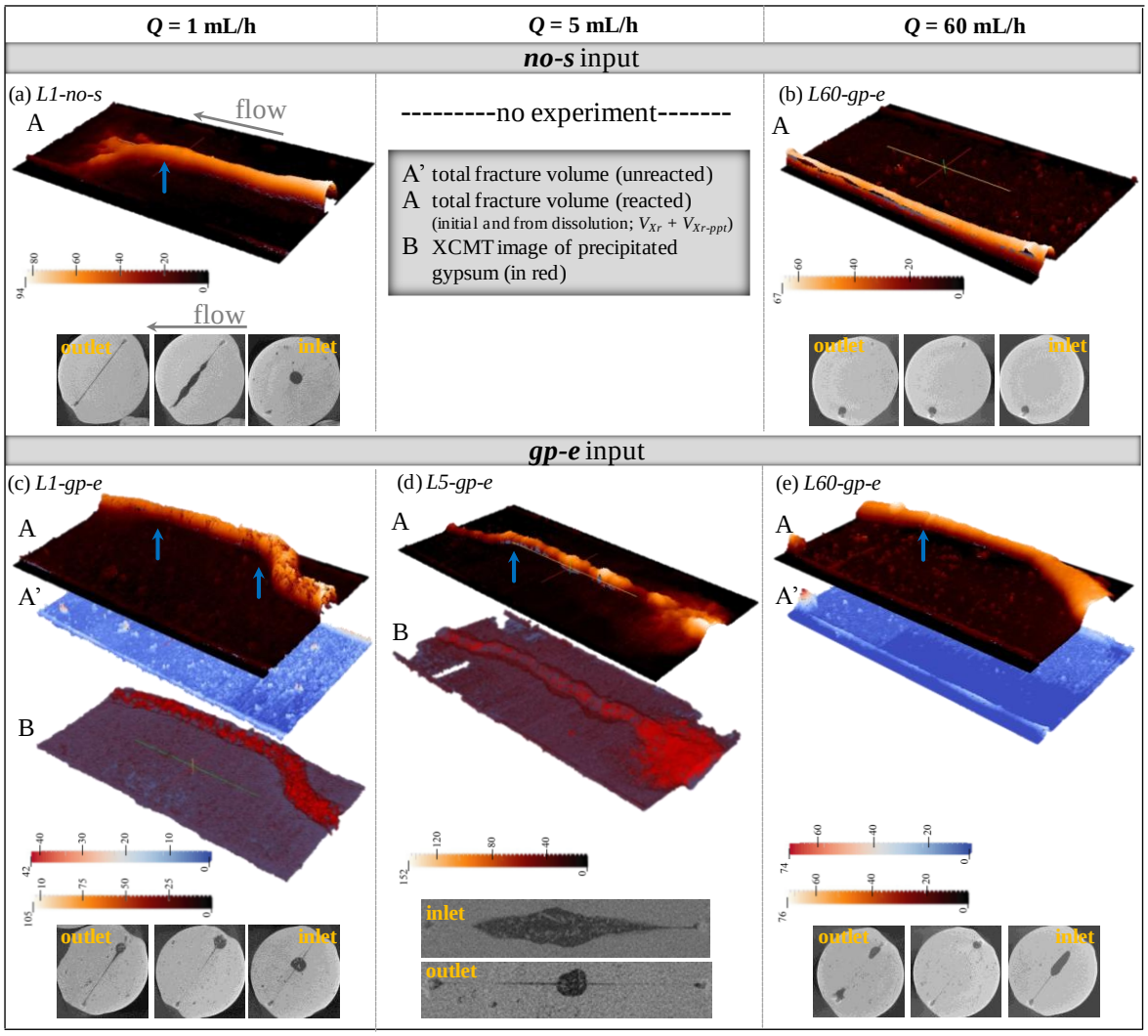

Fig. 4.7 *XCMT results. Total volume of reacted (A) and unreacted (A') fractures and images of the precipitated gypsum (B) in limestone experiments with no-s solution at (a) Q = 1 mL/h and (b) Q = 60 mL/h and experiments with gp-e solution at (c) Q = 1 mL/h, (d) Q = 5 mL/h and (e) Q = 60 mL/h. Arrows indicate bends of the preferential flow channels. Color scale bars are in pixels (1 pixel = 14 µm). Black and white sections (perpendicular to flow) show the fracture morphology with associated dissolution patterns from the inlet (right) to the outlet (left) of the cores.*

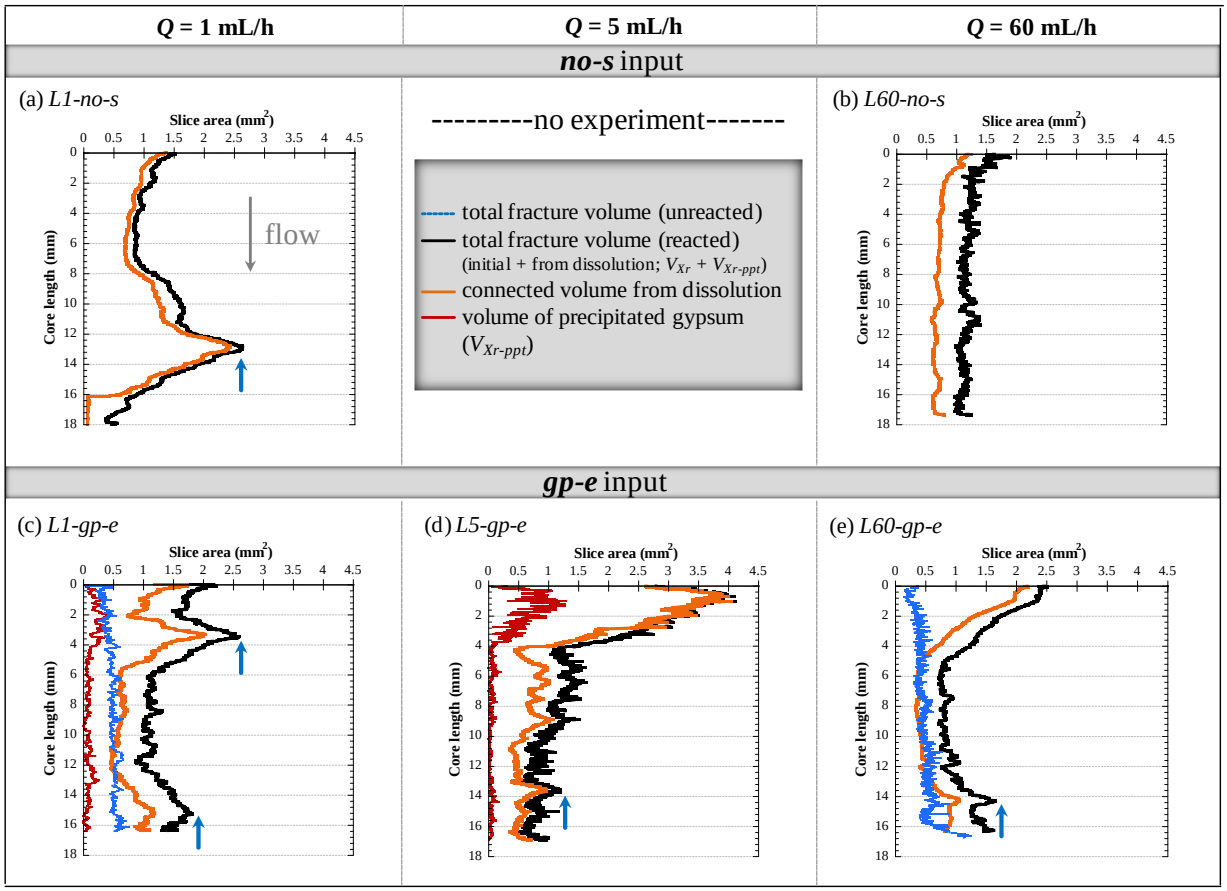

Fig. 4.8 *Fracture-length profiles that show the volume of unreacted (blue lines) and reacted (black lines) fractures, the largest connected volume from dissolution (orange lines) and the volume of precipitated gypsum (red lines) in exps. with no-s solution at (a) Q = 1 mL/h and (b) Q = 60 mL/h, and exps. with gp-e solution at (c) Q = 1 mL/h, (d) Q = 5 mL/h and (e) Q = 60 mL/h. Arrows point out volume increases that took place at the bends of the preferential flow channels (see Fig. 4.7).*

4.2.4.2 Sandstone samples

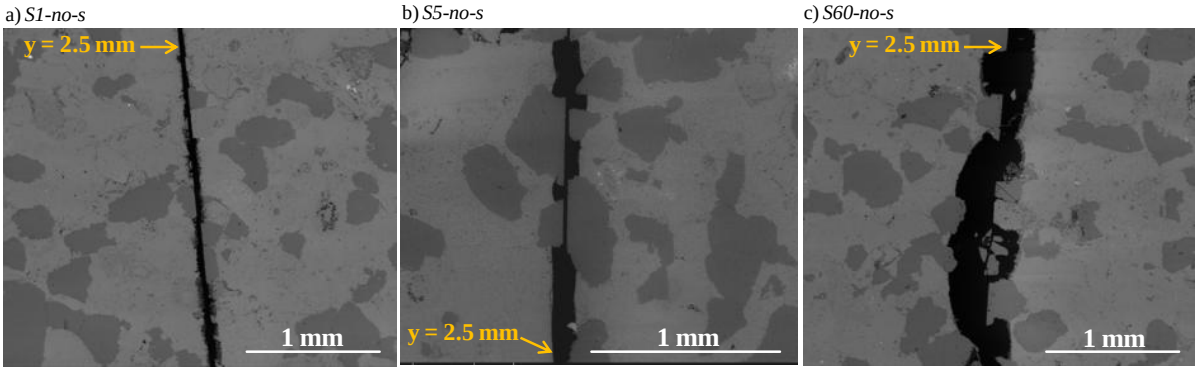

Fig. 4.9 *SEM images of the reacted sandstone fractures in experiments with no-s input solution at (a) Q = 1 mL/h (S1-no-s), (b) Q = 5 mL/h (S5-no-s) and (c) Q = 60 mL/h (S60-no-s). The y values indicate the distances from the inlet (y = 0) of the fracture along the flow direction (y). Yellow arrows point out the core height, which is given by the y value (mm).*

SEM images of the experiments with *no-s* input solution showed only calcite dissolution, leaving non-dissolved grains of quartz and microcline along the fracture. This phenomenon led to non-uniform aperture increases, independently of the flow rate, but the faster the flow rate the larger the non-uniformity (Fig. 4.9). XCMT images showed that at Q = 1 mL/h calcite dissolution was little and uniform along the fracture (Fig. 4.11a). XCMT was not performed in this experiment. At Q = 5 ml/h, calcite dissolution yielded uniform dissolution from the inlet to the middle of the fracture and a wormhole from the middle to the outlet (Fig. 4.11b). At Q = 60 mL/h, uniform dissolution took place along the fracture but slightly localized at the inlet (Fig. 4.11c).

In the S-rich experiments with *gp-u* solution XCMT images showed only calcite dissolution. Although gypsum precipitation was inferred from aqueous chemistry (Table 4.3), gypsum crystals were not observed by XCMT. Increasing the flow rate dissolution patterns changed from wormhole (Q = 5 mL/h; Fig. 4.11d) to nearly uniform dissolution (Q = 60 mL/h; Fig. 4.11e).

SEM images of the S-rich experiments using *gp-e* solution showed negligible dissolution at the slowest flow rate experiment. Noticeable dissolution, but differently distributed along the fracture, was observed in the rest of experiments with higher flow rate (Fig. 4.10). In the 1 and 60 mL/h experiments, dissolution was mostly homogeneous along the fracture except at the outlet, whereas in the 5 mL/h experiment it was localized around the middle of the fracture (Fig. 4.10). Other than calcite dissolution, precipitation of gypsum and an unidentified phase was observed. While gypsum crystals grew at expense of calcite dissolution, the unknown phase formed at expense of microcline dissolution (close-up images in Fig. 4.10b). SEM-EDX analysis indicated that this phase was formed of Si, Al, and K but it could not be identified by microRaman since fluorescence emission masked the Raman signal. XCMT images revealed that the dissolution was initially controlled by wormhole formation to finish up as a uniform in the 1 mL/h experiment. In contrast, at 60 mL/h the process occurred inversely (Fig. 4.11f, h). X-ray microtomography was not perfomed in the 5 mL/h experiment.

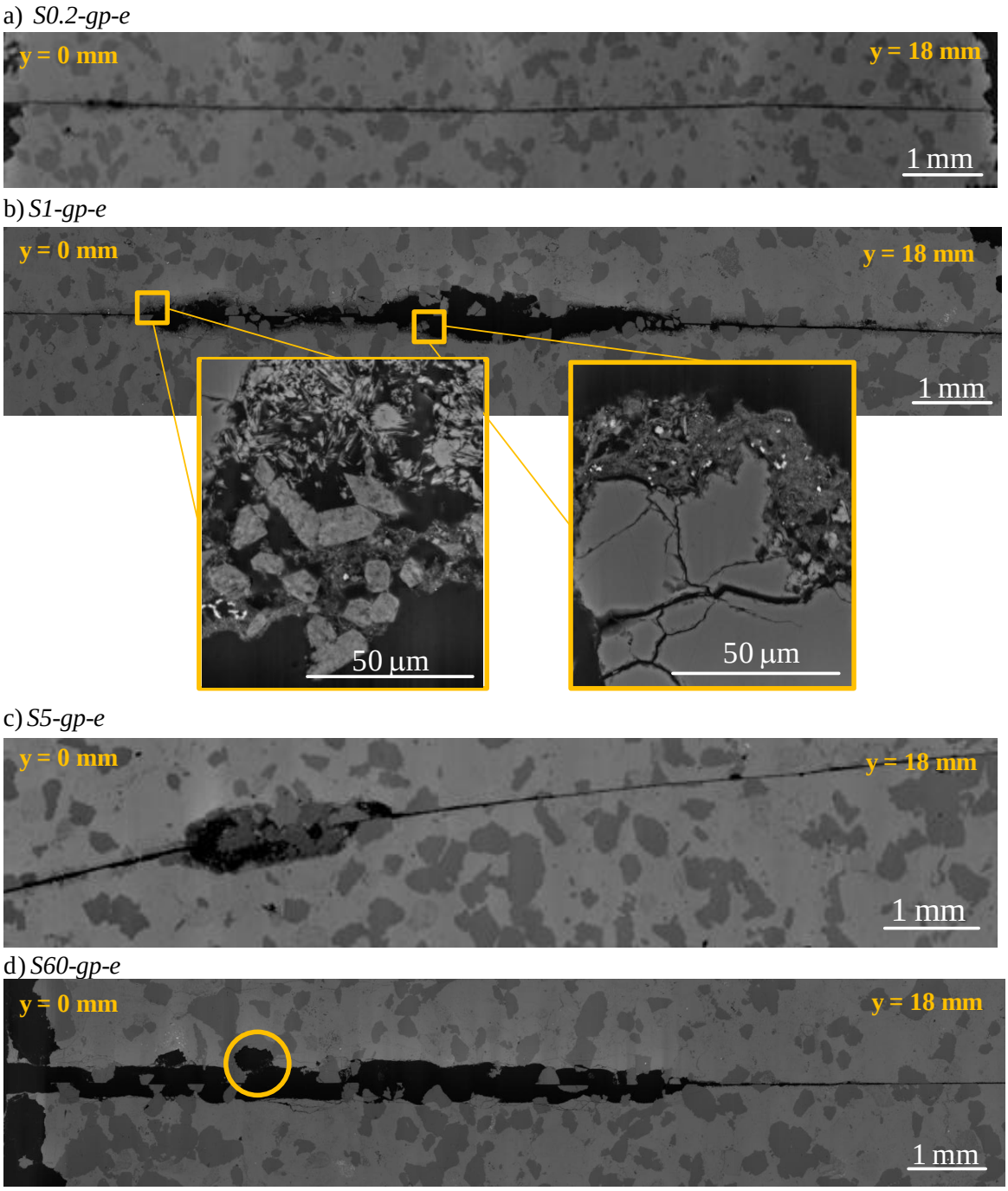

Fig. 4.10 *SEM images of the reacted sandstone fractures in experiments with gp-e input solution at (a) Q = 0.2 mL/h (S0.2-gp-e), (b) Q = 1 mL/h (S1-gp-e), (c) Q = 5 mL/h (S5-gp-e) and (d) Q = 60 mL/h (S60-gp-e). Close-up images in (b) show precipitated gypsum (left) and precipitated unidentified aluminosilicate (right). The y values indicate the distances from the inlet (y = 0) of the fracture along the flow direction (y). Yellow circle in (d) indicates a possible site of a grain detachment.*

Fig. 4.12 depicts the fracture-length profiles from XCMT data that show distinct evolution of the dissolution processes along the sandstone fractures (detailed explanation of the figure legend is given in the previous section (*Section 4.2.4.1*)). Due to a more uniform

dissolution in the sandstone samples than that observed in the limestone ones, black and orange profiles coincided in most of the experiments (Fig. 4.12b, c, e, h). In fact, lack of coincidence was observed where a localized dissolution (*e.g.*, wormhole) developed (Fig. 4.12d, f).

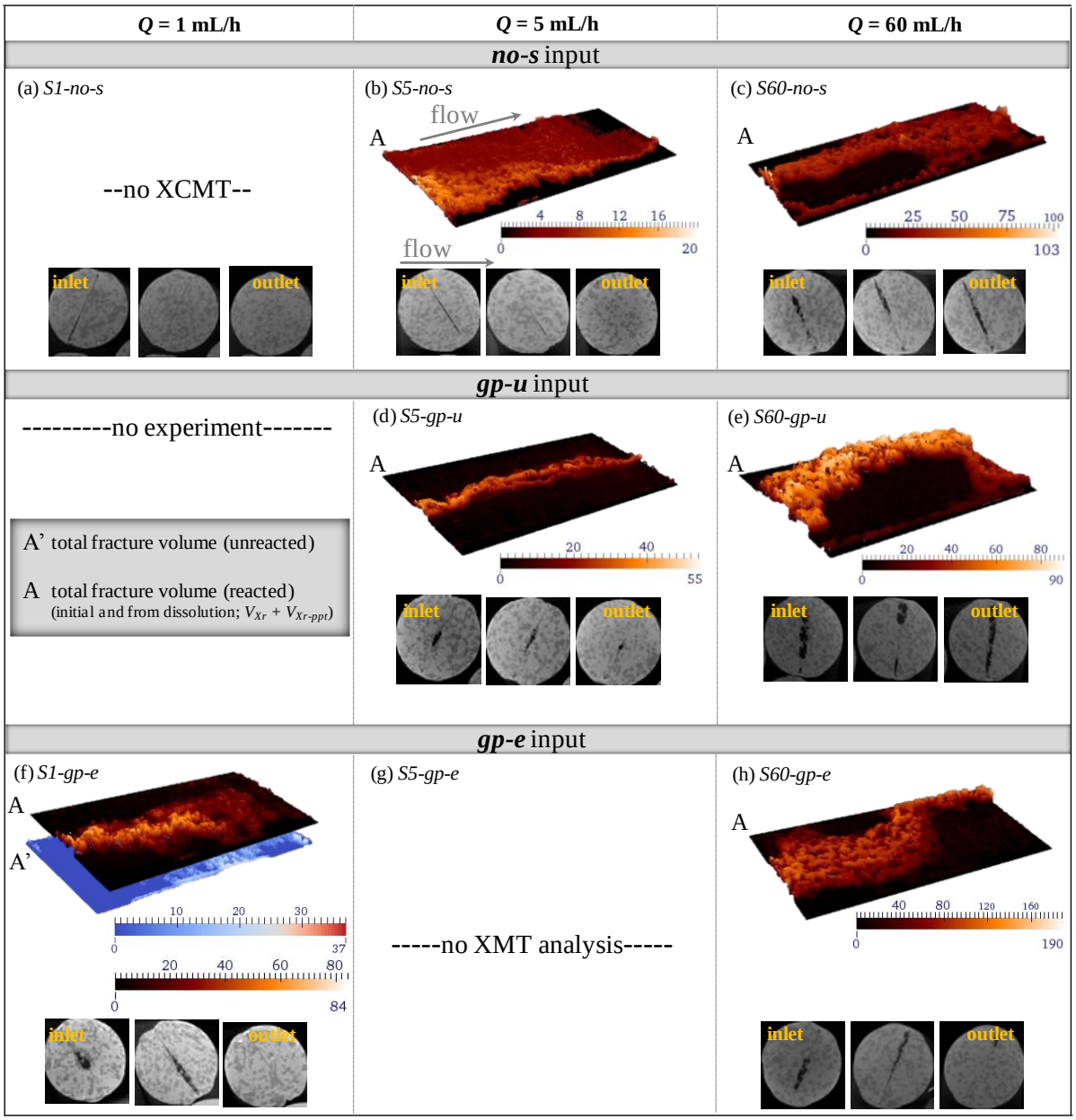

Fig. 4.11 *XCMT results. Total volume of reacted (A) and unreacted (A') fractures in sandstone experiments with no-s solution at (b) Q = 5 mL/h and (c) Q = 60 mL/h, with gp-u solution at (d) Q = 5 mL/h and (e) Q = 60 mL/h and with gp-e solution at (f) Q = 1 mL/h and (h) Q = 60 mL/h. XCMT was not performed in experiment S1-no-s and XMT analysis was not carried out in experiment S5-gp-e. Color scale bars are in pixels (1 pixel = 14 μm). Black and white sections (perpendicular to flow) show the fracture morphology with associated dissolution patterns from the inlet (left) to the outlet (right) of the cores.*

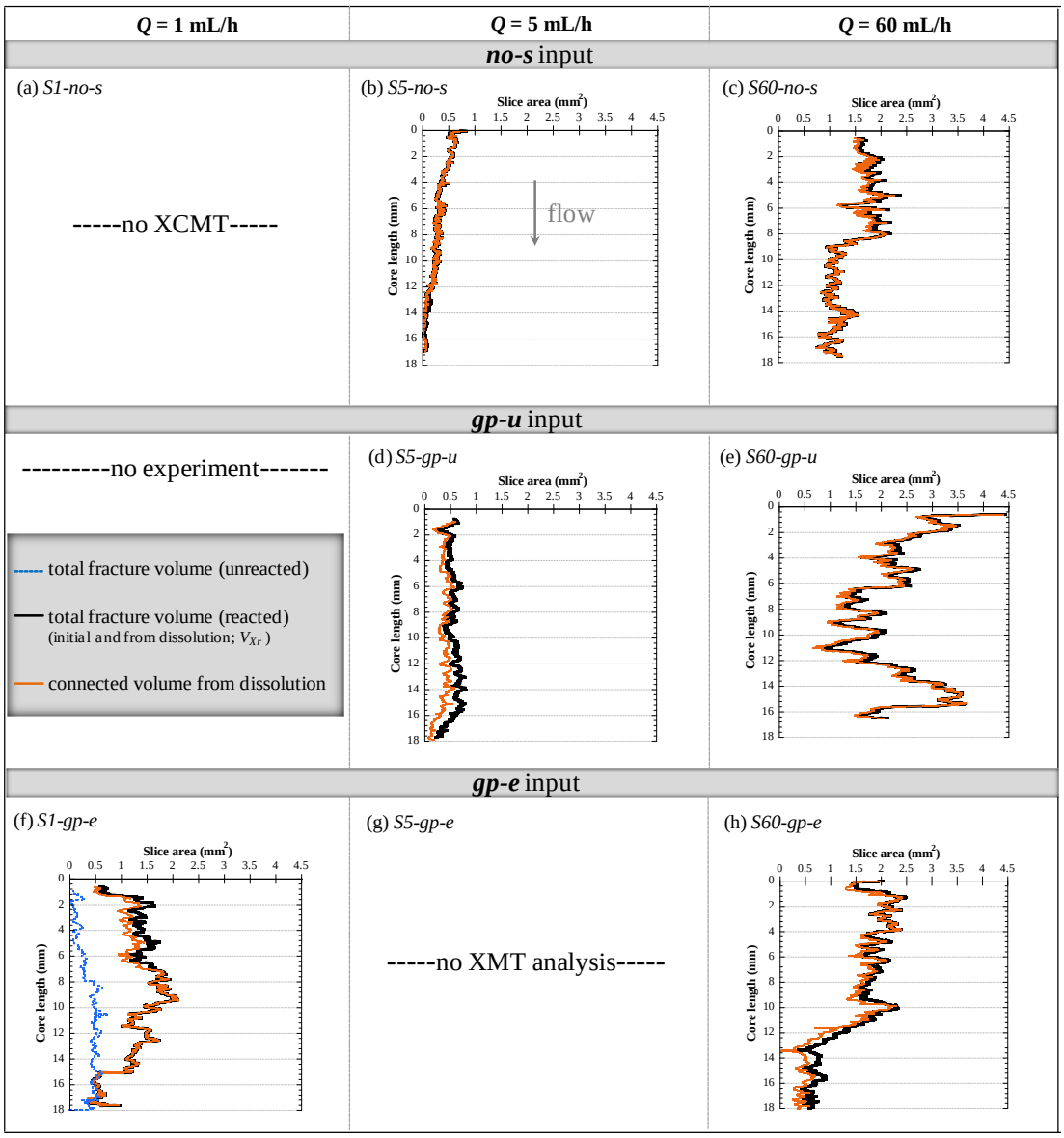

Fig. 4.12 *Fracture-length profiles that show the volume of unreacted (blue lines) and reacted (black lines) fractures and the largest connected volume from dissolution (orange lines) in sandstone experiments with no-s solution at (b) Q = 5 mL/h and (c) Q = 60 mL/h, experiments with gp-u solution at (d) Q = 5 mL/h, (e) Q = 60 mL/h and experiments with gp-e solution at (f) Q = 1 mL/h and (h) Q = 60 mL/h.*

4.3 Discussion

4.3.1 Fracture volume calculated from mass balance and XCMT

Once the percolation experiments were finished, five limestone and six sandstone fractured samples were characterized by XCMT to determine the geometry of the reacted fracture (Table 4.3; V_{Xr}). The changes in fracture volume obtained from aqueous chemistry

(ΔV_{ch}) and from XCMT data (ΔV_{Xr}) were compared at the end of the experiment (Table 4.3; $t = t_f$; comparison of ΔV_{ch} and ΔV_{Xr}).

From aqueous chemistry, the volume of dissolved calcite $V_{Cal-diss}$ and precipitated gypsum V_{Gp-ppt} and the variation of fracture volume ΔV_{ch} at the end of the experiment (t_f) were calculated according to Eqs. (2.2) and (2.7) and the mass balance equations (Eqs. (2.3) and (2.5); Table 4.3). The loss of mass calculated from the aqueous chemistry (ΔM_{calc}) was in very good agreement with the measured loss of mass (ΔM_{meas}) giving high reliability of the chemical analyses (Table 4.3).

Information about the total volume of fracture after reaction V_{Xr} (void space including the initial fracture volume and the dissolution-induced volume) and the volume of gypsum precipitated in the fracture V_{Xr-ppt} was obtained by processing the X-ray microtomography data sets. V_{Xr-ppt} was always an amount of gypsum precipitated inside the fracture or in a wormhole. The change in fracture volume ΔV_{Xr} shown in Table 4.3 was determined as

$$\Delta V_{Xr}(t_f) = V_{Xr}(t_f) - V_{Xr}(t_0) \quad (4.1)$$

where the total volume of the unreacted fracture $V_{Xr}(t_0)$ was obtained using XCMT analysis only for three experiments (Table 4.2; $V_{Xr}(t_0)$). The unreacted fracture volume obtained from XCMT was ≈ 7 times larger than that from SEM. Hence, this factor of ≈ 7 was used to calculate $V_{Xr}(t_0)$ for the rest of experiments, from which XCMT analysis of the unreacted fracture was not performed (Table 4.2; $V_{Xr}(t_0)$ values in grey background).

Comparison between the variation in fracture volume obtained from aqueous chemistry ($\Delta V_{ch}(t_f)$) and that obtained from XCMT analysis ($\Delta V_{Xr}(t_f)$) showed very good agreement in six experiments in which $\Delta V_{Xr}(t_f)/\Delta V_{ch}(t_f)$ ranged from 0.92 to 1.05 (Table 4.3). Agreement was poorer in the other four experiments (Table 4.3; $0.72 \leq \Delta V_{Xr}(t_f)/\Delta V_{ch}(t_f) \leq 0.86$). Problems in the XCMT segmentation process could be the cause of the observed discrepancies in the latter experiments. Void space was probably interpreted to be epoxy resin due to the large pixel size (14 μm) and the high background noise from the data. As a result, in the experiments where dissolution patterns developed in contact with the epoxy resin area, discrepancy increased. In most of the experiments where a wormhole developed in a central position (*e.g.*, Figs. 4.7a, d and 4.11f), a very small discrepancy was observed.

Table 4.3 *Measured mass, measured and calculated loss of mass and variation in fracture volume determined from aqueous chemistry and XCMT at the end of the experimental runs ($t=t_f$).*

$t = t_f$				Aqueous chemistry				XCMT			Comparison
Experiment label	t_f (h)	M_{meas} (g)	ΔM_{meas} (g)	$V_{Cal-diss}$ (mm^3)	V_{Gp-ppt} (mm^3)	ΔV_{ch} (mm^3)	ΔM_{calc} (g)	V_{Xr} (mm^3)	V_{Xr-ppt} (mm^3)	ΔV_{Xr} (mm^3)	$\Delta V_{Xr}/\Delta V_{ch}$
LIMESTONE											
L1-no-s	30.75	2.957	-0.039	14.92	-	**14.92**	-0.040	22.60	-	**15.13**	1.01
L60-no-s	4.70	2.945	-0.069	23.50	-	**23.50**	-0.064	21.73	-	**16.89**	0.72
L0.2-gp-e	45.72	2.809	-	2.37	0.53	**1.84**	-0.005	-	-	-	-
L1-gp-e	71.91	2.690	-0.049	21.53	5.47	**16.06**	-0.046	21.84	1.91	**13.78**	0.86
L5-gp-e	18.50	-	-	23.76	8.34	**15.42**	-0.045	21.77	2.87	**16.06**	1.04
L60-gp-e	4.51	2.648	-0.042	22.11	6.73	**15.38**	-0.044	19.44	not detected	**11.50**	0.75
SANDSTONE											
S1-no-s	6.31	2.970	-0.004	1.76	-	**1.76**	-0.005	-	-	-	-
S5-no-s	1.38	2.892	-0.004	-	-	-	-	4.71	-	**1.86**	-
S60-no-s	1.32	2.797	-0.034	12.45	-	**12.45**	-0.034	23.59	-	**13.07**	1.05
S5-gp-u	5.58	2.838	-0.014	6.72	0.50	**6.23**	-0.017	10.03	not detected	**5.70**	0.92
S60-gp-u	5.59	2.564	-0.121	45.76	2.97	**42.79**	-0.117	48.2	not detected	**40.57**	0.95
S0.2-gp-e	102.20	-	-	7.34	0.65	**6.69**	-0.018	-	-	-	-
S1-gp-e	37.34	2.825	-0.040	14.05	0.16	**13.89**	-0.038	21.88	not detected	**14.44**	1.04
S5-gp-e	17.66	-	-	14.24	4.66	**9.58**	-0.028	-	-	-	-
S60-gp-e	4.03	-	-	27.42	1.28	**26.14**	-0.071	32.01	not detected	**20.63**	0.79

t_f = experimental time.
M_{meas} = measured mass of fractured core (weighted).
ΔM_{meas} and ΔM_{calc} = measured and calculated (from aqueous chemistry) loss of mass.
$V_{Cal-diss}$ and V_{Gp-ppt} = volume of dissolved calcite and precipitated gypsum (aqueous chemistry).
V_{Xr} and V_{Xr-ppt} = volume of fracture (void space) and volume of precipitated gypsum (XCMT).
ΔV_{ch} and ΔV_{Xr} = variation of fracture volume from aqueous chemistry (ch) and XCMT (Xr).
Initial values used to calculate ΔM_{meas} and ΔV_{Xr} are given in Table 4.2.
The propagated error of ΔV_{ch} is 10-12 %.

Regarding the volume of precipitated gypsum in the limestone experiments, volume calculated from aqueous chemistry $V_{Gp-ppt}(t_f)$ was greater than that obtained from XCMT analysis $V_{Xr-ppt}(t_f)$ in all experiments (Table 4.3; $V_{Gp-ppt}(t_f)/V_{Xr-ppt}(t_f)$ = 2.9 in experiments *L1-gp-e* and *L5-gp-e*). The largest difference between measurements was obtained in the experiment with the fastest flow rate (*L60-gp-e*), where precipitation of gypsum was not observed by XCMT (Table 4.3; $V_{Xr-ppt}(t_f)$ = not observed) in contrast to the volume of precipitated gypsum calculated from aqueous chemistry (Table 4.3; $V_{Gp-ppt}(t_f)$ = 6.73 mm^3). In this experiment, the output Ca concentration was smaller than that obtained in experiments under slower flow rate (Q from 0.2 to 5 mL/h). This fact and the shorter residence time probably induced the precipitation of smaller gypsum crystals, which would be more difficult to identify by XCMT. Moreover, $V_{Gp-ppt}(t_f)$ in experiment *L60-gp-*

e was probably overestimated owing to the high uncertainty in the aqueous chemistry (Fig. 4.1b; ΔS ≈ 0 within the analytical error). In the experiment with the slowest flow rate (Q = 0.2 mL/h) this comparison could not be performed because the XCMT analysis was not carried out. Gypsum was not observed either in the SEM images probably due to the minor calcite dissolution.

In the sandstone experiments, precipitated gypsum was not detected by XCMT. In experiments *S60-gp-u* and *S60-gp-e* with remarkable $V_{Gp-ppt}(t_f)$, precipitation of small gypsum crystals owing to the fast flow rate (Q = 60 mL/h) was likely the cause to impede detection of gypsum by XCMT. In the experiment with the largest $V_{Gp-ppt}(t_f)$ (*S5-gp-e*) this comparison could not be performed because the XCMT analysis was not carried out.

Regardless of the methodology used to calculate changes in fracture volume, it was observed that the final fracture volume was always larger than the initial one even when gypsum precipitated in experiments with sulfate-rich solutions (*gp-u* and *gp-e*).

4.3.2 Influence of flow rate on reaction

The effect of flow rate on the resulting dissolution and precipitation processes was investigated by varying the flow rate from 1 to 60 mL/h in the experiments with *no-s* and *gp-u* input solutions and from 0.2 to 60 mL/h in the experiments with *gp-e* input solution (Table 4.1).

Mineral dissolution is limited by reaction rates in the fracture surfaces and solute transport (advection vs. diffusion) within the fracture. The Damköhler (Da) and Péclet (Pe) numbers parameterize the relative magnitude of these processes. In the formulation that we use, Pe compares the magnitudes of the advective solute flux along the fracture with diffusion from the fracture surface, and Da compares mineral reaction rates with advective flux along the fracture. The Pe number is given by $Pe = (va)/D_m$, where v is the mean fluid velocity in m/s defined as $v = Q/(da)$, a is the mean aperture of the fracture in m, D_m is the molecular diffusion coefficient of the reactants in m^2/s, Q is the volumetric flow rate in m^3/s and d is the width of the fracture in m. The molecular diffusion coefficient at 60 ºC (D_m = 5.36. × 10^{-9} m^2/s) was calculated using Arrenhius equation and the molecular diffusion coefficient in water assumed for all species at 25 ºC ($D_0 \approx 10^{-9}$ m^2/s).

To assess the flow rate effect on calcite dissolution, experiments with similar calcite dissolution rate ($R_{Cal} = A_{Cal} k_r a_{H^+} (1 - \Omega)^3$; Xu et al., 2012) must be compared. The initial calcite dissolution rate at the inlet of all fractures could be considered identical because the reactive surface area A_{Cal} (same geometry), the dissolution rate constant k_r (same *T*, *P*), the proton activity a_{H^+} (same pH) and the saturation state Ω (similar input solutions) were almost the same at this initial point (y = 0 mm and $t = t_0$). Once the injected solution reacts with the fracture surface (calcite) under different flow rates, the dissolution rate parameters (A_{Cal}, k_r, a_{H^+} and Ω) will be differently affected with time and distance.

Along the fractures, *P* and *T* were constant and changes in pH were very similar in all experiments (average input pH = 3.23 ± 0.02; average output pH = 3.91 ± 0.20), yielding no variation in k_r and very similar variation in a_{H^+}. Pokrovsky et al. (2009) demonstrated that R_{Cal} was basically not affected by pCO_2 directly (only through the a_{H^+} term). Additionally, saturation state should not noticeably change R_{Cal} between experiments because all output solutions were undersaturated with respect to calcite ($SI_{Cal} \approx$ -2.4 and $\Omega = 4 \times 10^{-3}$ for experiments at Q = 60 mL/h and $SI_{Cal} \approx$ -1.6 and $\Omega = 2.5 \times 10^{-2}$ for experiments at Q = 0.2, 1 and 5 mL/h) and considered to be far from equilibrium (SI_{Cal} < -1.5; Cubillas et al., 2005; Xu et al., 2012). Hence, differences in R_{Cal} between experiments at different flow rates were probably not caused by the small differences in Ω.

As for the reactive surface area A_{Cal} term, it should be similar in all experiments. However, as a consequence of the coupled chemical reactions and transport of elements through the fracture, different dissolution patterns (homogeneous vs. heterogeneous/localized dissolution) may occur, yielding a noticeable variation in the accessible area of mineral that can react with the solution along the fracture. Consequently, differences in the amount of Ca obtained from dissolution at the outlet of the fracture (net reaction rate) between experiments were probably related to changes in the reacted area. At this large scale, Luhmann et al. (2014) and Luquot and Gouze (2009) measured a decrease in *A* during wormhole formation. In addition, at the micrometer scale the flow rate also affects *A*, favoring an *A* increase for slow flow rates (microporosity development; *e.g.*, Fig. 4.6b and c) and an *A* decrease for fast flow rates (surface smoothing; *e.g.*, Fig. 4.6d). Similar observations were reported by Deng et al., (2013), Luquot et al. (2014) and Noiriel et al. (2009). These authors characterized microporosity formation during limestone dissolution for several flow-through experiments. Noiriel et al. (2009) proposed the so-called sugar-lump model that reproduces the

experimental results (formation of microporosity) by a dissolution mechanism that induces the formation of small calcite particles with larger reactive surface area.

To calculate the Damköhler number ($Da = R_{fe}/v$), a velocity for calcite dissolution far from equilibrium in m/s ($R_{fe} = k_r a_{H^+} v_m$) is used. This type of rate law (linear dependence on a_{H^+}) applies to calcite dissolution under acidic conditions (Atanassova et al., 2013; Palandri and Kharaka, 2004; Pokrovsky et al., 2009). Experimental studies have reported that below pH 5.5, the calcite dissolution rate is pH-dependent and limited by mass transfer processes (*e.g.*, Plummer et al., 1978; Sjöberg and Rickard, 1984). Therefore, calcite dissolution rate should increase with fluid velocity because the mass transfer of reactants and products is enhanced by the local fluid velocity near the mineral surface. This trend has been observed by several authors based on discontinuities in the evolution of the output solution concentration due to changes in the flow rate regime (Elkhoury et al., 2013; Noiriel et al., 2007). Noiriel et al. (2007) showed that the chemical flux of Ca^{2+} in mol/s increased with increasing flow rate. In this study, the calculated volumes of dissolved calcite per hour $V_{Cal-diss}/t_f$ (mm^3/h) also increased with increasing flow rate (Table 4.4; *e.g.*, from 0.05 to 4.90 mm^3/h in limestone experiments and from 0.07 to 6.80 mm^3/h in sandstone experiments by increasing Q from 0.2 to 60 mL/h with *gp-e* solution). Additionally, the volume of dissolved calcite per injected volume $V_{Cal-diss}/V_{inj}$ (mm^3/mL) was calculated and showed the opposite tendency: *e.g.*, $V_{Cal-diss}/V_{inj}$ decreased by a factor of ≈ 3.2 with increasing the flow rate from 0.2 (Pe = 1) to 60 mL/h (Pe = 346) in both limestone and sandstone experiments with *gp-e* (Table 4.4). It was probably caused by the shorter residence time in experiments under faster flow rate.

Note that at Q = 0.2 mL/h, $V_{Cal-diss}/V_{inj}$ was lower than expected in both limestone and sandstone experiments. The explanation for this was unclear as the output solution was far from equilibrium and there was no evidence of the existence of more diffusive zones that limited the overall dissolution process and retarded the exit of the reaction products.

To compare experiments performed with the same rock and flow rate, the dissolution rates were calculated at the same experimental time (experiments with (*) in Table 4.4), in particular at the shortest experimental time t_c. It was expected to obtain similar values of $V_{Cal-diss}/t_c$ and $V_{Cal-diss}/V_{inj}(t_c)$ in experiments under the same flow rate and similar evolution of fracture geometry (equivalent reacted area) (Table 4.4). This was evidenced, for

instance, in limestone experiments at Q = 60 mL/h (wormhole formation: *L60-no-s* and *L60-gp-e*) and in sandstone experiments at Q = 5 mL/h (wormhole formation: *S5-gp-u* and *S5-gp-e**).

Table 4.4 *Péclet (Pe) and Damköhler (Da) numbers and net reaction rates expressed as volume of dissolved calcite, precipitated gypsum and variation in fracture volume per time and injected volume.*

				Rate values calculated at t_f							
Exp. label	***Q*** (mL/h)	***Pe***	***Da***	**t_f** (h)	$V_{Cal\text{-}diss}/t_f$	$V_{Gp\text{-}ppt}/t_f$ (mm^3/h)	$\Delta V_{ch}/t_f$	**V_{inj} (t_f)** (mL)	$V_{Cal\text{-}diss}/V_{inj}$ (t_f)	$V_{Gp\text{-}ppt}/V_{inj}$ (t_f) (mm^3/mL)	$\Delta V_{ch}/V_{inj}$ (t_f)
L0.2-gp-	0.2	1	1.9E-05	46	0.05	0.01	0.04	9	0.26	0.06	0.20
L1-no-s	1	6	3.8E-06	31	0.49	-	0.49	31	0.49	-	0.49
*L1-gp-e**				72	0.30	0.08	0.22	72	0.30	0.08	0.22
L5-gp-e	5	29	7.6E-07	19	1.28	0.45	0.83	93	0.26	0.09	0.17
L60-no-s	60	346	6.3E-08	5	5.00	-	5.00	282	0.08	-	0.08
L60-gp-e				5	4.90	1.49	3.41	271	0.08	0.02	0.06
S0.2-gp-	0.2	1	1.9E-05	102	0.07	0.01	0.07	20	0.36	0.03	0.33
S1-no-s	1	6	3.8E-06	6	0.28	-	0.28	6	0.28	-	0.28
*S1-gp-e**				37	0.38	0.004	0.37	37	0.38	0.004	0.37
S5-no-s	5	29	7.6E-07	1	-	-	-	7	-	-	-
S5-gp-u				6	1.20	0.09	1.12	28	0.24	0.02	0.22
*S5-gp-e**				18	0.81	0.26	0.54	88	0.16	0.05	0.11
S60-no-s	60	346	6.3E-08	1	9.43	-	9.43	79	0.16	-	0.16
S60-gp-				6	8.19	0.53	7.66	335	0.14	0.01	0.13
S60-gp-e				4	6.80	0.32	6.49	242	0.11	0.01	0.11
				Rate values calculated at t_c							
				t_c (h)	$V_{Cal\text{-}diss}/t_c$	$V_{Gp\text{-}ppt}/t_c$ (mm^3/h)	$\Delta V_{ch}/t_c$	**V_{inj} (t_c)** (mL)	$V_{Cal\text{-}diss}/V_{inj}$ (t_c)	$V_{Gp\text{-}ppt}/V_{inj}$ (t_c) (mm^3/mL)	$\Delta V_{ch}/V_{inj}$ (t_c)
*L1-gp-e**				31	0.30	0.08	0.22	0	0.30	0.08	0.22
*S1-gp-e**				6	0.27	0.003	0.26	0	0.27	0.003	0.26
*S5-gp-e**				6	1.26	0.10	1.16	0	0.25	0.02	0.23

Pe and *Da* = Péclet and Damkhöler numbers.
t_f = total experimental time; t_c = time of the shortest experiment in those run at the same rock and flow rate (see text in *Section 4.3.2*).
* indicates experiments where t_c was calculated.
V_{inj} = injected volume.

However, in the two limestone experiments run at Q = 1 mL/h, $V_{Cal-diss}/t_c$ and $V_{Cal-diss}/V_{inj}(t_c)$ were larger in the experiment using *no-s* input solution (*L1-no-s* and *L1-gp-e**). The reacted area for the *no-s* experiment was larger because of the formation of channel branching near the outlet (Fig. 4.7a, c). Likewise, $V_{Cal-diss}/t_c$ and $V_{Cal-diss}/V_{inj}(t_c)$ were smaller in the sandstone experiment run at Q = 60 mL/h with *gp-e* owing to a more localized dissolution near the outlet than those for the other two sandstone experiments with nil or lower sulfate content in the input solution (Fig. 4.10 c, e, g). This fact confirmed the effect of the reacted area on the net calcite dissolution rate (including both reaction and transport).

Regarding gypsum precipitation it was also observed that by increasing the flow rate the volume of gypsum precipitated per hour V_{Gp-ppt}/t_f increased. Note, however, that at Q = 60 mL/h (exps. *L60-gp-e*, *S60-gp-u* and *S60-gp-e*), there was a large error in V_{Gp-ppt}/t_f due to the large uncertainty in the measured output S concentrations which were around zero within the error (Fig. 4.1b and Fig. 4.2b). This suggested that precipitation of gypsum was mainly favored at Q = 5 mL/h. Overall, the volume of gypsum precipitated per injected volume V_{Gp-ppt}/V_{inj} decreased by increasing the flow rate, being this attributed to the effect of the smaller residence time under fast flow rate. Gypsum precipitation was observed, as expected, in poorly reactive regions with high diffusion (Fig. 4.6c; y = 1.5 mm), and surprisingly, it also occurred on high reactive areas of the forming wormholes (*e.g.*, Fig. 4.6c; y = 16 mm).

Another factor that could contribute to the different amount of dissolved calcite in the experiments with the same flow rate is the sulfate content in the injected solution, as S inhibits calcite dissolution especially in the presence of calcium and magnesium in solution (Garcia-Rios et al., 2014; Gledhill and Morse, 2006; Sjoberg, 1978). Likewise, the inhibiting role of gypsum coating on the surface of dissolving calcite (passivation) should be taken into account (Offeddu et al., 2014, 2015).

4.3.3 Dissolution patterns

The relative rates of reaction and transport (diffusion and advection) control the nature of the dissolution process within the fracture and the evolution of the fracture geometry (Detwiler and Rajaram, 2007; Kalia and Balakotaiah, 2009). The dimensionless Damköhler and Péclet numbers provide a means of combining the physical and chemical processes that control dissolution regimes in porous and fractured media. Hence, depending on their values, three different dissolution patterns may result: (1) face dissolution (only dissolution at the inlet and no further alteration along the fracture due to reactant consumption), (2) wormhole formation and (3) uniform dissolution along the core (Fredd and Fogler, 1998; Golfier et at., 2002; Szymczak and Ladd, 2009).

As for fractured samples, various theoretical and computational models have been developed to propose easy prediction of dissolution patterns depending on Péclet and Damköhler numbers, which may be defined in different ways. Efforts to test the

computational models of fracture dissolution with quantitative experimental results have had varying success. Verberg and Ladd (2002) simulated the experiment performed by Durham et al. (2001) yielding discrepancies that they attributed to crude models of reaction kinetics and fracture closure. Experiments performed by Detwiler et al. (2003) have been simulated by several authors that have progressively achieved better reproducibility of the experimental data (Detwiler and Rajaram, 2007, Szymczak and Ladd, 2004, Szymczak and Ladd, 2009). The experimental system of Detwiler et al. (2003) consisted of two flat potassium-dihydrogen-phophate (KDP) surfaces with fixed relative positions to eliminate the effect of confining pressure, and a fracture aperture a = 1.26 × 10^{-2} cm. Dissolution was induced by an inflowing solution of KDP at 5% undersaturation (Ω = 0.95). Szymczak and Ladd (2009) successfully reproduced their experimental data using a 3D microscopic numerical method that combines velocity field calculations from an implicit lattice Bolzmann method (Verberg and Ladd, 1999) with a transport solver based on random walk algorithms that incorporates the chemical kinetics at the solid surfaces (Szymczak and Ladd, 2004a). A resulting phase diagram described characteristic dissolution patterns in fractures as a function of Pe and Da.

Elkhoury et al. (2013) performed four percolation experiments with fractured limestone cores using four different flow rates and under reservoir *P*-pCO_2-*T* conditions (*P* = pCO_2 = 140 bar and *T* = 60 ºC). Brine equilibrated with supercritical CO_2 (3 < pH < 4.6) was injected through fractures with a mean aperture a of ≈ 300 μm. The dissolution patterns observed in the fractures were wormhole formations in the two slowest flow rate experiments (Fig. 4.13; V2 with Q = 6 mL/h and Pe = 44 and V1 with Q = 14 mL/h and Pe = 101) and uniform dissolution in the two fastest flow rate experiments (Fig. 4.13; V3 with Q = 600 mL/h and Pe = 4374 and V4 with Q = 1200 mL/h and Pe = 8749). In addition, the authors successfully reproduced their experimental data providing a first opportunity to directly compare simulations to experimental results in more realistic rock samples (reservoir rocks) and settings than those used by Detwiler et al. (2003).

In this study, the Pe and Da values were computed using the formulation described in *Section 4.3.2* (Table 4.4) and R_{fe} = 1.2 × 10^{-8} m/s, which was calculated from the calcite dissolution rate reported by Pokrovsky et al. (2009) under pCO_2 = 30 atm and *T* = 60 ºC (3.98 × 10^{-4} mol/m^2/s) and the calcite molar volume (3.69 × 10^{-5} m^3/mol). Taking into account that the experimental conditions of Elhoury et al. (2013) were similar to those of this study, the same R_{fe} value was used to calculate their Da values. The resulting dissolution patterns were

plotted as a function of Pe and Da^{-1} (Fig. 4.13). In general, by increasing the flow rate (larger Pe and smaller Da) dissolution patterns in both sets of limestone experiments (V1-V4; Elhoury et al. (2013) and *LQ-input label*; this study) and in sandstone experiments (*SQ-input label*; this study) varied from face dissolution to wormhole and uniform dissolution (Fig. 4.13). This tendency was also observed in the Pe-Da^{-1} diagram reported by Szymczak and Ladd (2009).

Before discussing about the observed dissolution patterns it is advanced that the epoxy resin was mechanically stable up to 690 bar, preventing any fracture closure throughout the experiments. Therefore, a possible mechanical effect was neglected to influence fracture evolution. This was evidenced by the similar initial fracture apertures measured during the experiment (a_h) and after the experiment (a_s) (Table 4.2).

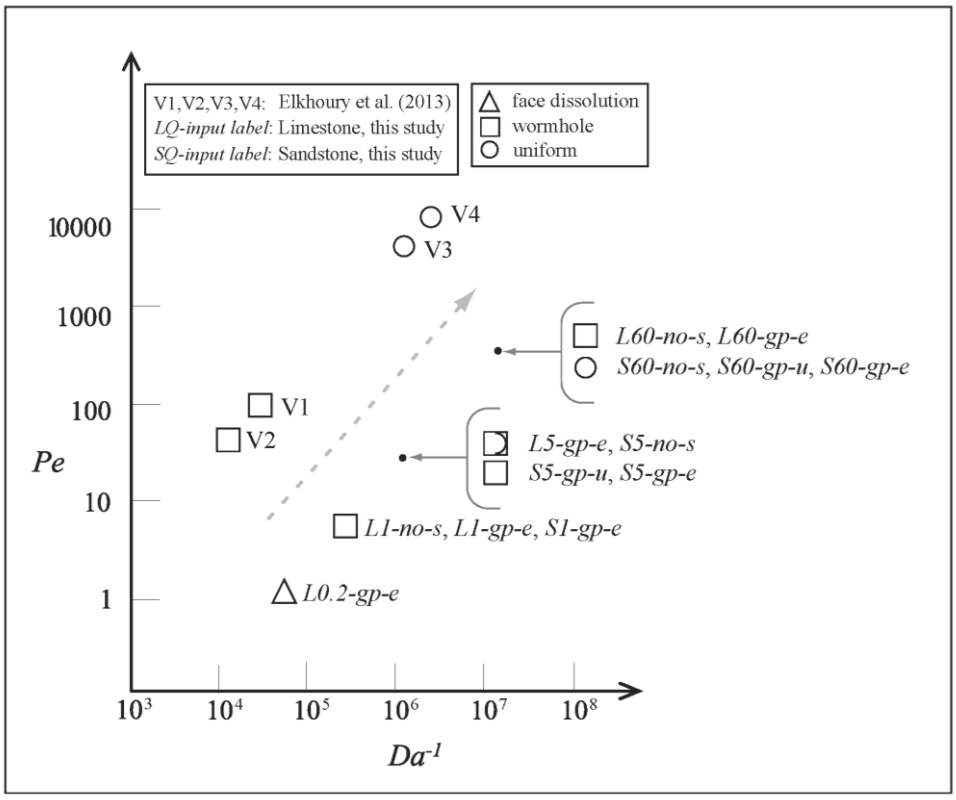

Fig. 4.13 *Dissolution patterns, as a function of Péclet and Damköhler numbers, of limestone and sandstone experiments performed in this study and limestone experiments conducted by Elkhoury et al. (2013). The dashed arrow shows the tendency of dissolution patterns by increasing flow rate. The triangle, square and circle symbols indicate face dissolution, wormhole and uniform dissolution, respectively. The mixed (semicircle-square) symbol denotes transition between patterns (see text).*

Dissolution pattern changed from face dissolution to wormhole by increasing the flow rate from 0.2 mL/h (Fig. 4.6a; *L0.2-gp-e*) to 1 mL/h (Fig. 4.7a, c and Fig. 4.11f; *L1-no-s*, *L1-gp-e* and *S1-gp-e*). Two sandstone experiments were not included in the $Pe\text{-}Da^{-1}$ diagram (*S0.2-gp-e* and *S1-no-s*). Unfortunately, the thin section of experiment *S0.2-gp-e* was produced far from the dissolution front preventing any SEM identification of the dissolution features (Fig. 4.10a) and XCMT was not performed. Similarly, the lack of XCMT and the short duration of experiment *S1-no-s* hindered a full development of any recognizable dissolution feature (Fig. 4.11a).

At 5 mL/h two dissolution structures were observed. A single wormhole originated in two experiments (Fig. 4.11d and Fig. 4.10c; *S5-gp-u* and *S5-gp-e*), as occurred in experiments at 1 mL/h, and a single dominant wormhole with slightly uniform dissolution at the inlet developed in other two experiments (Fig. 4.7d and Fig. 4.11b; *L5-gp-e* and *S5-no-s*). The latter phenomenon suggested an approach of some change in the dissolution pattern (semicircle-square symbol in Fig. 4.13).

Finally, by increasing the flow rate up to 60 mL/h, the expected dissolution pattern would be uniform dissolution, as it occurred in the three sandstone experiments (Fig. 4.11c, e, h; *S60-no-s*, *S60-gp-u* and *S60-gp-e*). However, different dissolution patterns were distinguished in the limestone experiments, probably caused by the presence of important heterogeneities in the fractures. In experiment *L60-gp-e*, slightly uniform dissolution occurred only at the inlet and not in the rest of the fracture, where a dominant wormhole developed. A reason to shift from one pattern to the other could be given by the initial high permeability along the lateral sealing (Fig. 4.7e). In experiment *L60-no-s*, the existence of the lateral heterogeneity at the very inlet perturbed the experiment, causing an exclusive fluid circulation on one side to yield a single dominant wormhole along the fracture (Fig. 4.7b). Hence, dissolution features are clearly influenced by heterogeneities. If significant heterogeneities are initially present, the calculated Pe and Da numbers are insufficient information to predict dissolution patterns (*L60-gp-e* and *L60-no-s*), as Luquot et al. (2014) pointed out for porous media.

Nonetheless, as supported by Elkhoury et al. (2013), dissolution patterns in fractures resemble those in porous media, where dissolution features evolve from face dissolution to wormhole formation when increasing the flow rate (Golfier et al. 2002). The main difference lies in the fact that the presence of fractures forces wormhole formation along the fractures.

However, under high flow rates, preferential flow paths grow more uniformly, compared to the formation of highly ramified wormholes in porous media.

4.3.4 Permeability changes during fracture dissolution

In principle, variation in the output Ca concentration, changes in fracture permeability and the evolved fracture geometry should be closely linked. This fact was readily observed in the 5 mL/h limestone experiment where, after 2 h, the output Ca concentration dropped dramatically as fracture permeability increased sharply (Fig. 4.1a and 4.3a; experiment *L5-gp-e* in red), presumably coinciding with the formation of the primary dissolution channel. Once this single preferential path was created (Fig. 4.7d), fracture permeability could not be measured ($\Delta P < \Delta P_{min}$) and output Ca concentration reached steady state. The other experiments under different flow rates did not show such evident correlation between parameters.

Differences in intrinsic characteristics of the fractures, such as an initially distinct *k*, and development of combined dissolution structures, such as branched wormholes, led to different scenarios where some correlation of these parameters is rather complex. For example, in the 1 mL/h limestone experiment, the sharp increase in fracture permeability occurred after 15 min. However, in this case, the output Ca concentration did not drop, but went on increasing (Fig. 4.1a and 4.3a; experiment *L1-no-s* in green). This behavior is attributed to the evolution of the fracture, as a single wormhole developed while branches formed near the outlet (Fig. 4.7a). This type of fracture geometry (*i.e.*, branching) contributed to an enhancement of the accessible area of mineral (calcite) that can react with the solution along the fracture, yielding a gradual increase in output Ca concentration.

In the 60 mL/h experiments, variation in output Ca concentration and fracture permeability were not apparently linked (Fig. 4.1a and 4.3a; experiment *L60-gp-e* in black and Fig. 4.2a and 4.3b; experiment *S60-gp-e* in black). The increase in fracture permeability was observed with a negligible variation in output Ca concentration due to the very short residence time under this fast flow rate.

A two-stage trend in the evolution of permeability was observed during wormhole formation. After a first period of slow increase in fracture permeability (initial formation of connectivity), a wormhole finally breaks through the outlet of the core, inducing a large and

sudden increase in permeability. Instead, when uniform dissolution originated, a stepped *k* increase was observed in most of the experiments (Fig. 4.3).

Experiments under different flow rates led to situations where the amount and location of dissolution in the fracture varied significantly. Taking into account that local dissolution kinetics in this system is fast relative to diffusion (Pokrovsky et at., 2009; Sjöberg and Rickard, 1984), fracture dissolution will be transport limited (as shown in *Section 4.3.2*) and strongly influenced by *Pe*. At very low *Pe*, diffusion controls dissolution resulting in the growth of large disconnected cavities and a slow increase in *k*, whereas for high Pe, advection dominates reactant transport resulting in dissolution along dominant flow channels and a more rapid increase in *k*. Finally, when fast flow rates eliminate diffusive gradients on the fracture surface, reactant transport is fast relative to dissolution kinetics, and reaction in the fracture tends to a more uniform dissolution (Detwiler et al., 2003; Golfier et al., 2002).

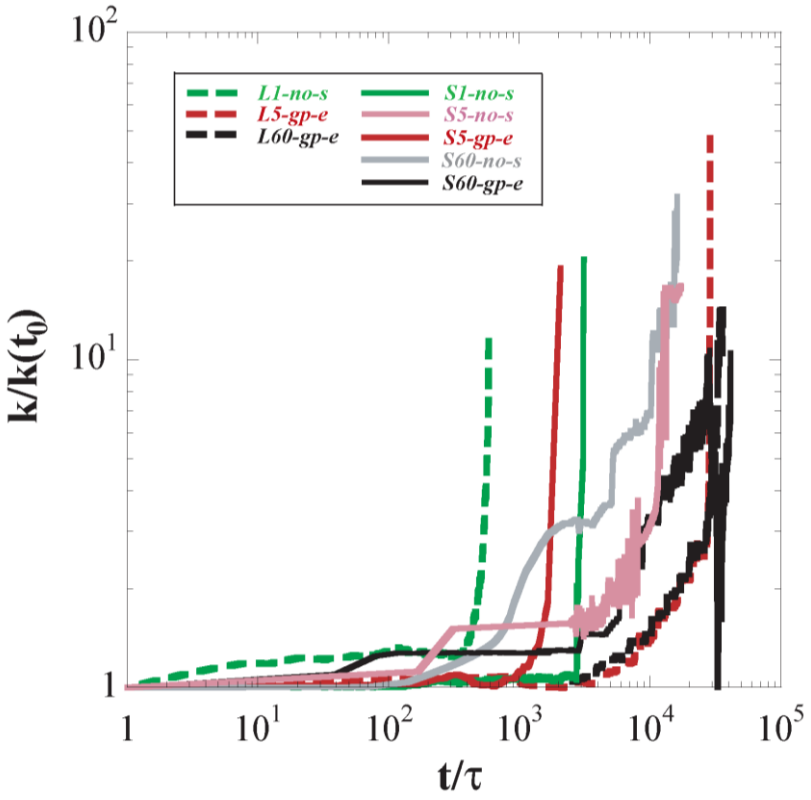

Fig. 4.14 *Variation in fracture permeability vs. the number of equivalent fracture volumes (time/residence time τ) for the limestone (dashed lines) and sandstone (solid lines) experiments. Q = 1 mL/h (green line), Q = 5 mL/h (red and pale red lines) and Q = 60 mL/h (black and grey lines). k(t_0) indicates initial fracture permeability.*

Fig. 4.14 shows variation in fracture permeability versus the number of equivalent fracture volumes for the experiments where k was measurable. Variation in k could not be measured in the two experiments with the slowest flow rate (Table 4.2; Pe = 1; *L0.2-gp-e* and *S0.2-gp-e*) from which, the slowest k increase would be expected, leading to the maximum number of fracture volumes until breakthrough. All experiments under faster flow rate, where k was measurable, showed a remarkable k increase. The k increase was very sharp for experiments where a single dominant wormhole developed (*e.g.*, *L1-no-s*, *S5-gp-e*) and more gradual for the experiments with more uniform dissolution patterns and, in general, under faster flow rates (*e.g.*, *L5-gp-e*, *S60-gp-e*). In addition, in experiments where a single wormhole developed, the significant increase in k occurred after a relatively few fracture volumes. For the 5 and 60 mL/h experiments the number of fracture volumes until breakthrough increased due to formation of more uniform dissolution structures. In this case, dissolution took place over larger fracture surface areas. The trend in the permeability responses showing the typical transition from a single dominant wormhole channel to a more uniform structure was likewise observed in percolation experiments performed in porous media, but more ramified wormhole structures formed (Fredd and Fogler, 1998, Luhmann et al., 2014).

4.4 Summary and conclusions

Injection of CO_2-rich sulfate solutions through fractured limestone and sandstone cores always produced an increase in permeability and fracture volume even when gypsum precipitated in the fractures (experiments using gypsum-equilibrated solutions).

In general, the two methods (aqueous chemistry and XCMT analysis) used to calculate the variation in fracture volume induced by calcite dissolution and gypsum precipitation showed good agreement, yielding differences around 5%. Major discrepancies between them arose when wormholes developed along the lateral sealing and small gypsum crystals precipitated in experiments under fast flow rate. In both cases, the XCMT resolution and image quality limited an accurate quantification of the resulting volumes of fracture and precipitated gypsum.

By increasing the flow rate, under the same pH and far from equilibrium conditions, (1) the volume of dissolved calcite per time increased, confirming that calcite dissolution in

the fracture was transport controlled, and (2) the volume of dissolved calcite per injected volume decreased, likely caused by the smaller residence time in experiments run under faster flow rate. In addition, the formation of more uniform geometries under fast flow rates (*i.e.*, increase of the reacted area) led to an increase in the amount of calcite dissolved. At the micrometer scale, slow flow rates (*e.g.*, Q = 1 and 5 mL/h) led to an increase in reactive surface area caused by an enhancement of microporosity, whereas fast flow rates (*e.g.*, Q = 60 mL/h) tended to form smooth fracture surfaces which did not favor an increase in reactive surface area.

At the same flow rate, the amount of calcite dissolved was larger in some experiments with sulfate-free solution owing to the larger reacted area related to the developed dissolution feature. Another factor contributing to the larger calcite dissolution in sulfate-free experiments than in sulfate-rich ones could be the sulfate inhibitory effect on calcite dissolution, together with gypsum coatings leading to calcite passivation.

In general, dissolution patterns in limestone and sandstone experiments varied from face dissolution to wormhole formation and uniform dissolution by increasing the flow rate (larger Pe and smaller Da), confirming the tendency observed in previous studies (Detwiler et al., 2003; Szymczak and Ladd, 2009). Nonetheless, to predict them, initial surface heterogeneities must be taken into account since they were decisive in the evolution of the dissolving fractures.

Variation in fracture permeability was found to be highly dependent on flow rate and developed dissolution pattern. Thus, permeability increase was very sharp when a single dominant wormhole developed, whereas it was more gradual when uniform dissolution occurred under fast flow rate. The number of fracture volumes to breakthrough increased with flow rate. This phenomenon was attributed to the formation of more uniform dissolution structures, which induced dissolution over larger fracture surface areas.

Chapter 5

Dissolved CO_2 effect on two fractured reservoir rocks: comparison and 2D modeling

5.1 Introduction

This chapter is divided in two parts. In the first one, the geochemical response of two fractured reservoir rocks (limestone and sandstone) to the injection of a CO_2-rich solution under the Hontomín reservoir conditions was compared. The main difference between the limestone and the sandstone is the presence of quartz and microcline grains (≈ 35%) in the latter rock, which affects the evolving geochemical processes and, consequently, could influence the CO_2 storage capacity and injectivity of the reservoir.

In the second part, 2D reactive transport simulations that reproduce the variation in aqueous chemistry and fracture geometry of the experiments were performed to estimate flow and reaction kinetics parameters. Under the experimental conditions, pH could not be measured. The calculated pH (CrunchFlow) increased from 3.3 (input solution) to 4.4 (steady-state output solution).

5.2 The role of silicate minerals on the CO_2 storage capacity and injectivity

The reactivity of two fractured reservoir rocks (limestone composed of 100% calcite and sandstone composed of 65.7% calcite, 27.8% quartz and 6.5% microcline) in contact with a CO_2-rich sulfate solution was compared.

As shown in *Chapter 4*, calcite dissolution was the dominant reaction in both limestone and sandstone experiments, becoming the only process considered to calculate the volumes of dissolved rock. Negligible dissolution of K-feldspar (microcline) and nil dissolution of quartz led to the existence of inert regions in reactive zones of the sandstone experiments. The influence of the inert regions on rock dissolution, mineral precipitation and fracture volume variation was evaluated.

Two sets of experiments with *gp-e* input solution run under flow rates of 0.2, 1, 5 and 60 mL/h were compared (Table 4.1; four limestone experiments: *L0.2-gp-e*, *L1-gp-e*, *L5-gp-e* and *L60-gp-e*; four sandstone experiments: *S0.2-gp-e*, *S1-gp-e*, *S5-gp-e* and *S60-gp-e*).

Overall, the volume of dissolved rock $V_{rock-diss}$ was larger in the sandstone experiments than in the limestone ones (Fig. 5.1a), likely caused by the evolved dissolution pattern. The presence of inert silicate grains in the sandstone experiments favored more extended dissolution structures than the localized ones in the limestone experiments. As a result, a larger area of calcite could interact with the CO_2-rich solution resulting in a larger amount of calcite dissolution. The XCMT images show the difference in dissolution patterns between limestone and sandstone experiments (*e.g.*, comparison of Fig. 4.7c and Fig. 4.11f). Only when Q was 5 mL/h $V_{rock-diss}$ was larger in the limestone experiment. This was related with the zone in which dissolution started: in the fracture (limestone experiment *L5-gp-e*) or in the rock matrix through initial heterogeneities (sandstone experiment *S5-gp-e*). Net rock dissolution was likely favored when started in the fracture.

The volume of gypsum precipitated V_{Gp-ppt} was always larger in the limestone experiments, even if calcite dissolution was smaller (Fig. 5.1b). In the sandstone experiments, dispersion of nuclei for precipitation on the inert surfaces (quartz grains) was likely the cause of less precipitation. This phenomenon was already observed when inert wood chips (Rötting et al., 2008) and glass beads (Offeddu et al., 2015) were added in columns packed with calcite grains to prevent calcite passivation.

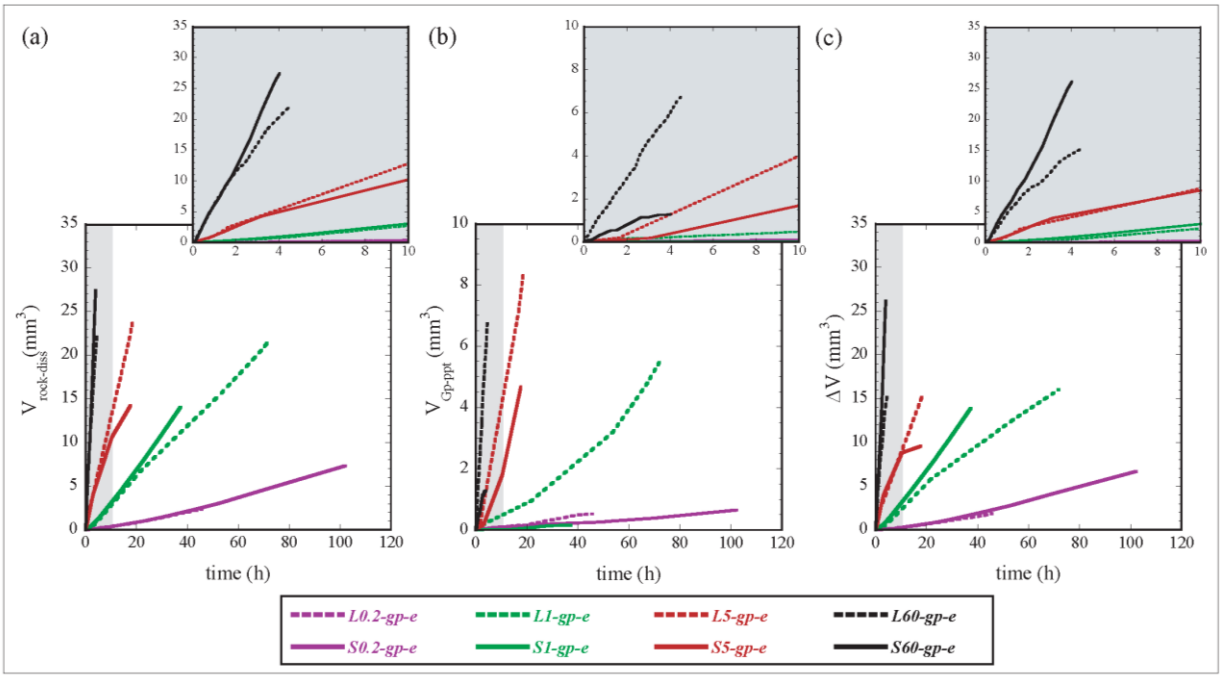

Fig. 5.1 *Experimental variation of volume of dissolved rock $V_{rock-diss}$ (a), volume of precipitated gypsum V_{Gp-ppt} (b) and fracture volume ΔV (c) with time in limestone (dashed lines) and sandstone (solid lines) experiments with gp-e input solution, under Q = 0.2 mL/h (in violet), Q = 1 mL/h (in green), Q = 5 mL/h (in red) and Q = 60 mL/h (in black).*

The resulting $V_{rock-diss}$ and V_{Gp-ppt} always yielded a larger increase in fracture volume ΔV in sandstone experiments (Fig. 5.1c). Hence, it appears that the CO_2 storage capacity would be more favored in a sandstone reservoir than in a limestone one because the increase in porosity is higher and larger extended distribution of created volume ΔV occurs (uniform dissolution).

The different distribution of created volume ΔV between limestone and sandstone experiments was responsible for the different variation in fracture permeability (Fig. 5.2). Limestone dissolution tended to be localized (wormhole), whereas sandstone dissolution tended to be extended (uniform). To illustrate it fracture permeability variation was compared between a limestone experiment where a wormhole developed (*L60-gp-e*; Fig. 5.2a) and a sandstone experiment where uniform dissolution occurred (*S60-gp-e*; Fig. 5.2b). In the limestone experiment, the increase in fracture permeability started with the formation of a localized preferential path (t_1), which continuously enlarged (t_2 and t_3), resulting in a gradual increase in permeability (from t_1 to t_3). In the sandstone experiment, the fracture permeability increase was more complex. In this case, the enlargement of a first preferential path (first permeability increase; t_1) was constrained by the presence of inert grains. The initial path

enhancement stopped as calcite totally dissolved and silicate grains contacted the solution. Thereafter, additional paths developed (t_2), keeping permeability constant until a larger channel originated (t_3 with $a_3 > a_1, a_2$), allowing permeability to increase. This stepped increase in fracture permeability contrasts with the sharper increase observed in limestone experiments.

Given the resulting differences in fracture permeability variation, an advantage of a progressive stepped increase in permeability in the sandstone experiments is that risks associated with changes in the mechanical properties of a reservoir, induced by a sharp permeability increase during CO_2 injection, could be minimized. Moreover, in sandstone experiments, the lower number of fracture volumes necessary to start the permeability increase could facilitate the CO_2 injection and, hence, reduce the energetic storage costs. Another benefit that stems from the more extended distribution of created volume in sandstone experiments is the enhancement of porous connectivity, which favors capillary trapping.

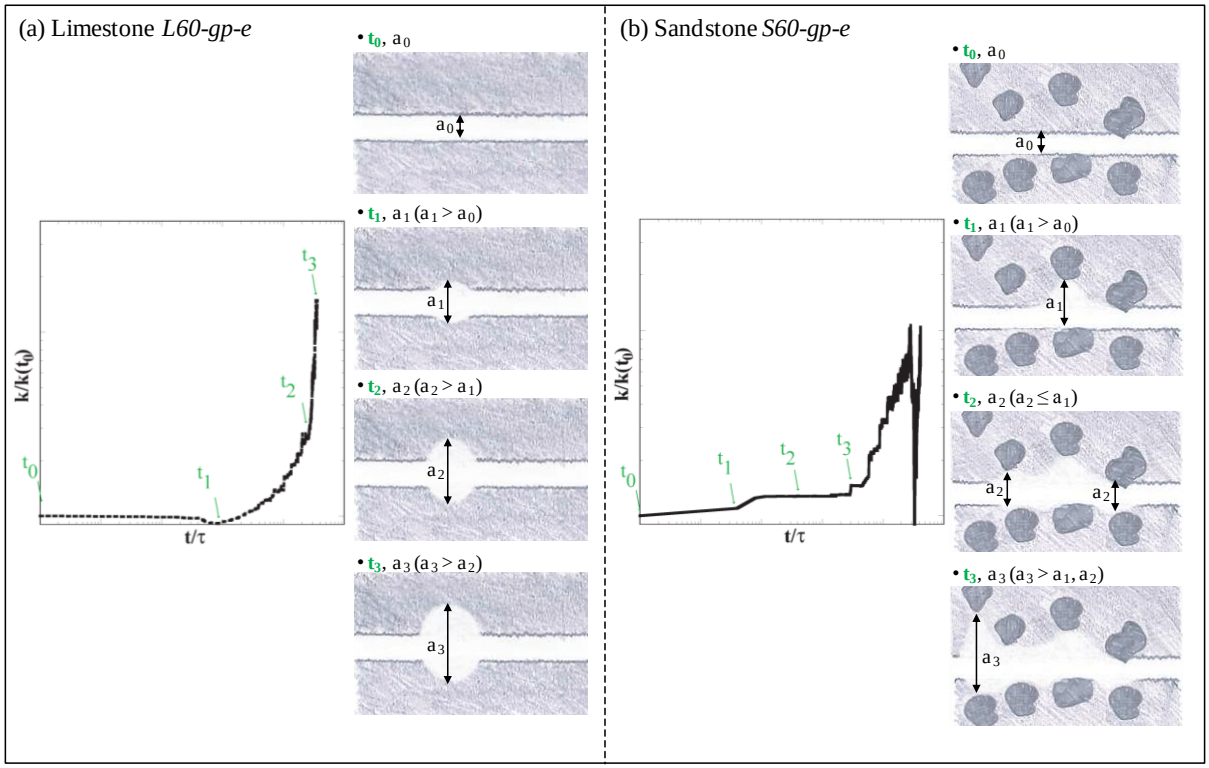

Fig. 5.2 *Variation in fracture permeability as a function of number of fracture volumes (t/τ) and the associated distribution of created volume in the experiments L60-gp-e (a) and S60-gp-e (b). $k(t_0)$ indicates initial fracture permeability.*

5.3 (2D) Reactive transport modeling

Simulations of experiment *L0.2-gp-e* (face dissolution), *L1-gp-e* (wormhole) and *S60-no-s* (uniform dissolution) are shown in this section. In addition, discussion on the fitting parameters used to adjust the model to the experimental data (measured Ca and S concentrations and porosity variation) is also provided.

Rectangular coordinates were used to model experiments which developed face and uniform dissolution patterns (*L0.2-gp-e* and *S60-no-s*), whereas rectangular and cylindrical coordinates were used in the experiment where a wormhole developed (*L1-gp-e*). When cylindrical coordinates were used, it was assumed that the initial fracture was already cylindrical (*i.e.*, a very small wormhole).

5.3.1 Face dissolution

A model with rectangular coordinates and flow update was used to simulate the experimental data of experiment *L0.2-gp-e* (face dissolution). A good match between the experimental and simulated Ca and S concentrations versus time was achieved by considering an initial D_e value of 3.0×10^{-12} m^2/s in the rock matrix and adjusting the initial calcite and gypsum reactive surface areas (A_{Cal} = 250 m^2_m/m^3_{bulk}; A_{Gp} = 10 m^2_m/m^3_{bulk}) (SIM_A in Fig. 5.3a, b). Nonetheless, the simulated variation in porosity (Fig. 5.3c) did not match the actual variation measured by SEM (Fig. 4.6a). Considering half of the fracture core (due to symmetry), the SEM image shows 100% porosity up to 12 μm in the *x* direction (normal distance to fracture) at the inlet of the fracture (colored area in Fig. 5.3c, d), and no porosity increase at the outlet. The initial D_e value was calculated using Eq. (2.21) with D_0 and n values equal to 10^{-9} m^2/s and 2.5, respectively. These values are common values reported in literature (see *Section 2.2.2.3*).

A reasonable match of the variation of both the Ca and S concentrations with time (SIM_B in Fig. 5.3a, b) and porosity with distance normal to fracture (Fig. 5.3d) was only obtained by reducing the initially estimated D_e value to 6.0×10^{-14} m^2/s and adjusting the values of A_{Cal} and A_{Gp} (2000 and 100 m^2_m/m^3_{bulk}, respectively). Model parameters used in this simulation are given in Table A.6, *Appendix A*. Experimental porosity variation was plausibly reproduced by the model: at the inlet of the core the calculated porosity was higher than 85% over the first 11.3 μm in the *x* direction (the measured porosity was 100% up to 12 μm; Fig

4.6a, y = 0 mm). At the outlet, the calculated porosity was slightly higher than the measured one (20% instead of 5%; Fig 4.6a, y = 20 mm). The changes in mineral content caused a noticeable increase in porosity at the inlet of the fracture and almost no increase afterwards (Fig. 5.3d). The different increase in porosity between inlet and outlet of the fracture (markedly larger at the inlet) compared well with the observed dissolution pattern (face dissolution).

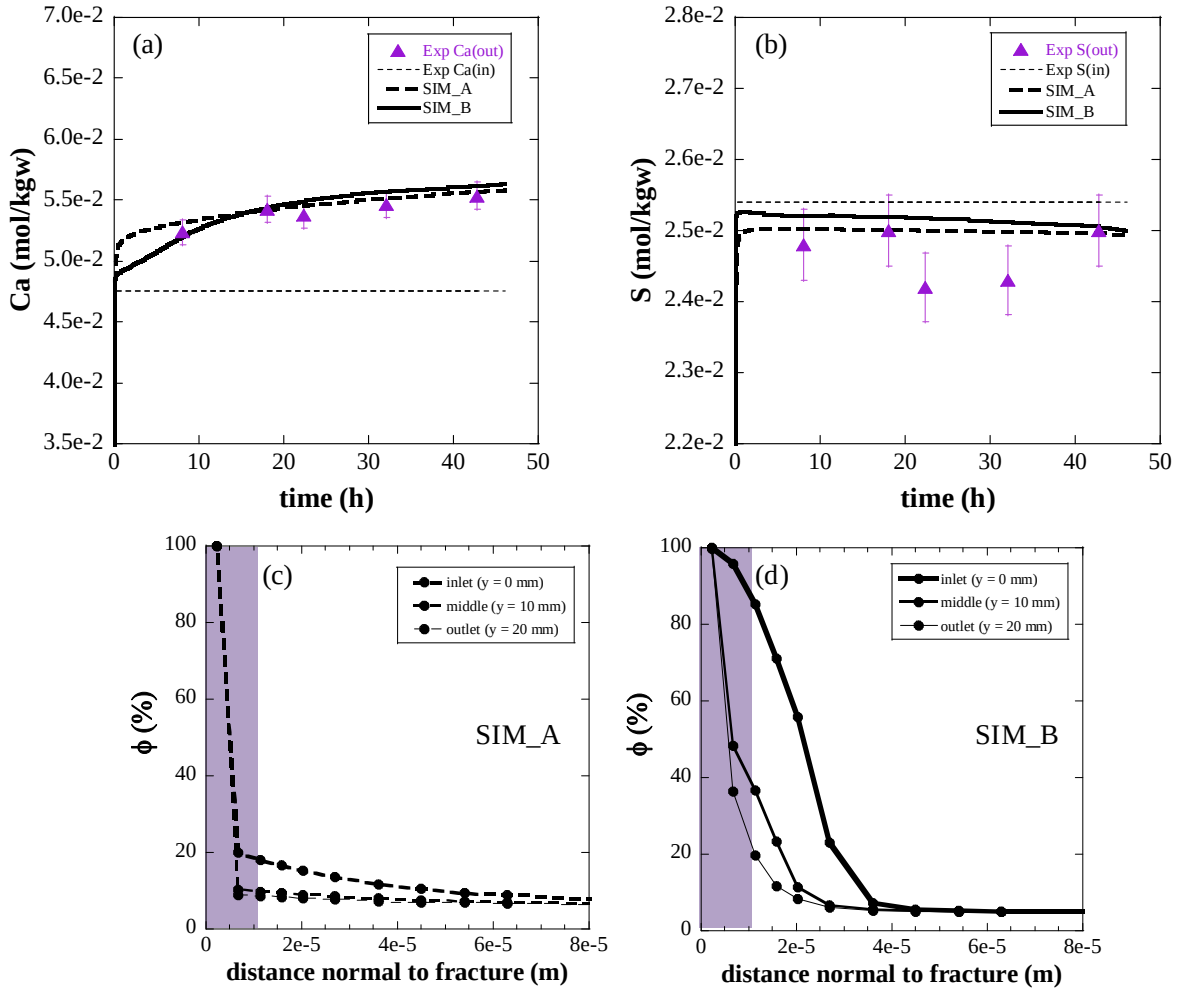

Fig. 5.3 *Experiment L0.2-gp-e (face dissolution); simulations with rectangular coordinates and flow update: (a,b) Variation in the experimental and simulated Ca and S concentration versus time and (c,d) simulated porosity variation with distance normal to fracture. Colored areas in (c,d) indicate the zone with 100% porosity measured by SEM at the inlet of the fractured core.*

These changes in porosity and the associated changes in permeability have translated into a slight change in Darcy velocity in the fracture. At the end of the experiment, solution

still flowed preferentially along the fracture (V_y; Fig. 5.4b), with a negligible deviation towards the rock matrix (V_x; Fig. 5.4a).

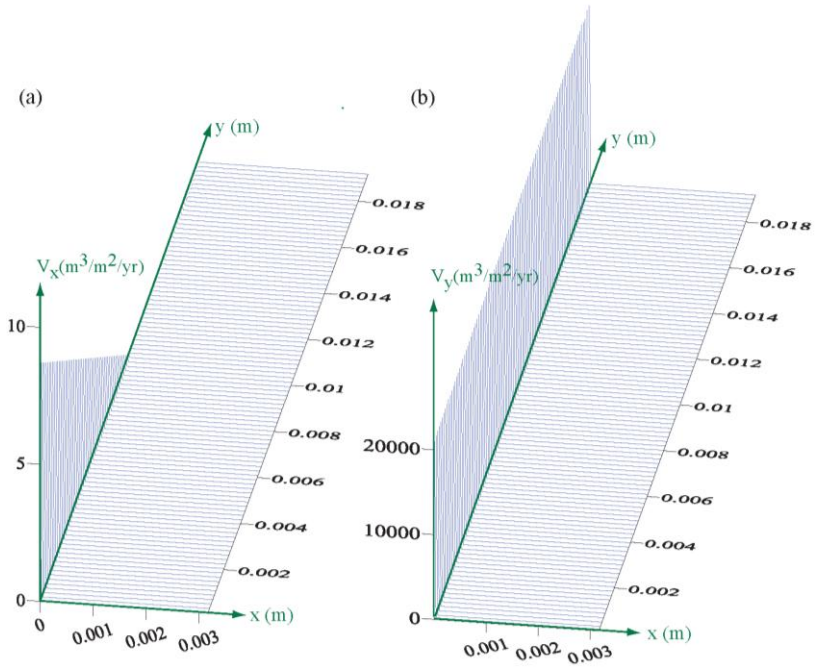

Fig. 5.4 *Velocity field for experiment L0.2-gp-e (face dissolution) at t = 46 h; Velocity ($m^3/m^2/yr$) in the x direction (Vx; left plot) and in the y direction (Vy; right plot).*

5.3.2 Wormhole

Simulation of the wormhole experiment would require the use of cylindrical coordinates and flow update. However, flow update is not implemented in CrunchFlow when cylindrical coordinates are used. Given this limitation, a model with rectangular coordinates and flow update was used to simulate just the very initial stage of the experiment by assuming that wormhole formation was not initiated yet. This approach allowed a successful match of the initial variation in Ca and S concentration with time (black-solid lines in Fig. 5.5a, b) but, as expected, did not reproduce the porosity variation with distance normal to fracture. The match of this initial stage was achieved by considering a D_e value of 3.0×10^{-12} m^2/s and adjusting the calcite and gypsum reactive surface areas (A_{Cal} = 2000 m^2_m/m^3_{bulk}; A_{Gp} = 100 m^2_m/m^3_{bulk}). Note that these areas were one order of magnitude higher than those used to fit the face-dissolution experiment using the same D_e value. The measured (SEM) porosity variation was defined by a wormhole with a radius of 600 μm at the inlet and a radius of 430 μm at the outlet (Fig. 4.6b) whereas the calculated porosity was only higher than 80% in the

first 200 μm in the *x* direction at the inlet of the fracture and, with no significant increase in porosity at the outlet.

A model with cylindrical coordinates and fixed flow was used to match the Ca and S concentration after the first initial stage. It was assumed that at this stage the wormhole was already developed. In the model the initial radius of the cylinder had to be increased from 6.7 μm (initial fracture aperture; grey-dashed line in Fig. 5.5a, b) to 402 μm (black-dashed line in Fig. 5.5a, b) to match the experimental data. This larger radius nearly coincided with the measured radius of the wormhole at the outlet of the fracture (430 μm). From here it could be deduced that solution initially circulated through both the incipient wormhole and the dissolving fracture until the moment when the radius of the wormhole was high enough to concentrate most of the flow. In this case, a good match was achieved by considering a D_e value of 3.0×10^{-12} m^2/s and adjusting the calcite and gypsum reactive surface areas (A_{Cal} = 9500 m^2_m/m^3_{bulk}; A_{Gp} = 6 m^2_m/m^3_{bulk}).

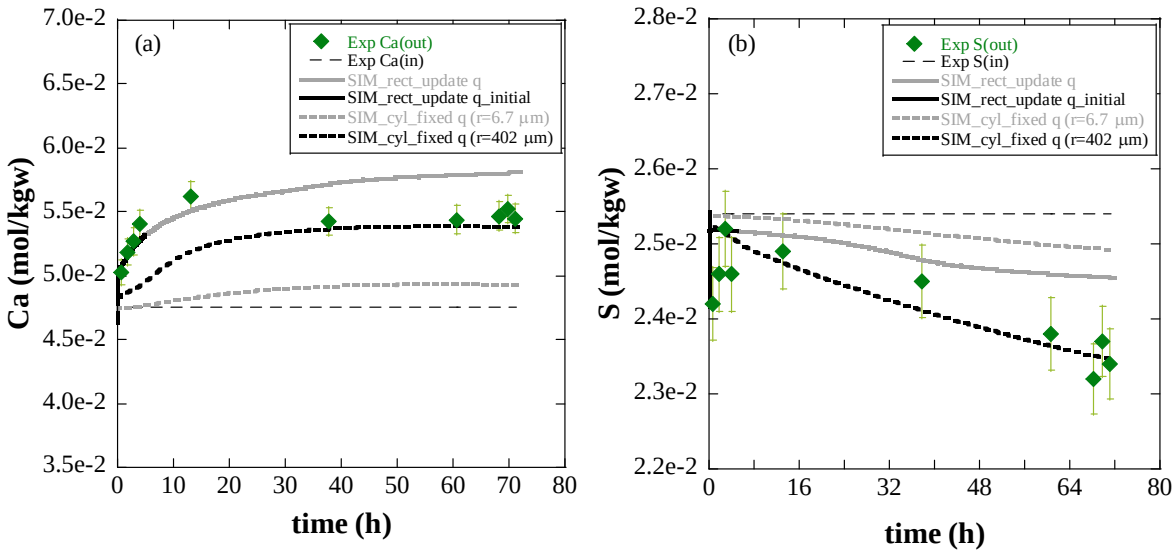

Fig. 5.5 *Experiment L1-gp-e (wormhole); simulations with rectangular coordinates (rect) and flow update (solid lines) and simulations with cylindrical coordinates (cyl) and fixed flow (dashed lines): Variation in the experimental and simulated Ca (a) and S (b) concentration versus time. r indicates the initial radius of the cylinder (see text).*

Finally, a single model that combined rectangular and cylindrical coordinates and fixed flow was used to match the full variation in Ca and S concentration with time (Fig. 5.6a, b) and in porosity with distance normal to fracture (Fig. 5.6c). The model was divided into two stages. In the first one, the first 15 h of the experiment were simulated using a model

with rectangular coordinates and fixed flow in the fracture zone. Fracture thickness corresponded to the initial fracture aperture (Table A.6, *Appendix A*). The calculated parameters obtained from this first stage were the input parameters used in the second one, in which the rest of the experiment (from 15 to 72 h) was simulated using a model with cylindrical coordinates and fixed flow imposed in a cylinder of 402 μm of radius (the first 52 nodes; Table A.6, *Appendix A*). With this approach the porosity variation with the distance normal to fracture was reasonably matched (Fig. 5.6c), indicating the creation of high porosity at the inlet (up to 600 μm) and at the outlet (up to 400 μm), as observed in the SEM images. Porosity increase was not higher than 80% owing to the precipitation of gypsum in this high-porosity area (Fig. 5.6d). Gypsum precipitation was also observed in the SEM images (Fig. 4.6b).

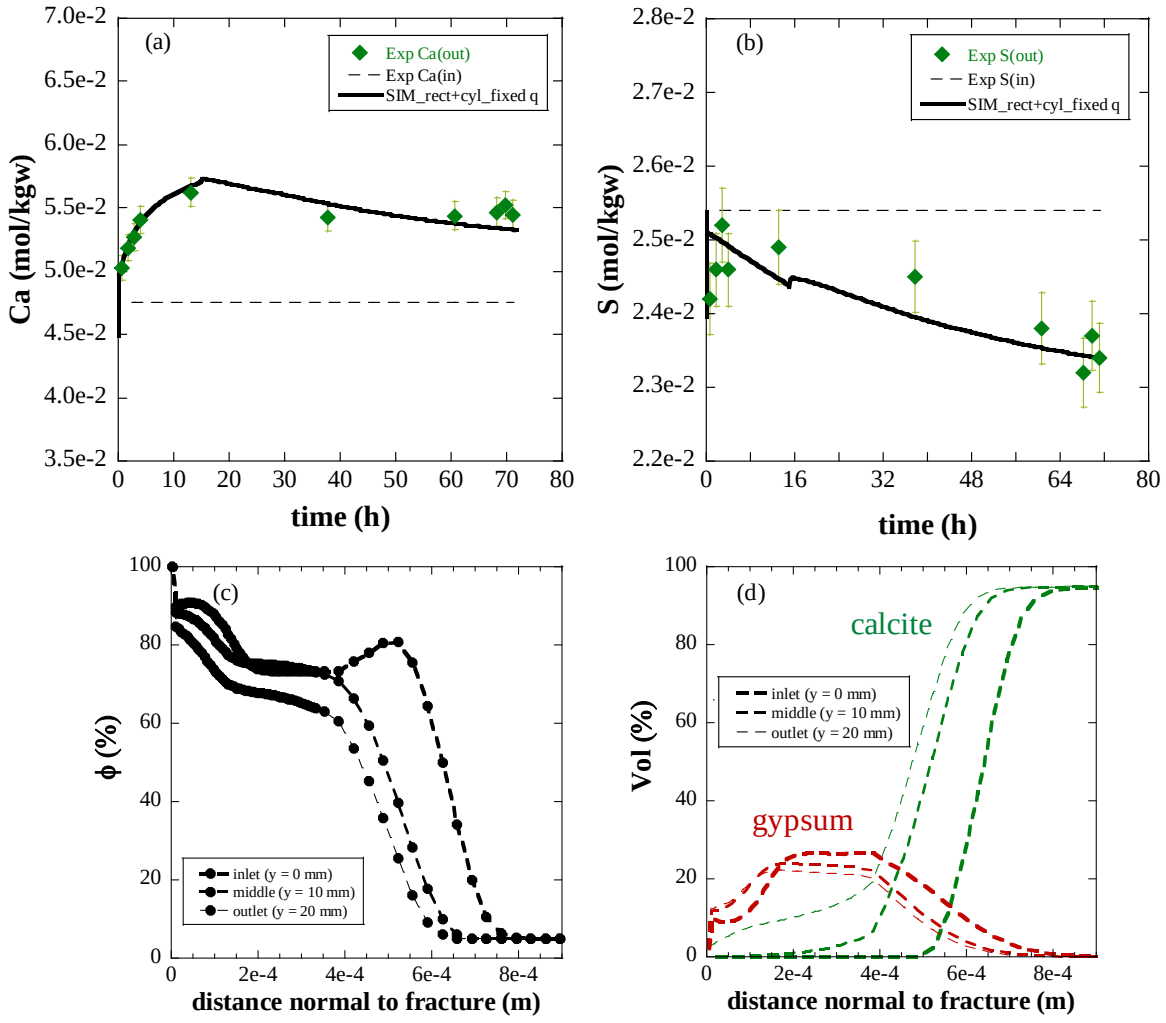

Fig. 5.6 *Experiment L1-gp-e (wormhole); simulation with rectangular + cylindrical coordinates and fixed flow: (a,b) Variation in the experimental and simulated Ca and S concentration versus time and variation in simulated porosity (c) and mineral content (d) with distance normal to fracture.*

5.3.3 Uniform dissolution

A model with rectangular coordinates and flow update was used to match the variation in Ca concentration with time (Fig. 5.7a) in experiment *S60-no-s* (uniform dissolution) with sulfate-free solution. The distance normal to fracture affected by dissolution was underestimated in the model. Indeed, the calculated porosity variation indicated high porosity (≈ 70%) up to 60 μm at the inlet (Fig. 5.7b) whereas the measured one showed high porosity (total dissolution of calcite grains; 96%) up to 100 μm from the fracture along most the fracture length (grey background in Fig. 5.7b and Fig. 4.9c). Nonetheless, the similar porosity variation all along the fracture calculated by the model was consistent with the observed dissolution pattern (uniform). As occurred in experiment *L0.2-gp-e* (face dissolution), at the end of the experiment, solution still flowed preferentially along the fracture (V_y; Fig. 5.4b), with a negligible deviation towards the rock matrix (V_x; Fig. 5.4a).

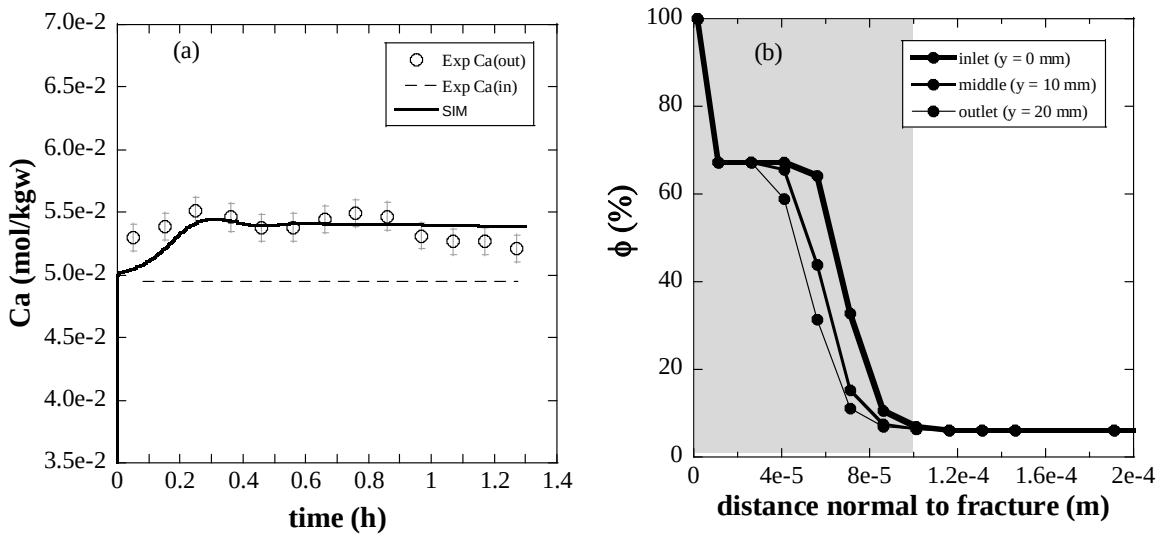

Fig. 5.7 *Experiment S60-no-s (uniform dissolution); simulation with rectangular coordinates and flow update: (a) Variation in the experimental and simulated Ca concentration versus time and (b) simulated porosity variation with the distance normal to fracture. Grey area in (b) indicates the zone with high porosity (96%) measured by SEM along most the fracture length.*

In this case, the D_e value (9.4×10^{-12} m^2/s) used in the model to reasonably reproduce the experimental data was slightly higher than that used in the wormhole simulation (3.0×10^{-12} m^2/s) for limestone, and markedly higher than that used in the face dissolution model (6.0×10^{-14} m^2/s), also for limestone. Likewise, the adjusted calcite reactive surface area was

higher than those used in previous models (A_{Cal} = 3 × 10^5 m^2_m/m^3_{bulk}). Model parameters used in this simulation are given in Table A.6, *Appendix A*.

As occurred in the experiment with face dissolution, at the end of the experiment, solution still flowed preferentially along the fracture (V_y; Fig. 5.4b), with a negligible deviation towards the rock matrix (V_x; Fig. 5.4a).

5.3.4 Flow and reaction kinetics parameters

The fit of the models was achieved by adjusting the calcite reactive surface area value (A_{Cal}) and, in some cases, the effective diffusion coefficient value (D_e).

A_{Cal} values had to be diminished from the initially calculated geometric surface area. A possible explanation for the small areas could be given by the transport control of the calcite dissolution reaction at pH < 5, which increased by decreasing the flow rate. Indeed, when D_e equaled 3.0 × 10^{-12} m^2/s and flow update was used in the models, A_{Cal} was reduced by four, three and one order of magnitude in the 0.2, 1 and 60 mL/h experiments, respectively. Note also that the net reaction rates, which include the transport effect, were larger at higher Q because more extended geometries (larger reacted area) developed under these conditions.

Regarding the wormhole experiment, the A_{Cal} value used in the model with fixed flow was a factor of five greater than that used in the model with flow update. This expected increase in reactive surface area was necessary to compensate the lack of advection in the rock matrix when fixed flow was used.

Concerning the D_e values used in the simulations, the initially estimated D_e value (3.0 × 10^{-12} m^2/s) was diminished in the slowest flow rate limestone experiment (6.0 × 10^{-14} m^2/s), kept constant for the 1 mL/h limestone experiment and slightly increased in the fastest flow rate sandstone experiment (9.5 × 10^{-12} m^2/s). In the limestone experiments, diminishing D_e was necessary to increase the fracture surface reactivity at the inlet. D_e values by one order of magnitude higher for sandstone than limestone rocks with similar porosity (3-11%) were reported by Boving and Grathwohl (2001).

5.4 Summary and conclusions

When a CO_2-rich solution interacted with the fractured reservoir rocks, on the one hand, the presence of inert silicate grains in sandstone favored the occurrence of largely distributed dissolution structures in contrast to localized dissolution in limestone. Hence, a larger area of calcite intervened in the process so that sandstone dissolution was larger than limestone dissolution. On the other hand, the dispersion of nuclei for precipitation on the inert silicate surfaces resulted in smaller gypsum precipitation in sandstone than in limestone. As a result, in sandstone reservoirs, the larger increase in fracture volume as well as the more extended distribution of the created volume would favor the CO_2 storage capacity.

The different distribution of created volume between limestone and sandstone fractured reservoir rocks promoted a different variation in fracture permeability. The progressive stepped permeability increase for sandstone would be prefer to the sharp permeability increase for limestone to minimize risks related with CO_2 injection, favor capillary trapping and reduce energetic storage costs.

The 2D reactive transport models reproduced the variation in aqueous chemistry and in porosity of the experiments by adjusting the calcite reactive surface area value (A_{Cal}) and, in some cases, the effective diffusion coefficient value (D_e) derived from literature (3.0×10^{-12} m^2/s). A_{Cal} values had to be diminished from the initially calculated geometric surface area to account for the transport control of the calcite dissolution reaction at pH < 5, which increased by decreasing the flow rate. Also, the net reaction rates (including transport effect) were larger at higher Q because of more extended geometries (larger reacted area) developed under these conditions.

D_e values for sandstone (9.5×10^{-12} m^2/s) were higher than those for limestone (3.0×10^{-12} m^2/s and 6.0×10^{-14} m^2/s), as it is found in literature for these rock with similar porosity.

Part IV:

Conclusions

Chapter 6

General conclusions

The main conclusions of this thesis are:

1) Regarding the effect of *P*, pCO_2, *T*, mineralogy, acidity and solution saturation state on the coupled reactions of calcite/dolomite dissolution and gypsum precipitation (**crushed rock):**

- Under all pCO_2 conditions, low temperature favored limestone dissolution rate although the calcite dissolution rate constants increase with temperature. This inverse tendency was explained by the fact that limestone undersaturation increased by decreasing the temperature, which suggested that the process was thermodynamically controlled.

- In experiments using gypsum-undersaturated solutions, gypsum did not precipitate and the amount of dissolved limestone was found to be slightly higher than that obtained in experiments using gypsum-equilibrated solutions. The decrease in calcite dissolution rate could be associated to the sulfate inhibitory effect and/or passivation of the calcite grain surfaces.

- As expected under the conditions of this study, the volume of dissolved limestone was larger than that of dolostone owing to the well-known faster calcite dissolution kinetics. Likewise, a pCO_2 increase implies a pH decrease that enhances substantially calcite dissolution rate with respect to that of dolomite. In addition, gypsum induction

time was longer when limestone dissolved and precipitation increased gradually. When dolostone dissolved, gypsum precipitated quickly and precipitation remained steady.

- When raising pCO_2, the limestone dissolution rate increased along the column because of the direct pH effect on the calcite dissolution rate. Dissolution of the carbonate minerals in acidic pH was controlled, under atmospheric pressure, by the protons provided by the strong acid (HCl or H_2SO_4), whereas under high pCO_2, H_2CO_3 partial dissociation controlled the dissolution. Model results showed that if brine acidity was controlled by a strong acid, dissolution occurred exclusively at the first rock-brine contact, raising the pH at ≈ 7 and limiting the limestone dissolution further away. In contrast, simulations under high pCO_2 conditions showed that pH remains acidic (≈ 5) and the brine was permanently undersaturated with respect to calcite and dolomite (due to the carbonic acid buffer capacity), yielding a higher increase in porosity all over the rock-brine contact. This suggested that calcite/dolomite dissolution induced by CO_2-rich solutions tends to extend the dissolution fronts (1) favoring the CO_2 storage capacity of the reservoir and (2) preventing localized dissolution which would lead to sharp changes in hydrodynamic rock properties, harmful for CO_2 injection.

- A good match between the CrunchFlow and PhreeqC (v.3) reactive transport calculations and the experimental data was obtained. Rate laws including the values of the rate constants were taken from literature. The fit of the model to the experimental data was performed by adjusting the values of the reactive surface areas. The calcite and dolomite reactive surface area values had to be diminished by two orders of magnitude from the initially calculated geometric surface areas. A possible explanation for the small areas could be given by the transport (diffusion) control of the dissolution reactions at pH < 5. It should be noted that a single value of the reactive area for calcite provided a good fit of the model to all experimental results, supporting the applicability of this modeling approach. The values for dolomite were more variable but continued to be within the model uncertainty.

- Overall, the coupled process of limestone/dolostone dissolution and gypsum precipitation always increased porosity (under any pCO_2). This suggested that

gypsum precipitation cannot decrease the reservoir rock porosity nor impede CO_2 injection.

2) Regarding the influence of the flow rate on dissolution and precipitation features in the percolation experiments with fractured limestone and sandstone cores (**fractured rock**):

- Injection of CO_2-rich solutions through fractured limestone and sandstone cores always produced an increase in permeability and in fracture volume even when gypsum precipitated.

- In general, the two methods (aqueous chemistry and XCMT analysis) used to calculate the variation in fracture volume induced by calcite dissolution and gypsum precipitation showed good agreement, yielding differences < 4%. Major discrepancies between them arose when wormholes developed along the lateral sealing and small gypsum crystals precipitated in experiments under fast flow rate. The XCMT resolution and image quality limited an accurate quantification of the resulting volumes of fracture and precipitated gypsum.

- By increasing the flow rate, under the same pH and far from equilibrium conditions, (1) the volume of dissolved calcite per time increased, confirming that calcite dissolution in the fracture was transport controlled, and (2) the volume of dissolved calcite per injected volume decreased, likely caused by the smaller residence time in experiments under faster flow rate. In addition, the formation of more uniform geometries under fast flow rates (*i.e.*, increase of the reacted are) led to an increase in the amount of calcite dissolved. At the micrometer scale, slow flow rates (Q = 1 and 5 mL/h) led to an increase in reactive surface area caused by an enhancement of microporosity, whereas fast flow rates (Q = 60 mL/h) tended to form smooth fracture surface which did not favor an increase in reactive surface area.

- At the same flow rate, the amount of calcite dissolved was larger in some experiments with sulfate-free solution owing to the larger reacted area related to the developed dissolution feature. Another factor contributing to the larger calcite dissolution in sulfate-free experiments than in sulfate-rich ones could be the sulfate inhibitory effect on calcite dissolution, together with gypsum coatings leading to calcite passivation.

- In general, dissolution patterns in limestone and sandstone experiments varied from face dissolution to wormhole formation and uniform dissolution by increasing the flow rate (larger Pe and smaller Da), confirming the tendency observed in previous studies (Detwiler et al., 2003; Szymczak and Ladd, 2009). Nonetheless, to predict them, initial surface heterogeneities must be taken into account since they were decisive in the evolution of the dissolving fractures.

- Variation in fracture permeability was found to be highly dependent on flow rate and developed dissolution pattern. Thus, permeability increase was very sharp when a single dominant wormhole developed, whereas it was more gradual when uniform dissolution occurred under fast flow rate. The number of fracture volumes to breakthrough increased with the flow rate. This phenomenon was attributed to the formation of more uniform dissolution structures, which induced dissolution over wider fracture surface areas.

3) Regarding the geochemical response of the two main Hontomín reservoir rocks (limestone and sandstone) to injection of a CO_2-rich sulfate solution, and the 2D simulations of the percolation experiments:

- On the one hand, during the interaction between CO_2-rich sulfate solutions and fractured reservoir rocks, the presence of inert silicate grains in sandstone favored the occurrence of largely distributed dissolution structures in contrast to localized dissolution in limestone. Consequently, a larger area of calcite could interact with the CO_2-rich solution resulting in a larger amount of calcite dissolution. On the other hand, dispersion of precipitation nuclei on the surface of the inert silicates yielded smaller volume of gypsum precipitated in sandstone than in limestone. As a result, in sandstone reservoirs, the larger increase in fracture volume, along with the more extended distribution of the created volume, would favor the increase of the CO_2 storage capacity.

- The different distribution of created volume between limestone and sandstone fractured reservoir rocks promoted a different variation in fracture permeability. A progressive stepped increase in permeability for sandstone is preferred to a sharp increase in permeability for limestone to minimize risks related with CO_2 injection, favor capillary trapping and reduce the energetic cost of storage.

- The 2D reactive transport models reproduced the variation in aqueous chemistry and in porosity of the experiments by adjusting the calcite reactive surface area value (A_{Cal}) and, in some cases, the effective diffusion coefficient value (D_e) derived from literature (3.0×10^{-12} m^2/s). As in the experiments with crushed rock, A_{Cal} values had to be diminished from the initially calculated geometric surface area to account for the transport control of the calcite dissolution reaction at pH < 5, which increased by decreasing the flow rate. D_e values for sandstone (9.5×10^{-12} m^2/s) were higher than those for limestone (3.0×10^{-12} m^2/s and 6.0×10^{-14} m^2/s), as it is found in literature for this type of sedimentary rocks and similar porosity.

References

Alcalde, J., Marzán, I., Saura, E., Martí, D., Ayarza, P., Juhlin, C., Pérez-Estaún, A., Carbonell, R., 2014. 3D geological characterization of the Hontomín CO_2 storage site, Spain: Multidisciplinary approach from seismic, well-log and regional data. Tectonophysics 627, 6–25.

Alkattan, M., Oelkers, E.H., Dandurand, J., Schott, J., 2002. An experimental study of calcite dissolution rates at acidic conditions and 25 ºC in the presence of $NaPO_3$ and $MgCl_2$. Chem. Geol. 190, 291–302.

ALM-09-008, 2010. Caracterización petrofísica de las facies jurásicas-cretácicas aflorantes en las inmediaciones de Aguilar de Campoo, equivalentes a los niveles almacén y sello presentes en la estructura geológica a utilizar como Planta de Desarrollo Tecnológico de almacenamiento geológico de CO_2. Hito 1: Informe de muestreo. CIUDEN.

Appelo, C.A.J., Parkhurst, D.L., Post, V.E.A., 2014. Equations for calculating hydrogeochemical reactions of minerals and gases such as CO_2 at high pressures and temperatures. Geochim. Cosmochim. Acta 125, 49–67.

Arvidson, R.S., Collier, M., Davis, K.J., Vinson, M.D., Amonette, J.E., Luttge, A., 2006. Magnesium inhibition of calcite dissolution kinetics. Geochim. Cosmochim. Acta 70, 583–594.

Atanassova, R., Cama, J., Soler, J.M., Offeddu, F.G., Queralt, I., Casanova, I., 2013. Calcite interaction with acidic sulphate solutions: a vertical scanning interferometry and energy-dispersive XRF study. Eur. J. Mineral. 25, 331–351.

Bachu, S., Adams, J.J., 2003. Sequestration of CO_2 in geological media in response to climate change: capacity of deep saline aquifers to sequester CO_2 in solution. Energy Convers. Manag. 44, 3151–3175.

Bachu, S., Gunter, W.D., Perkins, E.H., 1994. Aquifer disposal of CO_2: Hydrodynamic and mineral trapping. Energy Convers. Manag. 35, 269–279.

Bandstra, J. Z., Buss, H. L., Campen, R. K., Liermann, L. J., Moore, J., Hausrath, E. M., Navarre-Sitchler, A.K., Jang, J., Brantley, S. L., 2008. Appendix: compilation of mineral dissolution rates. Kinetics of Water–Rock Interaction. Springer, New York, 737-823.

Barrante, J.R., 1974. Applied Mathematics for Physical Chemistry. Prentice-Hall.

Benson, S.M., Cole, D.R., 2008. CO_2 sequestration in Deep Sedimentary Formations. Elements 4, 325-331.

Bertier, P., Swennen, R., Laenen, D., Dreesen, R., 2006. Experimental identification of CO_2-water-rock interactions caused by sequestration of CO_2 in Westphalia and Buntsandstein sandstones of the Campine Basin (NE-Belgium). J. of Geochem. Exploration 89, 10-14.

Boving, T.B., Grathwohl, P., 2001. Tracer diffusion coefficients in sedimentary rocks: correlation to porosity and hydraulic conductivity. J. Cont. Hydro. 53, 85–100.

Carroll S., Smith M., Hao Y., 2012. Evolution of carbonate dissolution features produced under variable pCO_2 conditions relevant to CO_2-EOR and geologic CO_2 storage. AiChE Annual meeting, conference proceedings 415b.

Chopping, C., Kaszuba, J.P., 2012. Supercritical carbon dioxide–brine–rock reactions in the Madison Limestone of Southwest Wyoming: An experimental investigation of a sulfur-rich natural carbon dioxide reservoir. Chem. Geol. 322-323, 223–236.

Cubillas, P., Köhler, S., Prieto, M., Chaïrat, C., Oelkers, E.H., 2005. Experimental determination of the dissolution rates of calcite, aragonite, and bivalves. Chem. Geol. 216, 59–77.

De Giudici, G., 2002. Surface control vs. diffusion control during calcite dissolution: Dependence of step-edge velocity upon solution pH. Am. Mineral., 87, 1279-1285.

De Marsily, G., 1986. Quantitative Hydrogeology. Academic Press, San Diego.

Deng, H., Ellis, B.R., Peters, C.A., Fitts, J.P., Crandall, D., Bromhal, G.S., 2013. Modifications of carbonate fracture hydrodynamic properties by CO_2-acidified brine flow. Energy & Fuels 27, 4221-4231.

Detwiler, R.L., 2008. Experimental observations of deformation caused by mineral dissolution in variable-aperture fractures. J. Geophys. Res. 113, B08202.

Detwiler, R.L., Glass, R.J., Bourcier, W.L., 2003. Experimental observations of fracture dissolution: The role of Peclet number on evolving aperture variability. Geophys. Res. Lett. 30, 1648.

Detwiler, R.L., Rajaram, H., 2007. Predicting dissolution patterns in variable aperture fractures: Evaluation of an enhanced depth-averaged computational model. Water Resour. Res. 43, W04403.

Dijk, P.E., Berkowitz, B., Yechieli, Y., 2002. Measurement and analysis of dissolution patterns in rock fractures. Water Resour. Res. 38, 1013.

Domenico, P.A., Schwartz, F.W., 1990. Physical and Chemical Hydrogeology. John Wiley and Sons, New York.

Downs, R.T., 2006. The RRUFF Project: an integrated study of the chemistry, crystallography, Raman and infrared spectroscopy of minerals. Program and Abstracts of the 19th General Meeting of the International Mineralogical Association in Kobe, Japan. O03-13

Duan, Z., Sun, R., 2003. An improved model calculating CO_2 solubility in pure water and aqueous NaCl solutions from 273 to 533 K and from 0 to 2000 bar. Chem. Geol. 193, 257–271.

Durham, W.B., Bourcier, W.L., Burton, E.A., 2001. Direct observation of reactive flow in a single fracture. Water Resour. Res. 37, 1–12.

Elkhoury, J.E., Ameli, P., Detwiler, R.L., 2013. Dissolution and deformation in fractured carbonates caused by flow of CO_2-rich brine under reservoir conditions. Int. J. Greenh. Gas Control 16, S203–S215.

Ellis, B., Peters, C., Fitts, J., Bromhal, G., McIntyre, D., Warzinski, R., Rosenbaum, E., 2011. Deterioration of a fractured carbonate caprock exposed to CO_2-acidified brine flow. Greenh. Gases Sci. and Technol. 1:248–260.

Espinoza, D.N., Kim, S.H., Santamarina, J.C., 2011. CO_2 geological storage — Geotechnical implications. KSCE J. Civ. Eng. 15, 707–719.

Fisher, S., Liebscher, A., Wandrey, M., the CO_2 SINK Group, 2010. CO_2-brine-rock interaction – first results of long-term exposure experiments at in situ P-T conditions of the Ketzin CO_2 reservoir. Chemie der Erde 70, 155-164.

Fredd, C.N., Fogler, H.S., 1998. Influence of transport and reaction on wormhole formation in porous media. AIChE Journal 44, 1933-1949.

Gao, X., Huo, W., Zhong, Y., Luo, Z., Cen, K., Ni, M., Chen, L., 2008. Effects of Magnesium and Ferric Ions on Crystallization of Calcium Sulfate Dihydrate Under the Simulated Conditions of Wet Flue-gas Desulfurization. Chem. Res. in Chinese Universities 24, 688-693.

Garcia-Rios, M., Cama, J., Luquot, L., Soler, J.M., 2014. Interaction between CO_2-rich sulfate solutions and carbonate reservoir rocks from atmospheric to supercritical CO_2 conditions: Experiments and modeling. Chem. Geol. 383, 107–122.

Gaus, I., 2010. Role and impact of CO_2–rock interactions during CO_2 storage in sedimentary rocks. Int. J. Greenh. Gas Control 4, 73–89.

Gherardi, F., Xu, T., Pruess, K., 2007. Numerical modeling of self-limiting and self-enhancing caprock alteration induced by CO_2 storage in a depleted gas reservoir. Chem. Geol. 244, 103–129.

Gledhill, D.K., Morse, J.W., 2006. Calcite dissolution kinetics in Na–Ca–Mg–Cl brines. Geochim. Cosmochim. Acta 70, 5802–5813.

Global Status of CCS, 2013. The Global CCS Institute, Melbourne, Australia.

Golfier, F., Zarcone, C., Bazin, B., Lenormand, R., Lasseux, D., Quintard, M., 2002. On the ability of a Darcy-scale model to capture wormhole formation during the dissolution of a porous medium. J. Fluid Mech. 457, 213–254.

Gouze, P., Noiriel, C., Bruderer, C., Loggia, D., Leprovost, R., 2003. X-ray tomography characterization of fracture surfaces during dissolution. Geophys. Res. Lett. 30, 1267.

Gunter, W.D., Bachu, S., Benson, S.M, 2004. The role of hydro-geological and geochemical trapping in sedimentary basins for secure geological storage of carbon dioxide, in: Baines, S.J., Worden, R.H. (Eds.), Geological Storage of Carbon Dioxide. Geological Society Special Publication, vol. 233, pp. 129-145. London, UK.

Gunter, W.D., Wiwchar, B., Perkins, E.H., 1997. Aquifer disposal of CO_2-rich greenhouse gases: extension of the time scale of experiment for CO_2-sequestration reactions by geochemical modelling. Mineral. and Petrol. 59, 121–140.

Hao, Y., Smith, M., Sholokhova, Y., Carroll, S., 2013. CO_2-induced dissolution of low permeability carbonates. Part II: Numerical modeling of experiments. Adv. Water Resour. 62, 388-408.

Hidalgo, J.J., Carrera, J., 2009. Effect of dispersion on the onset of convection during CO_2 sequestration. J. Fluid. Mech. 640, 441-452.

Hoefner, M.L., Fogler, H.S., 1988. Pore Evolution and Channel Formation During Flow and Reaction in Porous Media. Am. Inst. Chem. Eng. 34, 45–54.

Huitt, J.L., 1956. Fluid flow in simulated fractures, Am. Inst. Chem. Eng. 2, 259–264.

Intergovernmental Panel on Climate Change (IPCC), 2005. IPCC Special Report on Carbon Dioxide Capture and Storage. Cambridge University Press, Cambridge, UK, pp. 195-276.

Intergovernmental Panel on Climate Change (IPCC), 2014. Climate Change 2014: Mitigation of Climate Change. Contribution of Working Group III to the Fifth Assessment Report of the Intergovernmental Panel on Climate Change [Edenhofer, O., R. Pichs-Madruga,

Y. Sokona, E. Farahani, S. Kadner, K. Seyboth, A. Adler, I. Baum, S. Brunner, P. Eickemeier, B. Kriemann, J. Savolainen, S. Schlömer, C. von Stechow, T. Zwickel and J.C. Minx (eds.)]. Cambridge University Press, Cambridge, United Kingdom and New York, NY, USA.

International Energy Agency (IEA), 2010. Energy technology perspectives. Scenarios & strategies to 2050. Executive summary. IEA, France

International Energy Agency (IEA), 2013. CO_2 emissions from fuel combustion. Highlights. OECD/IEA, France.

Johnson, J.W., Nitao, J.J., Steefel, C.I., Knauss, K.G., 2001. Reactive transport modeling of geologic CO_2 sequestration in saline aquifers: the influence of intra-aquifer shales and the relative effectiveness of structural, solubility, and mineral trapping during prograde and retrograde sequestration. First National Conference on Carbon Sequestration. May 14-17, 2001, Washingtin D.C. pp. 60.

Kalia, N., Balakotaiah, V., 2009. Effect of medium heterogeneities on reactive dissolution of carbonates. Chem. Eng. Sci. 64, 376–390.

Kaszuba, J.P., Janecky, D.R., Snow, M.G., 2003. Carbon dioxide reaction processes in a model brine aquifer at 200 °C and 200 bars: implications for geologic sequestration of carbon. Appl. Geochemistry 18, 1065–1080.

Kaszuba, J.P., Janecky, D.R., Snow, M.G., 2005. Experimental evaluation of mixed fluid reactions between supercritical carbon dioxide and NaCl brine: Relevance to the integrity of a geologic carbon repository. Chem. Geol. 217, 277–293.

Knauss, K.G., Johnson, J.W., Steefel, C.I., 2005. Evaluation of the impact of CO_2, co-contaminant gas, aqueous fluid and reservoir rock interactions on the geologic sequestration of CO_2. Chem. Geol. 217, 339–350.

Koschel, D., Coxam, J-Y., Rodier, L., Majer, V., 2006. Enthalpy and solubility data of CO_2 in water and NaCl(aq) at conditions of interest for geological sequestration. Fluid Phase Equilibria 247, 107-120.

Liu, J., Polak, A., Elsworth, D., Grader, A., 2005. Dissolution-induced preferential flow in a limestone fracture. J. Contam. Hydrol. 78, 53–70.

Lu, J., Kharaka, Y.K., Thordsen, J.J., Horita, J., Karamalidis, A., Griffith, C., Hakala, J.A., Ambats, G., Cole, D.R., Phelps, T.J., Manning, M.A., Cook, P.J., Hovorka, S.D., 2012. CO_2–rock–brine interactions in Lower Tuscaloosa Formation at Cranfield CO_2 sequestration site, Mississippi, U.S.A. Chem. Geol. 291, 269–277.

Luhmann, A.J., Kong, X.-Z., Tutolo, B.M., Garapati, N., Bagley, B.C., Saar, M.O., Seyfried, W.E., 2014. Experimental dissolution of dolomite by CO_2-charged brine at 100°C and 150bar: Evolution of porosity, permeability, and reactive surface area. Chem. Geol. 380, 145–160.

Luquot, L., Andreani, M., Gouze, P., Camps, P., 2012. CO_2 percolation experiment through chlorite/zeolite-rich sandstone (Pretty Hill Formation – Otway Basin–Australia). Chem. Geol. 294-295, 75–88.

Luquot, L., Gouze, P., 2009. Experimental determination of porosity and permeability changes induced by injection of CO_2 into carbonate rocks. Chem. Geol. 265, 148–159.

Luquot, L., Rodriguez, O., Gouze, P., 2013. Experimental Characterization of Porosity Structure and Transport Property Changes in Limestone Undergoing Different Dissolution Regimes. Transp. Porous Media. DOI 10.1007/s11242-013-0257-4.

Luquot, L., Rodriguez, O., Gouze, P., 2014. Experimental Characterization of Porosity Structure Undergoing Different Dissolution Regimes. Transp. Porous Media 101, 507–532.

Martin-Garin, A., Van Cappellen, P., Charlet, L., 2003. Aqueous cadmium uptake by calcite: A stirred flow-through reactor study. Geochim. Cosmochim. Acta 67, 2763–2774.

Morse, J.W., Arvidson, R.S., 2002. The dissolution kinetics of major sedimentary carbonate minerals. Earth-Science Rev. 58, 51–84.

Mount, J., 1985. Mixed siliciclastic and carbonate sediments: a proposed first-order textural and compositional classification. Sedimentology, 32: 435–442. doi: 10.1111/j.1365-3091.1985.tb00522.x

Nogues, J.P., Fitts, J.P., Celia, M.A., Peters, C.A., 2013. Permeability evolution due to dissolution and precipitation of carbonates using reactive transport modeling in pore networks. Water Resour. Res. 49, 6006–6021.

Noiriel, C., Bernard, D., Gouze, P., Thibault, X., 2005. Hydraulic Properties and Microgeometry Evolution Accompanying Limestone Dissolution by Acidic Water. Oil Gas Sci. Technol. 60, 177–192.

Noiriel, C., Gouze, P., Bernard, D., 2004. Investigation of porosity and permeability effects from microstructure changes during limestone dissolution. Geophys. Res. Lett. 31, L24603.

Noiriel, C., Gouze, P., Madé, B., 2013. 3D analysis of geometry and flow changes in a limestone fracture during dissolution. J. Hydrol. 486, 211–223.

Noiriel, C., Luquot, L., Madé, B., Raimbault, L., Gouze, P., van der Lee, J., 2009. Changes in reactive surface area during limestone dissolution: An experimental and modeling study. Chem. Geol. 265, 160–170.

Noiriel, C., Madé, B., Gouze, P., 2007. Impact of coating development on the hydraulic and transport properties in argillaceous limestone fracture. Water Resour. Res. 43, W09406.

Nordstrom, D.K., 2013. Improving internal consistency of standard state thermodynamic data for sulfate ion , portlandite , gypsum , barite , celestine , and associated ions. Procedia Earth Planet. Sci. 7, 624–627.

Oelkers, E.H., Gislason, S.R., Matter, J., 2008. Mineral carbonation of CO_2. Elements 4, 333-337.

Offeddu, F.G., Cama, J., Soler J.M., Putnis C.V., 2014. Direct nanoscale observations of the coupled dissolution of calcite and dolomite and gypsum precipitation. Beilstein J. Nanotech. 5, 1245-1253.

Offeddu, F.G., Cama, J., Soler, J.M., Dávila, G., McDowell, A., Craciunescu, T., Tiseanu, I., 2015. Processes affecting the efficiency of limestone in passive treatments for AMD: Column experiments. J. Environ. Chem. Eng. 3, 304-316.

Oldenburg, C., 2007. Migration mechanisms and potential impacts of CO_2 leakage and seepage. In: Wilson, E.J., Gerard, D. (eds) Carbon Capture and Sequestration: Integrating Technology, Monitoring, Regulation. Blackwell Publishing, pp. 127-146.

Ossorio, M., Van Driessche, A.E.S., Pérez, P. and Garcia-Ruiz, J.M., 2013. Precipitation and stability behavior of calcium sulfate: the role of salinity temperature and reaction time. Goldschmidt 2013 Conference Abstracts 1899.

Palandri, J.L. Kharaka, Y.K., 2004. A compilation of rate parameters of water-mineral interaction kinetics for application to geochemical modeling. Science for a changing world. U.S. Geol. Surv. Open File Report 2004-1068.

Palandri, J.L., Kharaka, Y.K., 2005. Ferric iron-bearing sediments as a mineral trap for CO_2 sequestration: Iron reduction using sulfur-bearing waste gas. Chem. Geol. 217, 351–364.

Parkhurst, D.L., Appelo, C.A.J., 2013. Description of input and examples for PHREEQC (Version 3)-a computer program for speciation, batch-reaction, one-dimensional transport, and inverse geochemical calculations. U.S. Geological Survey Techniques and methods report. Book 6, 49.

Plummer, L.N., Wigley, T.M.L., Parkhust, D.L., 1978: The kinetics of calcite dissolution in CO_2-water systems at 5º and 60 ºC and 0.0 to 1.0 atm CO_2. Am. J. Sci., 278, 179-216.

Pokrovsky, O.S., Golubev, S.V., Schott, J., 2005. Dissolution kinetics of calcite, dolomite and magnesite at 25 °C and 0 to 50 atm pCO_2. Chem. Geol. 217, 239–255.

Pokrovsky, O.S., Golubev, S.V., Schott, J., Castillo, A., 2009. Calcite, dolomite and magnesite dissolution kinetics in aqueous solutions at acid to circumneutral pH, 25 to 150 °C and 1 to 55 atm pCO_2: New constraints on CO_2 sequestration in sedimentary basins. Chem. Geol. 265, 20–32.

Polak, A., Elsworth, D., Liu, J., Grader, A.S., 2004. Spontaneous switching of permeability changes in a limestone fracture with net dissolution. Water Resour. Res. 40, W03502.

Prisciandaro, M., Lancia, A., Musmarra, D., 2001. Calcium Sulfate Dihydrate Nucleation in the Presence of Calcium and Sodium Chloride Salts. Ind. Eng. Chem. Res. 40, 2335–2339.

Pujalte, V., Robles, S., Hernández, J.M., 1998. La sedimentación continental del Grupo Campóo (Malm-Cretácico basal de Cantabria, Burgos y Palencia): testimonio de un reajuste hidrográfico al inicio de una fase rift. Cuadenos de Geología Ibérica, 21, 227-251.

Rashad, M.M., Mahmoud, M.H.H., Ibrahim, I.A., Abdel-Aal, E.A., 2004. Crystallization of calcium sulfate dihydrate under simulated conditions of phosphoric acid production in the presence of aluminum and magnesium ions. J. Cryst. Growth 267, 372–379.

Reznik, I.J., Ganor, J., Gruber, C., Gavrieli, I., 2012. Towards the establishment of a general rate law for gypsum nucleation. Geochim. Cosmochim. Acta 85, 75–87.

Rimmelé, G., Barlet-Gouédard, V., Renard, F., 2010. Evolution of the Petrophysical and Mineralogical Properties of Two Reservoir Rocks Under Thermodynamic Conditions Relevant for CO_2 Geological Storage at 3 km Depth. Oil Gas Sci. Technol. – Rev. l'Institut Français du Pétrole 65, 565–580.

Rosenbauer, R.J., Koksalan, T., Palandri, J.L., 2005. Experimental investigation of CO_2–brine–rock interactions at elevated temperature and pressure: Implications for CO_2 sequestration in deep-saline aquifers. Fuel Process. Technol. 86, 1581–1597.

Rötting, T.S., Thomas, R.C., Ayora, C., Carrera, J., 2008. Passive treatment of acid mine drainage with high metal concentrations using dispersed alkaline substrate. J. Environ. Qual. 37, 1741–51.

Singurindy, O., Berkowitz, B., 2003. Evolution of hydraulic conductivity by precipitation and dissolution in carbonate rock. Adv. Water Resour. 39, 1016.

Sjöberg, E.L., 1978. Kinetics and mechanism of calcite dissolution in aqueous solutions at low temperature. Stockholm Contr. Geol. 32, 1–96.

Sjöberg, E.L., Rickard, D.T., 1984. Temperature-dependence of calcite dissolution kinetics between 1º C and 62 ºC at pH 2.7 to 8.4 in aqueous-solutions. Geochim. Cosmochim. Acta 48, 485–493.

Smith, M.M., Sholokhova, Y., Hao, Y., Carroll, S. A., 2013. CO_2-induced dissolution of low permeability carbonates. Part I: Characterization and experiments. Adv. Water Resour. 62, 370–387.

Söhnel, O., Mullin, J.W., 1988. Interpretation of Crystallization Induction Periods. J. Colloid Interface Sci. 123.

Spycher, N., Pruess, K., Ennis-King, J., 2003. CO_2-H_2O mixtures in the geological sequestration of CO_2. I. Assessment and calculation of mutual solubilities from 12 to 100 ºC and up to 600 bar. Geochim. Cosmochim. Acta 67, 3015–3031.

Steefel, C.I., 2009. CrunchFlow. Software for Modeling Multicomponent Reactive Flow and Transport. User´s Manual. Lawrence Berkeley National Laboratory, Berkeley, USA.

Steefel, C.I., Appelo, C.A.J., Arora, B., Jacques, D., Kalbacher, T., Kolditz, O., Lagneau, V., Lichtner, P.C., Mayer, K.U., Meeussen, J.C.L., Molins, S., Moulton, D., Shao, H., Šimůnek, J., Spycher, N., Yabusaki, S.B., Yeh, G.T., 2014. Reactive transport codes for subsurface environmental simulation. Comput. Geosci. DOI10.1007/s10596-014-9443-x

Szymczak, P., Ladd, A.J.C., 2004. Microscopic simulations of fracture dissolution. Geophys. Res. Lett. 31, L23606.

Szymczak, P., Ladd, A.J.C., 2004a. Stochastic boundary conditions to the convection-diffusion equation including chemical reactions at solid surfaces. Phys. Rev. E 69, 036704.

Szymczak, P., Ladd, A.J.C., 2009. Wormhole formation in dissolving fractures. J. Geophys. Res. 114, B06203.

Takenouchi, S., Kennedy, G.C., 1964. The binary system H_2O-CO_2 at high temperatures and pressures. Am. J. of Sci. 262, 1055–1074.

Ullman, W.J., Aller, R.C., 1982. Diffusion coefficients in near shore marine sediments. Limnol. Oceanog. 27, 552-534.

Van Driessche, A.E.S., Benning, L.G., Rodriguez-Blanco, J.D., Ossorio, M., Bots, P., García-Ruiz, J.M., 2012. The role and implications of bassanite as a stable precursor phase to gypsum precipitation. Science 336, 69–72.

Verberg, R., Ladd, A.J.C., 1999. Simulations of low-Reynolds-number flow via a time-independent lattice-Boltzmann method. Phys. Rev. E 60, 3366-3373.

Verberg, R., Ladd, A.J.C., 2002. Simulations of erosion in narrow fractures. Phys. Rev. E 65, 016701.

Wandrey, M., Fischera, S., Zemkea, K., Liebschera, A., Scherfb, A.K., Hillebrandb, A.V., Zettlitzerc, M., Würdemann, H., 2011. Monitoring petrophysical, mineralogical, geochemical and microbiological effects of CO_2 exposure — Results of long-term experiments under in situ conditions. Energy Procedia 4, 3644-3650.

Weibel, R., Kjoller, C., Bateman, K., Nielsen, L.H., Frykman, P., Springer, N., Laier, T., 2011. Mineral changes in CO2 experimetns-examples from Danish onshore saline aquifers. Energy Procedia 4, 4495-4502.

Wigand, M., Carey, J.W., Schütt, H., Spangenberg, E., Erzinger, J., 2008. Geochemical effects of CO_2 sequestration in sandstones under simulated in situ conditions of deep saline aquifers. Appl. Geochemistry 28, 2735-2745.

Witherspoon, P.A., Wang, J.S.Y., Iwai, K., Gale, J.E., 1980. Validity of cubic law for fluid flow in a deformable rock fracture. Water Resour. Res. 16, 1016–1024.

Wolery, T. J., Jackson, K.J., Bourcier, W.L., Bruton, C.J., Viani, B.E., Knauss, K.G. and Delany, J.M., 1990. Current status of the EQ3/6 software package for geochemical modeling, in: Melchior, C., Bassett, R.L. (Eds.), Chemical Modeling of Aqueous Systems II. Am. Chem. Soc. Symp. Ser. 416, 104-116.

Xu, J., Fan, C., Teng, H.H., 2012. Calcite dissolution kinetics in view of Gibbs free energy, dislocation density, and pCO_2. Chem. Geol. 322-323, 11–18.

Xu, M., Higgins, S.R., 2011. Effects of magnesium ions on near-equilibrium calcite dissolution: Step kinetics and morphology. Geochim. Cosmochim. Acta 75, 719–733.

Xu, T., Apps, J.A., Pruess, K., 2005. Mineral sequestration of carbon dioxide in a sandstone–shale system. Chem. Geol. 217, 295–318.

Yang, C., Gu, Y., 2006. Accelerated Mass Transfer of CO_2 in Reservoir Brine Due to Density-Driven Natural Convection at High Pressures and Elevated Temperatures. Ind. Eng. Chem. Res. 45, 2430-2436.

Young, R.A., 1995. The Rietveld Method, vol. 5, International Union of Crystallography Monographs on Crystallography. Oxford University Press, USA.

Yushkevich, P. A, Piven, J., Hazlett, H.C., Smith, R.G., Ho, S., Gee, J.C., Gerig, G., 2006. User-guided 3D active contour segmentation of anatomical structures: significantly improved efficiency and reliability. NeuroImage 31, 1116–28.

Appendix A

1D and 2D model parameters

A.1 (1D) model parameters

A.1.1 CrunchFlow simulations

Table A.1 *Experimental and input boundary conditions, transport parameters, numerical discretization and rock composition used in simulations of column experiments under atmospheric CO_2 conditions.*

Experiment label		*D25-atm-s*	*L25-atm-s*		*L25-atm-a3.5*	*L60-atm-a3.5*	*L25-atm-a2.1*		*L60-atm-a2.1*	
EXPERIMENTAL CONDITIONS										
T	(ºC)	25	25		25	60	25		60	
P	(bar)	1	1		1	1	1		1	
p CO_2	(bar)	$10^{-3.5}$	$10^{-3.5}$		$10^{-3.5}$	$10^{-3.5}$	$10^{-3.5}$		$10^{-3.5}$	
Flow Rate *Q*	mL/min	0.021	0.023		0.020	0.021	0.020		0.020	
Column Dimensions										
Length	(m)	0.026	0.026		0.026	0.026	0.026		0.026	
Radius	(m)	0.013	0.013		0.013	0.013	0.013		0.013	
Rock Sample										
Rock		D	L		L	L	L		L	
Mass	(g)	21.15	20.82		19.41	19.43	19.37		19.42	
Grain diameter	(mm)	1-2	1-2		1-2	1-2	1-2		1-2	
Density	(g/cm^3)	2.84	2.72		2.72	2.72	2.72		2.72	
TRANSPORT PARAMETERS										
Initial porosity ϕ_0	%	46.06	44.55		48.31	48.26	48.41		48.28	
Darcy velocity *q*	$m^3/m^2/s$	6.62E-07	7.06E-07		6.28E-07	6.59E-07	6.28E-07		6.28E-07	
Eff. Diff. coeff. D_e	m^2/s	2.12E-10	1.98E-10		2.33E-10	2.33E-10	2.34E-10		2.33E-10	
Long. dispersivity α_L	m	1.30E-03	1.30E-03		1.30E-03	1.30E-03	1.30E-03		1.30E-03	
DISCRETIZATION										
Number of elements		20	20		20	20	40 + 16		40 + 16	
Element dimension	m	1.3E-03	1.3E-03		1.3E-03	1.3E-03	1.3E-04	1.3E-03	1.3E-04	1.3E-03
ROCK COMPOSITION										
Volume Fraction										
Cal		-	0.5028		0.4688	0.4691	0.4678		0.4690	
Dol-dis		0.5400	0.0517		0.0482	0.0482	0.0481		0.0482	
A_m (m^2_m/m^3_{bulk})										
Cal		-	120(80 - 180)							
Dol -dis		17(16 - 20)	5(4 - 7)		5(0-20)					
			initial	final			initial	final	initial	final
Gp-25		0.03(0.01-0.06)	0.001(0-0.01)	0.015(0.01-0.03)	0(0-0.03)	-	0.01(0-0.1)	0.1(0.02-0.2)	-	-
Gp-40		-	-	-	-	-	-	-	-	-
Gp-60		-	-	-	-	0(0-0.005)	-	-	0.01(0.015-0.03)	0.04(0.02-0.05)
INPUT BOUNDARY CONDITIONS										
Input label		***s***			***a3.5***		***a2.1***			
SI, I and pH (CrunchFlow)										
Cal		-10.33	-10.34		-8.01	-7.77	-10.84		-10.60	
Dol-dis		-22.85	-23.53		-16.55	-15.74	-22.18		-21.36	
Gp-25		0.09	0.08		0.05	-	-0.03		-	
Gp-40		-	-		-	-	-		-	
Gp-60		-	-		-	0.04	-		-0.09	
I		0.05			0.63	0.62	0.61		0.59	
pH		2.50			3.50		2.10			

L = limestone; D = dolostone.

Cal = calcite; Dol-dis = disordered dolomite; Gp = gypsum.

A_m = Reactive surface area. A_m in brackets indicates the range of values that fits the experimental concentration data (within ± 2 % uncertainty) in the sensitivity study.

Table A.2 *Experimental and input boundary conditions, transport parameters, numerical discretization and rock composition used in simulations of column experiments under subcritical and supercritical CO_2 conditions.*

Experiment label		*L25-10-gp-u*	*L40-10-gp-u*	*L25-10-gp-e*		*L40-10-gp-e*		*L60-10-gp-e*		*D40-10-gp-e*	*L60-34-gp-e*
EXPERIMENTAL CONDITIONS											
T	(ºC)	25	40	25		40		60		40	60
P	(bar)	10	10	10		10		10		10	150
pCO_2	(bar)	10	10	10		10		10		10	34
Flow Rate *Q*	mL/min	0.063	0.062	0.056		0.055		0.055		0.058	0.010
Column Dimensions											
Length	(m)	0.054	0.054	0.054		0.054		0.054		0.054	0.017
Radius	(m)	0.016	0.016	0.016		0.016		0.016		0.016	0.004
Rock Sample											
Rock		L	L	L		L		L		D	L
Mass	(g)	61.60	56.00	62.61		58.27		59.23		61.60	0.8523
Grain diameter	(mm)	1-2	1-2	1-2		1-2		1-2		1-2	250-500
Density	(g/cm^3)	2.72	2.72	2.72		2.72		2.72		2.84	2.72
TRANSPORT PARAMETERS											
Initial porosity ϕ_0	%	47.85	52.59	47		50.67		49.86		50.06	54.77
Darcy velocity *q*	$m^3/m^2/s$	1.31E-06	1.29E-06	1.16E-06		1.14E-06		1.14E-06		1.20E-06	4.33E-06
Eff. Diff. coeff. D_e	m^2/s	2.29E-10	2.77E-10	2.21E-10		2.57E-10		2.49E-10		2.51E-10	3.00E-10
Long. dispersivity α_L		1.30E-03	1.30E-03	1.30E-03		1.30E-03		1.30E-03		1.30E-03	1.30E-03
DISCRETIZATION											
Number of elements		20	20	20		20		20		20	20
Element dimension	m	2.7E-03	2.7E-03	2.7E-03		2.7E-03		2.7E-03		2.7E-03	9.0E-04
ROCK COMPOSITION											
Volume Fraction											
Cal		0.4729	0.4299	0.4806		0.4473		0.4546		-	0.4102
Dol-dis		0.0486	0.0442	0.0494		0.0460		0.0467		0.4994	0.0422
A_m (m^2_m/m^3_{bulk})											
Cal		120(80 - 180)								-	120(80 - 180)
Dol -dis		5(0 - 10)								5(3 - 10)	10(5 - 30)
				initial	final	initial	final	initial	final		
Gp-25		-	-	0.01(0-0.1)	10(1-*)	-	-	-	-	-	-
Gp-40		-	-	-	-	0.01(0-0.04)	0.3(0.1-*)	-	-	0.3(0.08-*)	-
Gp-60		-	-	-	-	-	-	0.01(0-0.1)	0.1(0.01-*)	-	0.5(0.2 -*)
INPUT BOUNDARY CONDITIONS											
Input label		***gp-u***		***gp-e***							
SI, I and pH (CrunchFlow)											
Cal		-3.45	-3.22	-3.48		-3.21		-2.88		-3.19	-2.96
Dol-dis		-7.34	-6.71	-7.47		-6.77		-5.96		-6.74	-6.07
Gp-25		-0.19	-	0.00		-		-		-	-
Gp-40		-	-0.20	-		-0.01		-		0.01	-
Gp-60		-	-	-		-		-0.03		-	-0.04
I		0.60	0.61	0.61		0.62		0.58		0.63	0.60
pH		3.65**	3.7**	3.61**		3.68**		3.78**		3.68**	3.53

A_m = Reactive surface area. A_m in brackets indicates the range of values that fits the experimental concentration data (within ± 2 % uncertainty) in the sensibility study.

L = limestone; D = dolostone.

Cal = calcite; Dol-dis = disordered dolomite; Gp = gypsum.

* Maximum value is not constrained within the experimental error; solution reached equilibrium in the column.

** CrunchFlow (charge balance) calculated pH, similar to the measured averaged pH (see *Table 3.1*).

Table A.3 *Equilibrium constants (log K) and stoichiometric coefficients for equilibria in solution (column experiments and fractured core experiments L0.2-gp-e and L1-gp-e). Reactions are written as the destruction of 1 mol of the species in the first column. * indicates species used in the atmospheric CO_2 experiments with H_2SO_4 input solution (s).*

Species	log K 25°C	log K 40°C	log K 60°C	Stoichiometric coefficient								
				Ca^{2+}*	Mg^{2+}*	HCO_3^-*	H^+*	SO_4^{2-}*	K^+	Br^-	Cl^-	Na^+
CO_2(aq) *	-6.3414E+00	-6.2824E+00	-6.2695E+00	0	0	1	1	0	0	0	0	0
CO_3^{2-} *	1.0325E+01	1.0218E+01	1.0132E+01	0	0	1	-1	0	0	0	0	0
$CaCO_3$(aq) *	7.0088E+00	6.7507E+00	6.4479E+00	1	0	1	-1	0	0	0	0	0
$CaCl^+$	7.0039E-01	6.6684E-01	5.8650E-01	1	0	0	0	0	0	0	1	0
$CaCl_2$(aq)	6.5346E-01	6.7258E-01	6.2447E-01	1	0	0	0	0	0	0	2	0
$CaHCO_3^+$ *	-1.0429E+00	-1.0743E+00	-1.1605E+00	1	0	1	0	0	0	0	0	0
$CaOH^+$ *	1.2850E+01	1.2850E+01	1.2850E+01	1	0	0	-1	0	0	0	0	0
$CaSO_4$(aq) *	-2.1004E+00	-2.1626E+00	-2.2698E+00	1	0	0	0	1	0	0	0	0
H_2SO_4(aq)	1.0209E+00	1.0209E+00	1.0209E+00	0	0	0	2	1	0	0	0	0
HCl(aq)	-6.9993E-01	-6.9322E-01	-6.6883E-01	0	0	0	1	0	0	0	1	0
HSO_4^- *	-1.9755E+00	-2.1656E+00	-2.4383E+00	0	0	0	1	1	0	0	0	0
KBr(aq)	1.7423E+00	1.6141E+00	1.4461E+00	0	0	0	0	0	1	1	0	0
KCl(aq)	1.5004E+00	1.3746E+00	1.2133E+00	0	0	0	0	0	1	0	1	0
$KHSO_4$(aq)	-8.0584E-01	-1.0836E+00	-1.4815E+00	0	0	0	1	1	1	0	0	0
KOH(aq)	1.4460E+01	1.4460E+01	1.4460E+01	0	0	0	-1	0	1	0	0	0
KSO_4^-	-8.7500E-01	-9.1333E-01	-9.9245E-01	0	0	0	0	1	1	0	0	0
$Mg_4(OH)_4^{4+}$ *	3.9750E+01	3.9750E+01	3.9750E+01	0	4	0	-4	0	0	0	0	0
$MgCO_3$(aq) *	7.3562E+00	7.1557E+00	6.9230E+00	0	1	1	-1	0	0	0	0	0
$MgCl^+$	1.3865E-01	1.2330E-01	5.3627E-02	0	1	0	0	0	0	0	1	0
$MgHCO_3^+$ *	-1.0329E+00	-1.0700E+00	-1.1643E+00	0	1	1	0	0	0	0	0	0
$MgSO_4$(aq) *	-2.4125E+00	-2.5907E+00	-2.8356E+00	0	1	0	0	1	0	0	0	0
NaBr(aq)	1.3623E+00	1.2840E+00	1.1706E+00	0	0	0	0	0	0	1	0	1
$NaCO_3^-$	9.8156E+00	9.8967E+00	1.0079E+01	0	0	1	-1	0	0	0	0	1
NaCl(aq)	7.8213E-01	7.3035E-01	6.4856E-01	0	0	0	0	0	0	0	1	1
$NaHCO_3$(aq)	-1.5573E-01	-3.7720E-02	1.1267E-01	0	0	1	0	0	0	0	0	1
NaOH(aq)	1.4799E+01	1.4345E+01	1.3799E+01	0	0	0	-1	0	0	0	0	1
$NaSO_4^-$	-8.2000E-01	-8.2000E-01	-8.2000E-01	0	0	0	0	1	0	0	0	1
OH^- *	1.3991E+01	1.3537E+01	1.3029E+01	0	0	0	-1	0	0	0	0	0

Table A.4 *Equilibrium constants (log K) and stoichiometric coefficients for mineral reactions (column experiments). Reactions are written as the dissolution of 1 mol of mineral.*

Species	log K 25°C	log K 40°C	log K 60°C	Stoichiometric coefficient								
				Ca^{2+}	Mg^{2+}	HCO_3^-	H^+	SO_4^{2-}	K^+	Br^-	Cl^-	Na^+
Calcite	1.8542	1.6272	1.3304	1	0	1	-1	0	0	0	0	0
Dolomite-disordered	4.0684	3.4414	2.6455	1	1	2	-2	0	0	0	0	0
Gypsum-25/-40/-60	-4.5978	-4.6368	-4.7383	1	0	0	0	1	0	0	0	0

Table A.5 *Parameters for the mineral reaction rate laws (column experiments). All parameters are from Palandri and Kharaka (2004), except for the coefficients m_1 and m_2 for calcite, which are based on the data reported by Xu et al. (2012).*

Mineral	log k_r (25 °C) ($mol/m^2/s$)	E_{app} (kcal/mol)	$a_{H^+}^{n_{H^+}}$	m_1	m_2
Calcite	-0.30	3.44	1.0	3.0	1.0
	-5.81	5.62	-	3.0	1.0
Dolomite	-3.19	8.63	0.5	1.0	1.0
	-7.53	12.48	-	1.0	1.0
Gypsum	-2.79	15.00	-	1.0	1.0

A.1.2 PhreeqC simulation

The input PhreeqC file is attached below.

```
------------------------------------------------------------------------
TITLE L60-34-gp-e
PHASES
Gypsum
      CaSO4:2H2O = Ca+2 + SO4-2 + 2 H2O
      -log_k      -4.7383
      -delta_h -0.0 kcal
      #-analytic  68.2401     0.0   -3221.51    -25.0627
      -Vm 73.9 # 172.18 / 2.33  (Vm H2O = 13.9 cm3/mol)
SOLUTION 0
temp    60
units mol/kgw
pressure 150
pH 3.5 charge
S(6) 2.610e-2
Ca 4.757e-2
Mg 3.273e-2
K  1.125e-2
Na 3.906e-1
Br 1.138e-2
Cl 4.984e-1
C(4) 3.850e-1
END
```

```
SOLUTION 1-17
temp    60
units mol/kgw
pressure 150
pH 3.5 charge
S(6) 2.610e-2
Ca 4.757e-2
Mg 3.273e-2
K  1.125e-2
Na 3.906e-1
Br 1.138e-2
Cl 4.984e-1
C(4) 3.850e-1
END
RATES
Calcite
  -start
   10 sat_cc = SR("Calcite")
   20 rem if (m <= 0  and si_cc < 0) then goto 200
   30  k1 = 10^(-0.30)
   40  k2 = 10^(-5.81)
   50  k1=log(k1)-14400/8.31/2.303*(1/TK-1/298.15) #log k1
   60  k2=log(k2)-23500/8.31/2.303*(1/TK-1/298.15) #log k2
   70  sup=0.22
   80  rem moles=sup*(k1+k2)*(1-10^si_cc)*TIME #mol/l/s
   90  moles=sup*(10^(k1)*act("H+")+10^(k2))*((1-sat_cc)^3.0)*TIME #mol/l/s
   200 save moles
  -end

EQUILIBRIUM_PHASES 1-17
        gypsum 0.0 0.0
KINETICS 1-17
      Calcite
            -tol    1e-8
            -m0    30125
            -m    30125
            -parms      50      0.6
SELECTED_OUTPUT
        -file            montPmathexp.xls
        -totals          Ca S
        -saturation_indices calcite gypsum
        -kinetics calcite gypsum
TRANSPORT
        -cells           17
        -length          0.001
        -shifts          560
        -time_step       128  # en seg.
        -flow_direction  forward
        -boundary_cond   flux  flux
        -diffc           1.0e-9
        -dispersivity    0.001
        -correct_disp    true
        -punch_cells     17  #celda para extraer datos
        -punch_frequency  50 #datos cada 50 steps
END
------------------------------------------------------------------------
```

A.2 (2D) model parameters

Table A.6 *Experimental and input boundary conditions, fracture dimensions, numerical discretization, transport parameters and rock and fracture composition used in simulations of fractured core experiments.*

Experiment label		*L0.2-gp-e*						*L1-gp-e*			*S60-no-s*			
Dissolution pattern		face dissolution						wormhole			uniform			
Experimental Conditions														
T	°C	60												
P	bar	150												
pCO_2	bar	62												
Flow rate Q	mL/h	0.2						1			60			
Fracture Dimensions														
Diameter d	mm	9						9			9			
Aperture a	µm	9						6.7			7.22			
Length L	mm	20						20			20			
Discretization														
Coordinate (duration in h)		rectangular						rectangular (0-15h) + cylindrical (15-72h)			rectangular			
Total number of elements in X		27						133			28			
number of elements		5	5	5	6	3	3	50	33	50	1	10	10	7
element dimension	µm	4.5	9	45	90	180	720	6.7	67	34	3.6	15	75	380
Total number of elements in Y		36						36			20			
number of elements		20		10		6		20	10	6	20			
element dimension	µm	250		500		1667		250	500	1667	900			
Total number of elements in Z		1						-			1			
element dimension	mm	9						-			9			
Zones														
		X-range		Y-range				X-range		Y-range	X-range		Y-range	
Fracture		1-1		1-36				1-1		1-36	1-1		1-20	
Rock		2-27		1-36				2-133		1-36	2-28		1-20	
Transport parameters														
Darcy velocity (N) q	$m^3/m^2/s$	6.86E-04						4.61E-3 (1) + 5.47E-4 (52)			2.56E-01			
Diffusion coeff. D_0	m^2/s	1.1E-10						5.4E-09			1.1E-08			
Cementation exponent n		2.5						2.5			2.5			
Eff. Diffusion coeff. D_e	m^2/s	6.0E-14						3.0E-12			9.5E-12			
Long. Dispersivity α_L	m	0.001						0.001			0.001			
Trans. Dispersivity α_T	m	-						-			-			
Rock matrix														
Rock		oolitic limestone						oolitic limestone			sandstone			
Initial permeability k_0	m^2	1.00E-20						1.00E-20			1.00E-20			
Initial porosity ϕ_0	%	5						5			6			
		Vol. F.		A_m				Vol. F.		A_m	Vol. F.		A_m	
Cal		0.95		2000				0.95		9500	0.612		300000	
Qz		-		-				-		-	0.264		3605	
Mc		-		-				-		-	0.060		2180	
Gp-60		0.00		100				0.00		6	-		-	
Fracture zone														
Initial permeability k_0	m^2	6.75E-12						-			4.32E-12			
Initial porosity ϕ_0	%	100						100			100			
		Vol. F.		A_m				Vol. F.		A_m	Vol. F.		A_m	
Gp-60		0.00		100				0.00		6	-		-	
Input boundary conditions														
Input label		*gp-e*						*gp-e*			*no-s*			

A_m = Reactive surface area in m^2_m/m^3_{bulk}. Vol. F. = Volume fraction.
N = number of nodes along the x direction with fixed flow.
Chemical composition, calculated pH, SI and I of the input solutions are shown in Table 2.2.

Table A.7 *Equilibrium constants (log K) and stoichiometric coefficients for equilibria in solution in fractured core experiment S60-no-s. Reactions are written as the destruction of 1 mol of the species in the first column*

Species	log K	Stoichiometric coefficient									
	60°C	Ca^{2+}	Mg^{2+}	HCO_3^-	H^+	K^+	Br^-	Cl^-	Na^+	Al^{3+}	$SiO_2(aq)$
$Al(OH)_2^+$	8.7460E+00	0	0	0	-2	0	0	0	0	1	0
$Al_{13}O_4(OH)_{24}$	9.8730E+01	0	0	0	-32	0	0	0	0	13	0
$Al_2(OH)_2^{4+}$	7.6902E+00	0	0	0	-2	0	0	0	0	2	0
$Al_3(OH)_4^{5+}$	1.3880E+01	0	0	0	-4	0	0	0	0	3	0
AlO_2^-	1.9573E+01	0	0	0	-4	0	0	0	0	1	0
$AlOH^{2+}$	4.0039E+00	0	0	0	-1	0	0	0	0	1	0
$CO_2(aq)$	-6.2695E+00	0	0	1	1	0	0	0	0	0	0
CO_3^{2-}	1.0132E+01	0	0	1	-1	0	0	0	0	0	0
$CaCO_3(aq)$	6.4479E+00	1	0	1	-1	0	0	0	0	0	0
$CaCl^+$	5.8650E-01	1	0	0	0	0	0	1	0	0	0
$CaCl_2(aq)$	6.2447E-01	1	0	0	0	0	0	2	0	0	0
$CaHCO_3^+$	-1.1605E+00	1	0	1	0	0	0	0	0	0	0
$CaOH^+$	1.2850E+01	1	0	0	-1	0	0	0	0	0	0
$H_2SiO_4^{2-}$	2.2960E+01	0	0	0	-2	0	0	0	0	0	1
$H_4(H_2SiO_4)_4^-$	3.5940E+01	0	0	0	-4	0	0	0	0	0	4
$H_6(H_2SiO_4)_4^-$	1.3640E+01	0	0	0	-2	0	0	0	0	0	4
$HAlO_2(aq)$	1.3727E+01	0	0	0	-3	0	0	0	0	1	0
HCl(aq)	-6.6883E-01	0	0	0	1	0	0	1	0	0	0
$HSiO_3^-$	9.4758E+00	0	0	0	-1	0	0	0	0	0	1
KBr(aq)	1.4461E+00	0	0	0	0	1	1	0	0	0	0
KCl(aq)	1.2133E+00	0	0	0	0	1	0	1	0	0	0
KOH(aq)	1.4460E+01	0	0	0	-1	1	0	0	0	0	0
$Mg_4(OH)_4^{4+}$	3.9750E+01	0	4	0	-4	0	0	0	0	0	0
$MgCO_3(aq)$	6.9230E+00	0	1	1	-1	0	0	0	0	0	0
$MgCl^+$	5.3627E-02	0	1	0	0	0	0	1	0	0	0
$MgHCO_3^+$	-1.1643E+00	0	1	1	0	0	0	0	0	0	0
$NaAlO_2(aq)$	2.0095E+01	0	0	0	-4	0	0	0	1	1	0
NaBr(aq)	1.1706E+00	0	0	0	0	0	1	0	1	0	0
$NaCO_3^-$	1.0079E+01	0	0	1	-1	0	0	0	1	0	0
NaCl(aq)	6.4856E-01	0	0	0	0	0	0	1	1	0	0
$NaHCO_3(aq)$	1.1267E-01	0	0	1	0	0	0	0	1	0	0
$NaHSiO_3(aq)$	8.0585E+00	0	0	0	-1	0	0	0	1	0	1
NaOH(aq)	1.3799E+01	0	0	0	-1	0	0	0	1	0	0
OH^-	1.3029E+01	0	0	0	-1	0	0	0	0	0	0

Table A.8 *Equilibrium constants (log K) and stoichiometric coefficients for mineral reactions (fractured core experiments). Reactions are written as the dissolution of 1 mol of mineral.*

Species	log K	Stoichiometric coefficient									
	60°C	Ca^{2+}	Mg^{2+}	HCO_3^-	H^+	SO_4^{2-}	K^+	Br^-	Cl^-	Na^+	Al^{3+}	SiO_2(aq)
Calcite	1.3304	1	0	1	-1	0	0	0	0	0	0	0
Microcline	-0.9478	0	0	0	-4	0	1	0	0	0	1	3
Quartz	-3.4676	0	0	0	0	0	0	0	0	0	0	1
Gypsum-60	-4.7383	1	0	0	0	1	0	0	0	0	0	0

Table A.9 *Parameters for the mineral reaction rate laws (fractured core experiments). Parameters for calcite, gypsum and quartz are from Palandri and Kharaka (2004), except for the coefficients m_1 and m_2 for calcite, which are based on the data reported by Xu et al. (2012). Parameters for microcline are from Bandstra et al. (2008).*

Mineral	log k_r (25 °C) ($mol/m^2/s$)	E_{app} (kcal/mol)	$a_{H^+}^{n_{H^+}}$	m_1	m_2
Calcite	-0.30	3.44	1.0	3.0	1.0
	-5.81	5.62	-	3.0	1.0
Microcline	-10.06	12.40	0.5	14.0	0.4
	-12.41	9.08	-	14.0	0.4
Quartz	-13.39	15.00	-	1.0	1.0
Gypsum	-2.79	15.00	-	1.0	1.0

Appendix B

Additional experimental and modeling results from the column experiments

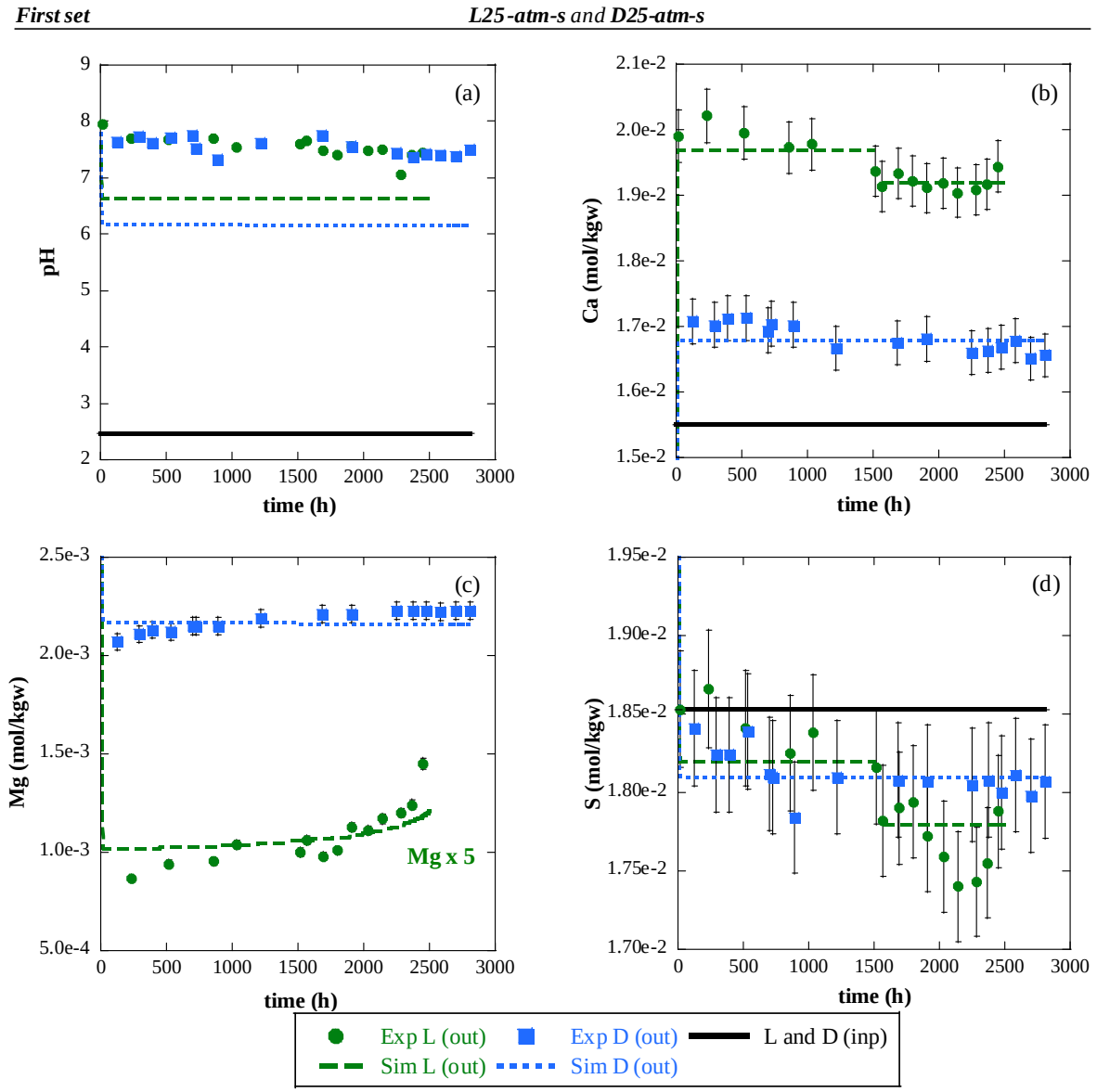

Fig. B.1 *Variation of experimental (Exp) and simulated (Sim) output pH (a) and output concentration of Ca (b), Mg (c) and S (d) with time in limestone (L; in green) and dolostone (D; in blue) column experiments (L25-atm-s and D25-atm-s, respectively). Solid lines indicate input solution except for Mg which is smaller than* 3×10^{-4} *mol/kgw (Table 2.2). Dashed and dotted lines indicate simulated values of limestone and dolostone column experiments, respectively.*

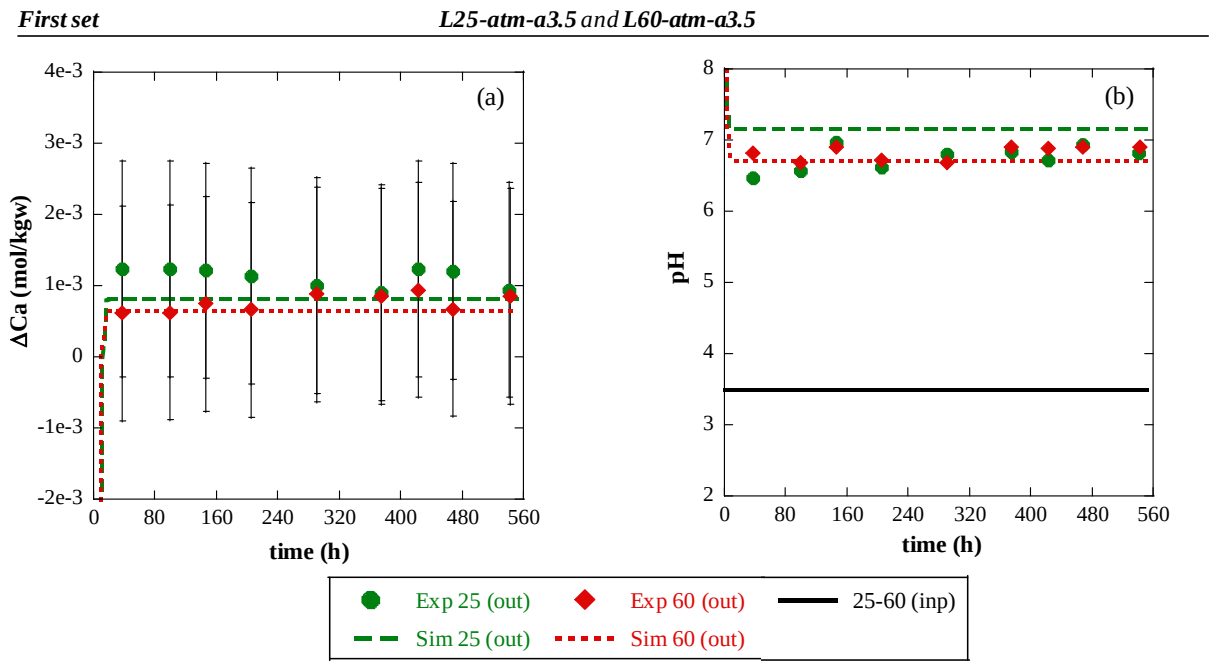

Fig. B.2 *Variation of the experimental (Exp) and simulated (Sim) increase in Ca concentration (a) and output pH (b) with time in limestone column experiments at 25 ºC (in green; L25-atm-a3.5) and 60 ºC (in red; L60-atm-a3.5). Solid line in (b) shows input pH. Dashed and dotted lines show simulated values at 25 and 60 ºC, respectively.*

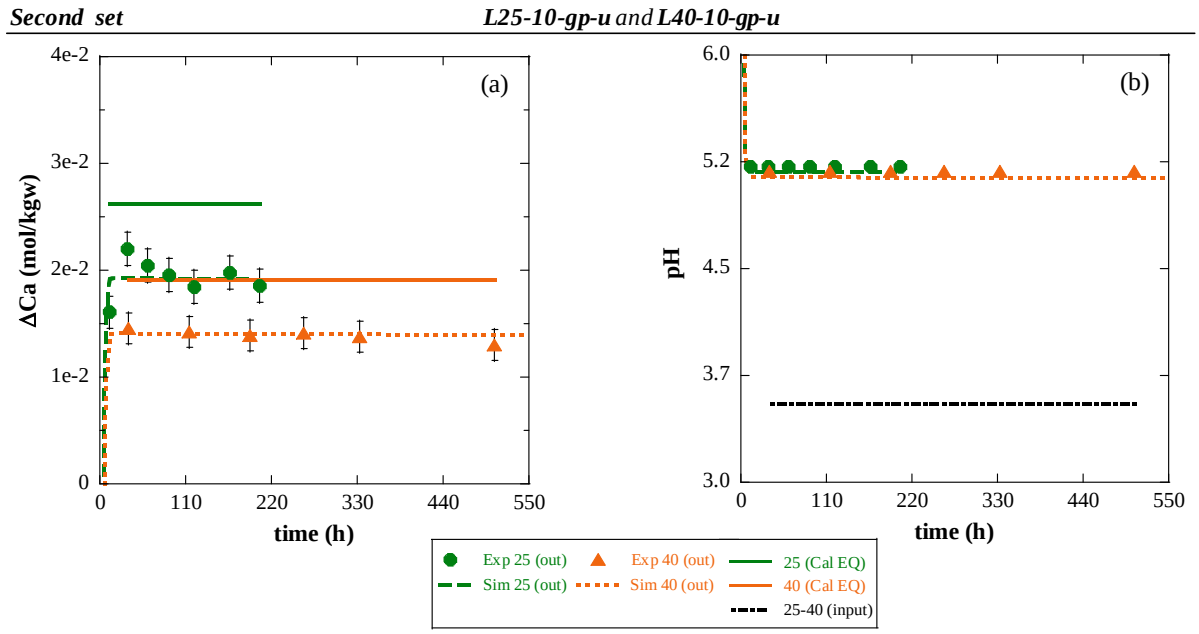

Fig. B.3 *Variation of the experimental (Exp) and simulated (Sim) increase in Ca (a) and output pH (b) with time in limestone column experiments at 25 ºC (in green; L25-10-gp-u) and 40 ºC (in orange; L40-10-gp-u). Colored solid lines in (a) represent the Ca equilibrium with calcite and black-dashed line in (b) indicates input pH. Dashed and dotted lines show simulated values at 25 and 40 ºC, respectively.*

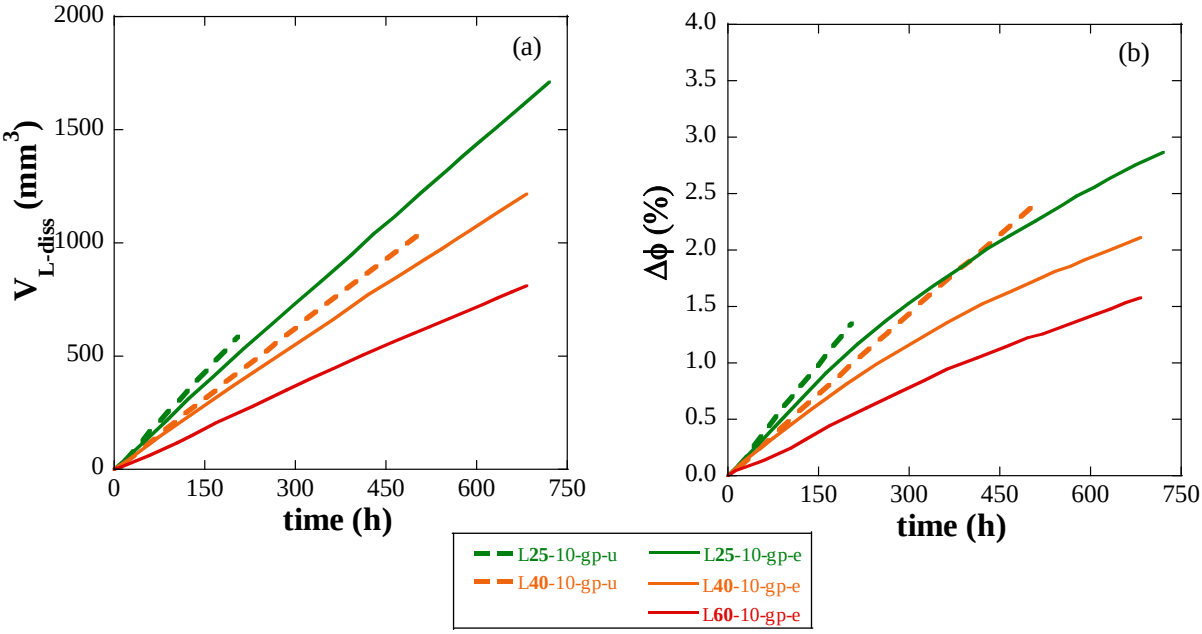

Fig. B.4 *Experimental variation of volume of dissolved limestone $V_{L\text{-}diss}$ (a) and porosity ϕ (b) versus time in experiments performed at 25 ºC (in green; L25-10-gp-u and L25-10-gp-e), 40 ºC (in orange; L40-10-gp-u and L40-10-gp-e) and 60 ºC (in red; L60-10-gp-e). Solid and dashed lines indicate experiments with gypsum-equilibrated and gypsum-undersaturated solutions, respectively.*